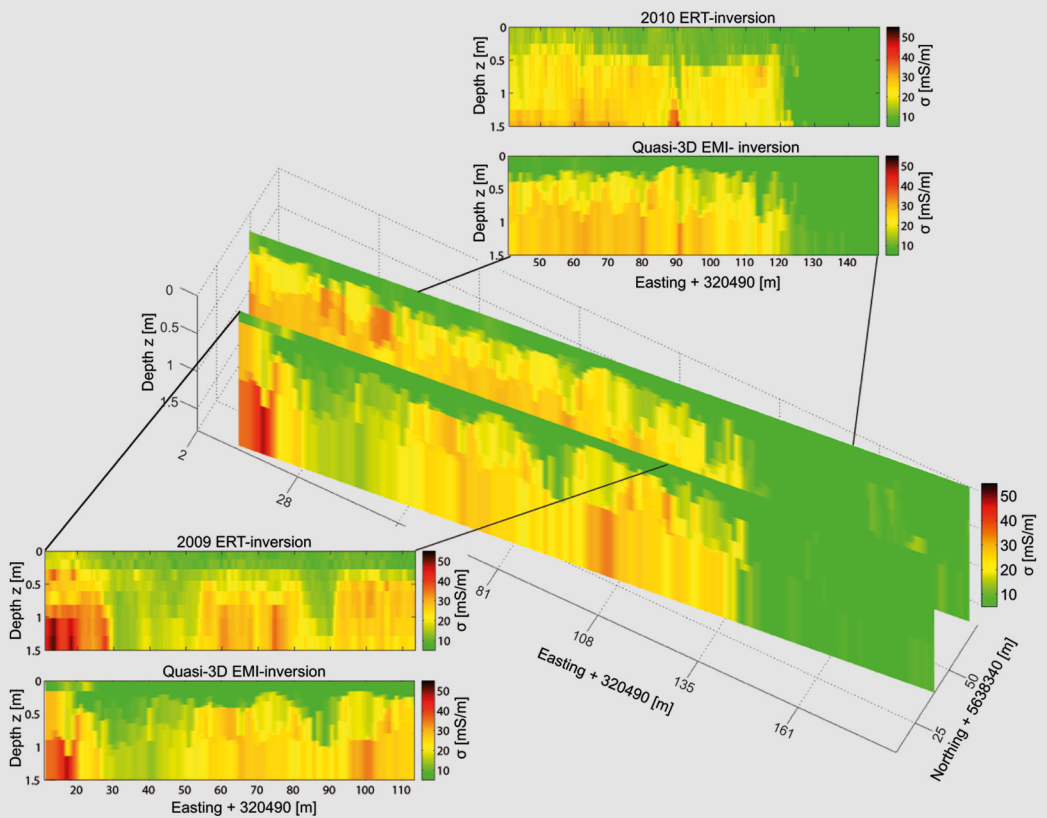


# Calibration and large-scale inversion of multi-configuration electromagnetic induction data for vadose zone characterization

Christian von Hebel







Forschungszentrum Jülich GmbH  
Institute of Bio- and Geosciences  
Agrosphere (IBG-3)

# **Calibration and large-scale inversion of multi-configuration electromagnetic induction data for vadose zone characterization**

Christian von Hebel

Schriften des Forschungszentrums Jülich  
Reihe Energie & Umwelt / Energy & Environment

Band / Volume 36 1

---

ISSN 1866-1793

ISBN 978-3-95806-210-8

Bibliographic information published by the Deutsche Nationalbibliothek.  
The Deutsche Nationalbibliothek lists this publication in the Deutsche  
Nationalbibliografie; detailed bibliographic data are available in the  
Internet at <http://dnb.d-nb.de>.

Publisher and  
Distributor: Forschungszentrum Jülich GmbH  
Zentralbibliothek  
52425 Jülich  
Tel: +49 2461 61-5368  
Fax: +49 2461 61-6103  
Email: [zb-publikation@fz-juelich.de](mailto:zb-publikation@fz-juelich.de)  
[www.fz-juelich.de/zb](http://www.fz-juelich.de/zb)

Cover Design: Grafische Medien, Forschungszentrum Jülich GmbH

Printer: Grafische Medien, Forschungszentrum Jülich GmbH

Copyright: Forschungszentrum Jülich 2017

Schriften des Forschungszentrums Jülich  
Reihe Energie & Umwelt / Energy & Environment, Band / Volume 36 1

D 82 (Diss. RWTH Aachen University, 2016)

ISSN 1866-1793  
ISBN 978-3-95806-210-8

The complete volume is freely available on the Internet on the Jülicher Open Access Server (JuSER)  
at [www.fz-juelich.de/zb/openaccess](http://www.fz-juelich.de/zb/openaccess).



This is an Open Access publication distributed under the terms of the [Creative Commons Attribution License 4.0](https://creativecommons.org/licenses/by/4.0/),  
which permits unrestricted use, distribution, and reproduction in any medium, provided the original work is properly cited.

# Abstract

Frequency-domain electromagnetic induction (EMI) devices measure a secondary magnetic field superimposed by the transmitted primary magnetic field in current conducting media. Commercially available systems convert this magnetic field ratio into an apparent electrical conductivity (ECa), not concretely stated but probably with a linear approximation assuming low induction numbers (LIN). In the LIN-based conversion, errors were observed between the true ground electrical conductivity ( $\sigma(z_i)$ ) and ECa such that the present thesis introduces an improved non-linear exact ECa conversion (EEC) approach that can be used beyond the LIN approximation. Until recently, the EMI method was used for qualitative data interpretations because quantitative ECa values were often not obtained. For example, the operator or the field setup generated additional magnetic fields being measured by the EMI device that shift the recorded ECa. To eliminate the shifts, a post-calibration is required. Here, a cross-correlation between measured and predicted EMI-ECa values resulted in calibration parameters that were applied to the EMI data such that quantitative ECa values were obtained. To predict the EMI device specific ECa values, a Maxwell-based electromagnetic forward model (EM-FM) used  $\sigma(z_i)$  obtained from inverted electrical resistivity tomography (ERT) or inverted vertical electrical sounding (VES) data. Analyzing several post-calibrations based on ERT, coefficients of determination of  $R^2 > 0.75$  were obtained when the data range along a calibration line exceeded 3 mS/m and when the ground electrical conductivity was larger than 5 mS/m. Using derived calibrations of different test sites, universal calibration parameters were obtained that allowed post-calibrations without an ERT reference line. Combining the introduced EEC with the modeling using the EM-FM that assumes horizontal layers in a multi-layer inversion of the post-calibrated EMI data, no errors were introduced anymore such that these methods can be applied also for high electrical conductive, e.g., saline areas, where the LIN approximation is no longer valid.

Large-scale EMI measurements often reflect relevant subsurface patterns, but only few researchers have attempted to resolve the vertical changes in electrical conductivity

that in principle can be obtained using multi-configuration EMI devices that house multiple receiver coils in a single unit. Here, areal quantitative multi-coil ECa values were interpolated onto a regularly spaced grid and the data at each grid node were independently inverted using the EM-FM in a novel parallelized inversion scheme that used the shuffled complex evolution (SCE) algorithm. The obtained inversion results were stitched together and formed a quasi-3D subsurface electrical conductivity model that showed smoothly varying electrical conductivity layers at a 1.1 ha large bare-soil field as well as paleo-river channel structures at a 2.55 ha large test site. At the bare-soil field, the performed three-layer EMI-inversions were validated with low resolution grain size distribution maps and two 120 m long ERT transects, which confirmed the obtained lateral and vertical large-scale electrical conductivity patterns. To fully capture the paleo-river channel dimensions, the field setup was extended from six coil configurations used at the bare-soil field up to 24 coils. A setup optimized for large-scale surveys recorded areal ECa values and all coils measured along transects crossing the channels. Due to the extended coil configurations, the inversion code was generalized from three- to n-layers and the transect data were inverted with up to 5-layers. The inverted electrical conductivities reflected even small changes in soil texture that was determined in the horizons of extracted soil cores and the inverted layer boundaries matched the measured depths.

Consequently, the proposed methods quantitatively characterize the soil layers in the vadose zone, which allows to infer hydrologically active regions, to improve root/crop models and/or to obtain the field capacity and thus the soil water content that is the key for understanding hydrological processes in the unsaturated zone.

# Zusammenfassung

Messgeräte welche die elektromagnetische Induktion nutzen (EMI-Geräte), erzeugen ein primäres magnetisches Feld. Dieses wird von sekundären Feldern, generiert in leitfähigen Bodenschichten, überlagert. Komerzielle EMI-Geräte konvertieren das gemessene Totalfeld in eine scheinbare elektrische Leitfähigkeit (ECa). Die Konvertierung ist nicht genau beschrieben, nutzt aber wahrscheinlich einen linearen Zusammenhang, der auf der Annahme kleiner Induktionszahlen (LIN) basiert. Die LIN-Konvertierung zeigte jedoch Abweichungen zwischen der echten Leitfähigkeit des Untergrundes ( $\sigma(z_i)$ ) und dem ausgegebenen ECa-Wert auf. Daher führt die hier vorliegende Dissertation eine exakte ECa-Konvertierung (EEC) ein, welche nicht-linear zwischen dem magnetischen Feld und ECa konvertiert, wodurch sie eine größere Gültigkeit als die LIN-Annäherung besitzt. Bisherige EMI Studien haben sich oft auf qualitative Datenanalysen beschränkt, da die gemessenen ECa-Werte meistens nicht quantitativ sind, da auch in Medien die das Gerät umgeben, magnetische Felder induziert werden. Diese addieren sich dem Totalfeld hinzu und verfälschen somit den ausgegebenen ECa-Wert, weshalb die gemessenen Werte kalibriert werden müssen. Zur Kalibration wird hier eine lineare Regression zwischen gemessenen und modellierten Daten durchgeführt, um die erhaltenen Parameter auf die EMI-Daten anzuwenden. Um gerätespezifische ECa-Werte zu modellieren, werden Daten der elektrischen Widerstandstomographie (ERT) oder der geoelektrischen Tiefensondierung (VES) invertiert und die erhaltenenen  $\sigma(z_i)$  werden in ein Maxwell-basiertes exaktes elektromagnetisches Vorwärtsmodell (EM-FM) eingestzt. Die Untersuchung vieler der ERT-basierten Kalibrationsmessungen ergaben ein Bestimmtheitsmaß von  $R^2 > 0.75$ , wenn der Bereich der gemessenen oder modellierten Daten  $> 3$  mS/m ist und der Wert der elektrischen Leitfähigkeit des Untergrundes  $> 5$  mS/m ist. Das Zusammenführen vieler solcher Kalibrationen ergab allgemeine Kalibrationsparameter, die es erlauben, EMI-Daten ohne weitere ERT-Messungen zu kalibrieren.

Die kombinierte Anwendung von EEC und des exakten EM-FM, welches horizontale Schichten voraussetzt, führt zu einer nahezu fehlerfreien Viel-Schichten Inversion der kalibrierten EMI-Daten. Daraus folgernd können die vorgestellten Methoden auch in hochleitfähigen, z.B. salinen Böden, in denen die LIN-Annäherung nicht gültig ist, eingesetzt werden.

Großskalige EMI-Karten deuten auf wichtige Untergrundstrukturen hin. Jedoch wurde bisher nur selten versucht unter der Verwendung von Mehrspulengeräten, welche in einer mobilen Konstruktion mehrere Spulenkfigurationen tragen und dadurch verschiedene Tiefen sondieren, die vertikale Leitfähigkeitsverteilung zu ermitteln. Hier wurden die kalibrierten Daten solcher EMI-Geräte in einer parallelisierten Version des Shuffled Complex Evolution (SCE) Algorithmus unter der Verwendung des exakten EM-FM invertiert. Dazu wurden die Daten der Mehrspulen-Geräte auf ein gemeinsames Gitter interpoliert und an den Gitterpunkten unabhängig voneinander invertiert. Die anschließende Zusammenführung der Inversionsergebnisse erzielte ein quasi-3D Untergrundmodell. Diese großskalige Inversion wurde auf ein ca. 1,1 ha großes brachliegendes Feld und auf ein ca. 2,55 ha großes Feld, welches durch Paleo-Flussstrukturen im Untergrund gekennzeichnet ist, angewendet. Die Drei-Schicht Inversionen des brachliegenden Feldes wurden mit Körnungsgrößen und mit zwei unabhängigen 120 m langen ERT-Linien validiert. Um die Dimensionen der Paleo-Flussstrukturen besser zu erfassen, wurden die sechs EMI-Spulenkfigurationen, welche auf dem brachliegendem Feld zum Einsatz kamen, auf bis zu 24 Spulen erweitert. Für die Flächen-daten wurde die Gerätezusammenstellung optimiert, auf senkrecht zu den Strukturen verlaufenden Messlinien wurde mit allen Spulenkfigurationen gemessen. Aufgrund der erweiterten Konfigurationen konnte der Inversionscode von Drei- auf generell n-Schichten erweitert werden, sodass die Transekt-daten mit bis zu 5 Schichten invertiert wurden. Die mit Bohrkernen validierten Inversionsergebnisse reflektierten selbst kleine Texturänderungen in den erbohrten Schichten, wobei gerade die Schichtgrenzen sehr gut rekonstruiert wurden.

Zusammengefasst, die hier vorgestellten Methoden charakterisieren die Schichten der vadosen Zone quantitativ, sodass die Ergebnisse z.B. auf hydrologisch relevante Schichten schließen lassen, oder zur Verbesserung von Wurzelmodellen beitragen können und/oder es kann auf die Feldkapazität und somit auf den Bodenwassergehalt geschlossen werden, welcher eine Schlüsselrolle in den Prozessen der ungesättigten Bodenzone einnimmt.

# Publications

Parts of this doctoral thesis have been published or submitted or will be used for future publications. The following list gives an overview of the written publications during my doctoral studies.

1. **von Hebel, C.**, S. Rudolph, A. Mester, J.A. Huisman, P. Kumbhar, H. Vereecken, and J. van der Kruk. 2014. Three-dimensional imaging of subsurface structural patterns using quantitative large-scale multiconfiguration electromagnetic induction data. *Water Resources Research*, 50, 2732–2748, doi:10.1002/2013WR014864
2. **von Hebel, C.**, J. van der Kruk, A. Mester, D. Altdorff, E. Zimmermann, A. Endres, and H. Vereecken. Conversion and post-calibration for quantitative inversion of electromagnetic induction data beyond the LIN approximation. submitted to *Geophysics*
3. **von Hebel, C.**, J. van der Kruk, H. Vereecken. Imaging of paleo-river channels by joint data inversion of multiple electromagnetic induction devices. in preparation.
4. **Rudolph, S.**, J. van der Kruk, C. von Hebel, M. Ali, M. Herbst, C. Montzka, S. Patzold, D.A. Robinson, H. Vereecken, L. Weihermüller. 2015. Linking satellite derived LAI patterns with subsoil heterogeneity using large-scale ground-based electromagnetic induction measurements. *Geoderma*, 241, 262–271, 10.1016/j.geoderma.2014.11.015
5. **van der Kruk, J.**, N. Gueting, A. Klotzsche, G. He, S. Rudolph, C. von Hebel, X. Yang, L. Weihermüller, A. Mester, H. Vereecken. 2015. Quantitative multi-layer electromagnetic induction inversion and full-waveform inversion of cross-hole ground penetrating radar data. *Journal of Earth Science*, 26 (6), 844–850, 10.1007/s12583-015-0610-3

6. **Borchard, N.**, M. Schirrmann, C. von Hebel, M. Schmidt, R. Baatz, L. Firbank, H. Vereecken, M. Herbst. 2015. Spatio-temporal drivers of soil and ecosystem carbon fluxes at field scale in an upland grassland in Germany. *Agriculture, Ecosystems and Environment*, 211, 84–93, 10.1016/j.agee.2015.05.008
7. **Altdorff, D.**, C. von Hebel, N. Borchard, J. van der Kruk, H. Boga, H. Vereecken, J.A. Huisman. Potential of catchment-wide soil water content mapping using electromagnetic induction in a forest ecosystem. accepted in *Environmental Earth Science*
8. **Mester, A.**, E. Zimmermann, C. von Hebel, J. van der Kruk, H. Vereecken and S. van Waasen, Field-optimization and validation of a novel multi channel electromagnetic induction system. in preparation

# Contents

<b>1</b>	<b>Introduction</b>	<b>1</b>
<b>2</b>	<b>Electromagnetic Induction Forward and Inverse Modeling</b>	<b>7</b>
2.1	Electromagnetic Induction Forward Models . . . . .	7
2.1.1	Exact electromagnetic forward model (EM-FM) . . . . .	8
2.1.2	Multi-coil EMI data above layered earth models . . . . .	9
2.2	n-Layer Inversion Algorithms . . . . .	10
2.2.1	Shuffled complex evolution (SCE) . . . . .	11
2.2.2	Differential evolution adaptive metropolis (DREAM <sub>ZS</sub> ) . . . . .	13
<b>3</b>	<b>Conversion and Post-Calibration for Quantitative Inversion of Elec- tromagnetic Induction Data beyond the LIN Approximation</b>	<b>15</b>
3.1	Magnetic Field and Apparent Electrical Conductivity Conversion . . . . .	16
3.1.1	Low induction number (LIN) -based conversion . . . . .	17
3.1.2	Comparison of exact EM-FM and LIN model . . . . .	17
3.1.3	Exact non-linear ECa conversion (EEC) . . . . .	19
3.2	Synthetic EMI Data Inversion using LIN-based Conversion and EEC . . . . .	21
3.3	Post-Calibration of Multi-Coil EMI Data . . . . .	23
3.3.1	ECa shifts in EMI measurements . . . . .	23
3.3.2	Site specific ECa post-calibration using electrical resistivity to- mography (ERT) . . . . .	25
3.3.3	Deducing universal calibration parameters . . . . .	27
3.4	Quantitative Inversions of Experimental Multi-Coil EMI Data . . . . .	30
3.4.1	Inversion using LIN-based conversion and EEC . . . . .	30

3.4.2	Inversion of universal calibrated EMI data . . . . .	32
3.5	Conclusions . . . . .	33
<b>4</b>	<b>Quasi-3D Test Site Characterization Using Inverted Quantitative Multi-Coil Electromagnetic Induction Data</b>	<b>35</b>
4.1	Selhausen Bare-Soil Field . . . . .	36
4.2	EMI and ERT Data Acquisition . . . . .	37
4.3	Data Processing and Filtering . . . . .	39
4.4	Results and Discussion . . . . .	40
4.4.1	Calibration and three-layer inversions of transect data . . . . .	40
4.4.2	Quasi-3D inversions of quantitative large-scale EMI data . . . . .	45
4.5	Conclusions . . . . .	49
<b>5</b>	<b>Imaging of Buried Paleo-River Channels by Joint Data Inversion of Multiple Electromagnetic Induction Devices</b>	<b>51</b>
5.1	Selhausen Paleo-River Channel Field . . . . .	52
5.2	EMI Field Setup . . . . .	53
5.3	EMI Surveys . . . . .	54
5.3.1	Large-scale data acquisition . . . . .	54
5.3.2	Transect measurements . . . . .	55
5.3.3	Post-calibration and validation data . . . . .	56
5.4	Large-Scale Data Inversion Results . . . . .	58
5.5	Detailed transect inversions . . . . .	63
5.6	Conclusions . . . . .	69
<b>6</b>	<b>Final Conclusions and Outlook</b>	<b>71</b>
6.1	Conclusions and Discussions . . . . .	71
6.2	Outlook . . . . .	76
<b>A</b>	<b>EMI post-calibration based on vertical electrical soundings</b>	<b>77</b>
A.1	Vertical electrical sounding (VES) data acquisition . . . . .	78
A.2	VES forward and inverse modeling . . . . .	79
A.3	VES based post-calibration of multi-coil EMI data . . . . .	80

<b>B</b>	<b>Supplementary data for test site characterizations</b>	<b>85</b>
B.1	Bare-soil field topography and aerial image . . . . .	86
B.2	Weather conditions before and during the large-scale surveys . . . . .	86
B.3	Synthetic study to compromise EMI setup and earth reconstructions . .	87
B.4	Pedo-transfer functions and field capacity . . . . .	89
B.4.1	Pedo-transfer model . . . . .	89
B.4.2	Toward 3D field capacity . . . . .	89
B.5	Large-scale ECa maps of campaign II . . . . .	91
B.6	Additional transect analysis results . . . . .	93
<b>C</b>	<b>DREAM on synthetic and experimental data</b>	<b>97</b>
C.1	Synthetic data inversion . . . . .	97
C.2	Experimental data inversion . . . . .	100



# Chapter 1

## Introduction

The vadose zone is part of the earth's critical zone, which includes the subsurface hydrosphere, pedosphere, and biosphere where the physical, chemical, and biological mass and energy exchange processes are driven. This highly important part of the earth provides vital resources, for example food production, such that scientists improve vadose zone characterizations to enable better management and protection strategies.

Many subsurface processes depend on soil water content which plays a major role in ecosystem developments such as plant performance and growth [Vereecken et al., 2008]. To determine and study the subsurface hydrology minimally invasive, hydrologists and geophysicists developed the interdisciplinary research field hydrogeophysics to gain a hydrological understanding through geophysical observations [Binley et al., 2015]. Hydrogeophysical investigations in the unsaturated zone often use methods that respond to the soil electrical properties. Techniques such as ground penetrating radar (GPR), electromagnetic (EM) methods and/or electrical resistivity tomography (ERT) are often used to estimate the soil water content and further characteristics such as soil texture, mineralization, porosity, or residual pore water content [Rubin, 2005].

Hydrological studies often require soil water content estimations with a high lateral and vertical resolution at the catchment-scale [Robinson et al., 2008]. To characterize areas up to the km<sup>2</sup>-scale, contactless and mobile EM measurements show a particular large potential, where for example helicopter-based time-domain EM (TEM) methods have been successfully used to map aquifers up to several hundred meters depths

[Sørense and Auken, 2004]. For investigations of the upper meters, TEM techniques are more difficult to apply due to the dead-time of the method. In this case, frequency domain electromagnetic induction (EMI) devices are more appropriate because the entire system of transmitter and receiver units can be carried in one mobile construction with fixed coil separations of up to 4.0 m such that up to 6 m depth can be explored.

The fixed-boom EMI method was successfully used to obtain and analyze the soil water content [Sheets and Hendrickx, 1995; Hardie and Doyle, 2012] and to infer the water holding capacity within a catchment [Abdu et al., 2008]. The soil water dynamics were obtained by repeating EMI measurements over several months to distinguish between the influence of time-invariant soil properties (e.g., clay content) and the dynamic soil water content changes, which identified hydrological patterns and pathways [Robinson et al., 2009]. In a consequent EMI time-lapse study, Robinson et al. [2012] estimated the relative catchment-scale changes in soil water content by subtracting the areal EMI data of the driest season from data collected during wet phases. Therefore, EMI surveys can be used to provide catchment characterizations and are preferable to classical methods, e.g., gravimetric soil sampling and time domain reflectometry [Robinson et al., 2003], because these methods are laborious when covering large areas and deliver limited depth and sparse point-scale information.

These limitations were addressed by introducing wireless sensor networks [Bogena et al., 2010; Rosenbaum et al., 2012], however the large amount of soil water content sensors required for such a network may be prohibitive from a cost perspective. Large-scale low-resolution soil water content of the upper few centimeters can be derived from air- or space-borne remote sensing techniques [Kerr et al., 2001; Montzka et al., 2011], which scan the ground surface in swathes measured with hundred of meters up to orbital distances. The gap between point-scale and remote sensing resolution may be filled by contactless EMI measurements.

Recently, Rudolph et al. [2015] investigated EMI data together with satellite based remote sensing images received after a two month drought period at a 20 ha large test site. They transferred the satellite based data into leaf area index (LAI), a proxy for plant performance, and found good correlations between EMI and LAI data. Patterns of increased EMI and LAI values were present due to the presence of buried paleo-river

channels. These channels were filled with finer textured soils in a mainly gravelly area such that they inherently have a higher water holding capacity and provide thus more plant available water especially under drought conditions.

The EMI method measures the bulk soil that composes, beside the water content, e.g., mineral grains and salt such that relatively high correlations were found between EMI data and clay pans [Doolittle et al., 1994; Sudduth et al., 2005] and soil texture in general [Saey et al., 2013; Piikki et al., 2015]. Furthermore, EMI helped in agricultural studies to reduce fertilizer supply and irrigation [Corwin and Lesch, 2003; Adamchuk et al., 2004; Corwin and Plant, 2005] and to investigate the plant and (saline) soil interactions [Dejong et al., 1979; Lesch et al., 1992; Stadler et al., 2015].

### Sensitivity curves

The electromagnetic induction devices pass an alternating current at a fixed frequency ( $f < 10^5$  Hz) through a transmitter coil while generating a primary magnetic field ( $H_P$ ) according to Ampère's law. Due to induction phenomena, Faraday's law,  $H_P$  induces an electromotive force (emf) that forces eddy currents to flow in an electrical conductive subsurface, which in turn generate a secondary magnetic field ( $H_S$ ). The interference of  $H_S$  and  $H_P$  is measured at a receiver coil [Telford et al., 1990], where a changing coil configuration, i.e., combination of orientation and separation  $s$ , changes the depth of investigation (DOI).

Recently developed and commercially available EMI devices house multiple receiver coils with certain separations in a single unit to simultaneously sense different but overlapping subsurface volumes. Increasing the coil separation increases the sensing depth and changing the orientation changes the sensitivity. Whereas perpendicular (PRP) and vertical coplanar (VCP) oriented coils show the maximum sensitivity at the near surface and decrease monotonically with depth, the sensitivity of horizontal coplanar (HCP) coils peak at a certain depth, see Figure 1.1a. Integrating the local sensitivities obtains the cumulative response as shown in Figure 1.1b. By definition, the DOI is the depth to which a coil configuration accumulates approximately 70% of its total sensitivity [McNeill, 1980] such that the DOI of PRP, VCP, and HCP coils is approximately 0.5-s, 0.75-s, and 1.5-s, respectively.

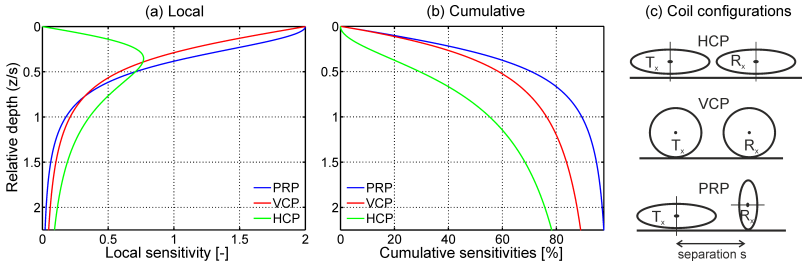


Figure 1.1: (a) local and (b) cumulative sensitivities of PRP, VCP and HCP coil configurations vs. relative depth, i.e.,  $z/s$ . (c) Shows the respective coil arrangements.

The induced secondary magnetic fields lag  $H_P$  by  $90^\circ$  due to the emf and up to  $180^\circ$  due to additional subsurface electrical properties [Keller and Frischknecht, 1966] such that  $H_S$  contains an in-phase (real) and a quadrature (imaginary) part. The quadrature component is non-linearly related to the apparent electrical conductivity (ECa) of the subsurface [Ward and Hohmann, 1988] that reflects a weighted average value over the coil configuration specific sensing depth [Kaufman and Keller, 1983].

### EMI calibration

External influences such as the presence of the operator, on-field zero leveling procedures [Gebbers et al., 2009; Nüsch et al., 2010] or the field setup produce additional magnetic fields that interfere with the secondary magnetic fields generated in the subsurface such that the recorded ECa can be shifted. Moreover, temperature changes and/or inner instrumental changes due to aging electronics can additionally shift the recorded ECa [Sudduth et al., 2001; dos Santos and Porsani, 2011]. Mainly due to these drifts and shifts, the usage of EMI data has been limited to plotting of ECa maps and qualitative interpretations.

To obtain quantitative ECa, the EMI data need calibration. One post-calibration approach performs colocated EMI and ERT measurements along a calibration line and is based on linear regressions between measured and predicted ECa [Lavoué et al., 2010; Minsley et al., 2012; Shanahan et al., 2015]. Another post-calibration procedure records EMI-ECa at certain sampling locations and performs a linear regression with ECa predicted by the electrical conductivity distribution of extracted soil cores [Moghadas et al., 2012].

To predict EMI-E<sub>Ca</sub> of an electrical current conducting earth, James R. Wait derived formulas in the 1950's that describe the non-linear relationship between the secondary magnetic field and the ground electrical conductivity. By introducing the low induction number (LIN) approximation [Wait, 1954], a linear relationship was obtained and the response functions were simplified [McNeill, 1980]. Note that this LIN model is only valid when small separated coils of a low frequency EMI device lie at the ground surface of a homogeneous half-space with low electrical conductivity [McNeill and Bosnar, 1999; Callegary et al., 2007; Beamish, 2011], whereas precise EMI data of a layered subsurface can be computed using a Maxwell-based full solution electromagnetic forward model (EM-FM) [Ward and Hohmann, 1988].

### **EMI inversion**

Due the availability of multi-coil EMI devices, many developments were recently initiated to obtain images of a layered subsurface. For example, Santos et al. [2010] developed a multi-coil EMI inversion scheme based on the LIN model that was also used to separate two distinct layers above the bedrock [Saey et al., 2012]. The available and increasing computational power allows to use the Maxwell-based EM-FM to characterize the individual subsurface layers reflected by their electrical properties. Hydrogeological strata were modeled [Triantafyllis et al., 2012] and active layers in permafrost regions were explored [Dafflon et al., 2013]. The exact EM-FM was also used to invert multiple EMI data that were ERT-based calibrated using the Lavoué et al. [2010] approach for a two-layered medium over a 120 m long transect [Mester et al., 2011]. Their calibrated EMI data inversion approach initiated the present doctoral thesis that shows that for reliable inversions the multi-coil E<sub>Ca</sub> values must be accurate, precise and quantitative. Since the LIN model describe a linear relation for a non-linear dependency, non-LIN methods are required to obtain accurate data. To have confidence with the precision of the EMI device, the measurement influences need to be understood and only after post-calibration, quantitative multi-layer EMI inversions are feasible such that the work presented here turns the EMI usage from a simple proxy indicator toward a tool that quantitatively characterizes the subsurface, which enable a wide range of catchment scale vadose zone applications to benefit from the outlined methods.

## Objectives and outline

The goal of quantitative subsurface characterizations reflected by lateral and vertical electrical property changes is achieved by three main objectives as described and analyzed after introducing the main theory needed for EMI forward and inverse modeling in [Chapter 2](#).

[Chapter 3](#) describes how to overcome the LIN limitations and how to obtain accurate ECa values in EMI forward and inverse modeling. The classical approaches are compared with the introduced novel methodologies. Next, the influences on EMI measurements are investigated and post-calibration approaches are described and used to obtain quantitative EMI data that are used in presented transect inversions.

In [Chapter 4](#), the gained knowledge is used to resolve three-dimensional (3D) large-scale multi-layer electrical conductivity structures based on a quasi-3D EMI data inversion. The ECa values of an approximately 1.1 ha large test site were recorded with one multi-coil EMI device and post-calibrated using colocated EMI and ERT measurements over a relatively short calibration line. The quantitative ECa values were interpolated to an equally spaced grid and inverted using a parallelized deterministic inversion code that resolved the subsurface assuming three-layers.

In [Chapter 5](#), the previously used inversion code is extended up to five-layers that are validated with ground truth data. To enable n-layer large-scale and detailed transects inversions, the multi-coil ECa values of up to 24 coil configurations are post-calibrated based on ERT and vertical electrical sounding (VES) data. The detailed transect inversions are performed above buried paleo-river channels that were revealed in the large-scale inversions of the investigated 2.55 ha field. To this end, the obtained inversion results are compared to soil horizons of extracted soil cores.

The last [Chapter 6](#) closes the thesis with final conclusions and an outlook to ongoing and future work.

## Chapter 2

# Electromagnetic Induction Forward and Inverse Modeling

### 2.1 Electromagnetic Induction Forward Models

The exact EM-FM predicts the magnetic field values given the medium properties. The plane wave (PW) propagation/diffusion of the quasi-static electromagnetic field in the  $z$ -direction can be written in a general formulation as  $PW = PW_0 e^{-\gamma z}$ . The propagation constant  $\gamma$  is defined as [Fitterman and Labson, 2005]

$$\gamma = \sqrt{j\omega\mu_0\sigma}, \quad (2.1)$$

where  $j = \sqrt{-1}$  is the imaginary unit,  $\omega = 2\pi f$  is the angular frequency of the EMI signal,  $\mu_0$  is the magnetic permeability of free-space ( $\mu_0 = 4\pi 10^{-7}$ ), and  $\sigma$  is the electrical conductivity of the medium.

The skin depth  $\delta$  is defined where the magnetic field strength falls to  $1/e$  ( $e \approx 2.7183$ ) or 37% of the surface value via

$$\delta = \sqrt{2/\omega\mu_0\sigma}. \quad (2.2)$$

such that  $\delta$  indicates the penetration depth of the electromagnetic field.

### 2.1.1 Exact electromagnetic forward model (EM-FM)

The magnetic field ratio measured at a receiver coil can be modeled for a homogeneous half-space according to Wait [1955, 1962]

$$\left(\frac{H_P+H_S}{H_P}\right)^{PRP} = \gamma^2 s^2 (I_1 K_1 - I_0 K_0) + 4\gamma s (I_1 K_0 - I_0 K_1) + 16I_1 K_1, \quad (2.3)$$

$$\left(\frac{H_P+H_S}{H_P}\right)^{VCP} = -\frac{2}{\gamma^2 s^2} [3 - \gamma^2 s^2 - (3 + \gamma s + \gamma^2 s^2)e^{-\gamma s}], \quad (2.4)$$

$$\left(\frac{H_P+H_S}{H_P}\right)^{HCP} = \frac{2}{\gamma^2 s^2} [9 - (9 + 9\gamma s + 4\gamma^2 s^2 + \gamma^3 s^3)e^{-\gamma s}], \quad (2.5)$$

where  $I_0, I_1, K_0, K_1$  are the modified Bessel functions with the argument  $\gamma s/2$ . The complex function  $\gamma s$  is expressed by the coil separation  $s$  and skin depth  $\delta$  as

$$\begin{aligned} \gamma s &= \frac{s}{\delta}(1+j) \quad \text{or as function of the induction number } (N_b) \\ \gamma s &= N_b(1+j) \quad \text{where } N_b = \frac{s}{\delta}. \end{aligned} \quad (2.6)$$

For a horizontally n-layered earth the expressions are discussed by Ward and Hohmann [1988] and are given by Wait [1982] as

$$\left(\frac{H_P+H_S}{H_P}\right)^{PRP} = 1 - s^3 \left[ \int_0^\infty R_0 J_1(s\lambda) \lambda^2 d\lambda \right], \quad (2.7)$$

$$\left(\frac{H_P+H_S}{H_P}\right)^{VCP} = 1 - s^2 \left[ \int_0^\infty R_0 J_1(s\lambda) \lambda d\lambda \right], \quad (2.8)$$

$$\left(\frac{H_P+H_S}{H_P}\right)^{HCP} = 1 - s^3 \left[ \int_0^\infty R_0 J_0(s\lambda) \lambda^2 d\lambda \right]. \quad (2.9)$$

Here,  $J_0, J_1$  are the zeroth and first order Bessel functions, respectively,  $\lambda$  is the radial wave number and  $R_0$  is the reflection coefficient [Ward and Hohmann, 1988] that can recursively be obtained using

$$R_n(h_n, \sigma_n) = \frac{\frac{\Gamma_n - \Gamma_{n+1}}{\Gamma_n + \Gamma_{n+1}} + R_{n+1} e^{-2\Gamma_{n+1} h_{n+1}}}{1 + \frac{\Gamma_n - \Gamma_{n+1}}{\Gamma_n + \Gamma_{n+1}} R_{n+1} e^{-2\Gamma_{n+1} h_{n+1}}}, \quad (2.10)$$

with  $R_{n+1} = 0$  [Slob and Fokkema, 2002] and  $\Gamma_n = \sqrt{\lambda^2 + \gamma_n^2}$ , where  $\gamma_n^2$  is the n-th layer propagation constant. The quasi-static exact EM-FM neglects displacement currents and assumes only a horizontally layered earth and no other assumption.

### 2.1.2 Multi-coil EMI data above layered earth models

The exact EM-FM for a layered subsurface were used to compute the earth response for multiple EMI devices namely the CMD-MiniExplorer (ME) and a custom-made CMD-SpecialEdition (SE) that GF-Instruments, Brno, Czech Republic manufactured according to our provided specifications as well as the DualEM-421 (DUEM) of DualEM, Milton, Canada. The ME and the SE house three and six coplanar receiver coils, respectively, that can be oriented either in VCP or in HCP mode. The DUEM carries three PRP plus three HCP coils in one single unit, see also Table 2.1.

Table 2.1: Multi-coil EMI device configurations used to generate the synthetic measurements in the present section and used later to characterize the test sites.

EMI device	Receiver	Orientation	Separation [cm]	Frequency [kHz]	Manufacturer
ME	3	VCP , HCP	32, 71, 118	30	GF-Instruments
SE	6	VCP , HCP	35, 49, 71, 97, 135, 180	25.17	GF-Instruments
DUEM	3 + 3	PRP + HCP	110, 210, 410 + 100, 200, 400	9	DualEM

Figure 2.1a shows ECa values of the 24 coil configurations displayed with crosses above layered earth models with the electrical properties presented in Figure 2.1b. Six coil configurations of shallow, intermediate, and deep sensing were highlighted by dashed lines. In the case of a homogeneous earth, model 1, all devices measured of course the same ECa value due to no electrical depth variation. In the case of increasing electrical conductivities with depth (models 2 to 4), the deepest sensing DUEM-HCPs400 coil configuration measured the largest while the shallowest sensing ME-VCPs32 measured the lowest ECa values and the intermediate deep sensing coil configurations measured values in-between. In the case of decreasing electrical conductivity with depth, see results above models 5 to 7, the opposite trend was visible. Consequently, the exact EM-FM generate data that can be used to determine the vertical electrical conductivity changes.

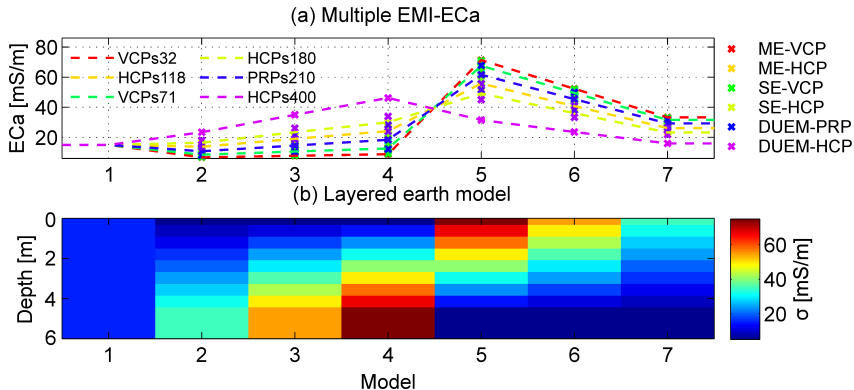


Figure 2.1: (a) Multiple EMI device data computed for the layered earth models shown in (b). The coil configurations of the three commercial EMI devices, see Table 2.1, i.e., CMD-MiniExplorer (ME), a custom-made CMD-SpecialEdition (SE), and DualEM-421 (DUEM) were inserted together with the layered electrical conductivities into the exact EM-FM of Equations 2.7 to 2.9. The obtained magnetic field ratios were converted into ECa using the exact ECa conversion presented in Section 3.1

## 2.2 n-Layer Inversion Algorithms

Using the data of multiple EMI devices enable the reconstruction of an n-layer electrical conductivity model by jointly inverting all device and coil specific magnetic field ratios. The inverse modeling scheme here optimizes the normalized  $L_1$ -norm using the following objective function [Mester et al., 2011]

$$\Delta H(\mathbf{mp}) = \frac{1}{D} \sum_{d=1}^D \left[ \frac{|H_d^{meas} - H_d^{mod}(\mathbf{mp})|}{H_d^{meas}} \right], \quad (2.11)$$

where  $\Delta H(\mathbf{mp})$  describes the misfit between the measured magnetic field,  $H_d^{meas}$ , and the modeled magnetic field  $H_d^{mod}(\mathbf{mp})$  that depends on the medium parameters, where  $\mathbf{mp} = [\sigma_i, h_j]$ ,  $i = 1 \dots n$ ,  $j = 1 \dots n-1$ , and  $D$  is the total number of the coil configurations (separations and orientations) of the EMI devices. The absolute difference  $L_1$ -norm is used because it is less influenced by outliers compared to the more traditional squared difference  $L_2$ -norm. Moreover, no smoothing or damping parameters were considered to assure sharp layer boundaries between adjacent structures.

This objective function was successfully used by Mester et al. [2011], who combined a global and subsequent local search using the LIN model and the exact EM-FM, respectively, to invert for two-layers described by  $\sigma_{1,2}$  and  $h_1$ . Trying to extend this approach

to three layers hence a five dimensional parameter space resulted in the inversions being trapped in local minima possibly due to the use of the LIN approximation in the global search. Consideration of lateral constraints for neighboring inversions similar to Auken et al. [2005] resulted in a directional dependency, which also indicated that the inversions ended in local minima.

### 2.2.1 Shuffled complex evolution (SCE)

To explore the user-defined parameter space for n-layer electrical conductivity models, the shuffled complex evolution (SCE) algorithm was used and parallelized. The SCE is a global optimization that combines deterministic strategies to guide the search with the inclusion of random elements that make the algorithm flexible and robust [Duan et al., 1992]. Here, a population spread out over the feasible parameter space is divided into sub-populations, called complexes. Each complex carries information on number, location and size of the major regions of attraction [Vrugt et al., 2003; Mboh et al., 2011] and an implicit clustering strategy concentrates the search in the most promising regions [Duan et al., 1992].

The parameter search space explored by the SCE algorithm was spanned by the EMI data. For the n-layer electrical conductivities, the maximum and minimum ECa values were doubled and halved, respectively, to ensure a wide range of possible candidates. For the maximum layer thicknesses different values were tested and/or prior information were included because the layer thickness is the least sensitive parameter during the optimization [Mester et al., 2011]. For example, agricultural fields often show a ploughing depth of around 30 cm such that the maximum first layer thickness could be set to 0.35 m. If the contrast to the lower soil is not significant, the maximum thickness can be increased. A more general approach uses the DOI of the EMI coil configurations as follows. The layer depths can be set at the intersections of the coil specific DOI's, where the deepest boundary was set between the two deepest sensing coil configurations because one coil delivers too few information of deeper material changes (compare Figure 1.1a). The minimum layer thickness was  $\geq 0.10$  m to ensure stable numerical integration [Mester et al., 2011].

Figure 2.2 shows the SCE flow. The algorithm starts by random sampling from the parameter space  $\Omega$  from which  $S = c \times p$  points are sampled, where  $c$  is the number of complexes and  $p$  the number of parameter sets per complex. Tests showed a well agreement between inversion time and convergence to the global minimum when  $c$  equals the dimensionality of the problem, i.e., for  $n$ -layers  $c = 2 \cdot n - 1$ , with  $p = 2 \cdot c + 1$  parameter sets per complex.

The code evaluates the objective function for each parameter combination and sorts the parameter sets with increasing misfit into matrix  $M$  that is partitioned into  $A^k, k = 1 \dots c$  complexes. A systematic strategy evolves each complex independently, according to the competitive complex evolution (CCE) algorithm. In the CCE, the space is searched in different directions while a triangular probability distribution ensures competitiveness [Duan et al., 1993]. This basically means that CCE uses different parameter combinations and evolves the population by newly sampled parameters.

Next, the evaluated parameter sets of the individual complexes are shuffled and replaced into matrix  $M$  that is once again sorted with increasing misfit and again partitioned into complexes. The evolution and shuffling processes are continued until one of the two following convergence criteria has been reached: 1) maximum of  $1000 \cdot n^2$  function evaluations or 2) improvement smaller than 0.01% within 10 CCE loops. The competitive complex evolution and shuffling process in the SCE algorithm enhances survivability and improves global convergence efficiency, since better parameter sets are preferred over worse ones [Duan et al., 1993; Mboh et al., 2011].

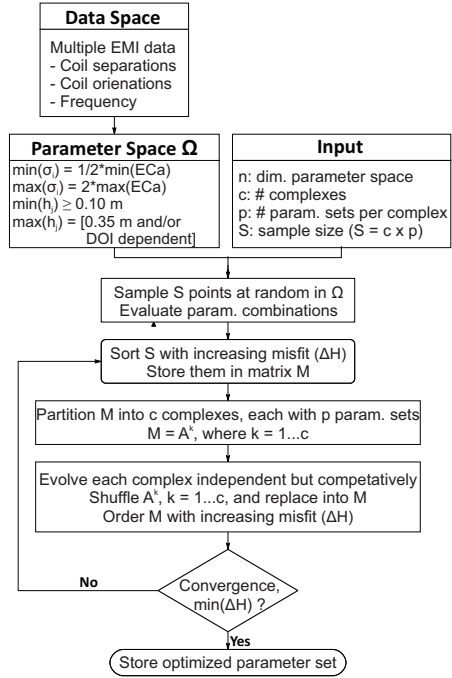


Figure 2.2: Flowchart of the SCE inversion algorithm for multi-coil EMI data.

Note that the implemented SCE algorithm optimizes the large-scale multi-coil EMI data of each measurement position separately, i.e., assuming a horizontally n-layer model. Large-scale high resolution EMI measurements require numerous inversions that run parallelized currently on the IBG-3 (Institute of Bio- Geoscience, Agrosphere, Forschungszentrum Jülich) computer cluster coded in GNU OCTAVE.

### 2.2.2 Differential evolution adaptive metropolis (DREAM<sub>ZS</sub>)

The differential evolution adaptive metropolis (DREAM<sub>ZS</sub>) algorithm presented by Laloy and Vrugt [2012] is a global optimization in a Bayesian framework, i.e., maximizing the probability of a parameter set while minimizing the misfit between measured and modeled data.

The posterior probability distribution,  $p(\mathbf{mp}|\mathbf{dta})$  to derive the medium parameters  $\mathbf{mp}$  given the multi-coil EMI device data  $\mathbf{dta}$  can be approximated as follows, see Linde and Vrugt [2013]

$$p(\mathbf{mp}|\mathbf{dta}) \approx p(\mathbf{mp})L(\mathbf{mp}|\mathbf{dta}), \quad (2.12)$$

where  $p(\mathbf{mp})$  is the prior distribution of the medium parameters and  $L(\mathbf{dta}|\mathbf{mp})$  is the likelihood function that summarizes the statistical properties of the misfit in a single scalar value [Linde and Vrugt, 2013], hence it quantifies whether the measured data would have been observed given the medium parameters.

To judge the misfit, the likelihood function needs an explicit formulation. For example, the  $L_2$ -norm likelihood function of Tarantola [2005] was used to derive the soil moisture distribution from GPR data [Linde and Vrugt, 2013] and a  $L_1$ -norm likelihood definition was used to jointly invert longwave EM and ERT data [Rosas-Carbajal et al., 2013].

Here, a log-likelihood definition similar to Linde and Vrugt [2013] is used to maximize the probability of medium parameters explaining the data

$$l(\mathbf{mp}|\mathbf{dta}) = -\frac{D}{2}\ln(2\pi) - \sum_{d=1}^D \ln(SN_d) - \frac{1}{2} \sum_{d=1}^D \left( \frac{|H_d^{meas} - H_d^{mod}(\mathbf{mp})|}{SN_d} \right)^2, \quad (2.13)$$

where  $SN_d$  describes the measurement standard deviation of each coil configuration. On the right-hand side, the first two terms are constants, while the third term describes the misfit between the measured magnetic fields and those modeled for possible medium parameter sets.

To sample the parameter space, Markov-Chain-Monte-Carlo (MCMC) methods are best suited since the described inverse problem is non-linear and relatively high dimensional. Typically, many thousands of model evaluations are required to converge to the posterior probability distribution [Bikowski et al., 2012], where the DREAM<sub>ZS</sub> algorithm, referred to as DREAM in the remainder of this thesis, was designed for efficient parameter space exploration.

The DREAM algorithm runs multiple chains in parallel and uses sampling from an archive of past states to generate candidate points in each individual chain [Laloy and Vrugt, 2012]. The algorithm automatically tunes the scale and orientation of the proposal distribution during sampling and has been shown to work well for a wide range of problems [Vrugt et al., 2009]. Here, the MATLAB (The MathWorks, Inc.) version is used to obtain the global minimum and to study the most likely parameter sets with respect to uncertainty.

## Chapter 3

# Conversion and Post-Calibration for Quantitative Inversion of Electromagnetic Induction Data beyond the LIN Approximation<sup>1</sup>

---

<sup>1</sup>adapted from von Hebel et al. [submitted to Geophysics]

## Overview

Commonly a linear relationship based on the low induction number (LIN) approximation is used to convert between the magnetic field and the apparent electrical conductivity, whereas the dependency is non-linear, see e.g., the analytical Equations 2.3 to 2.5 for homogeneous half-spaces, which results in discrepancies between the true ground electrical conductivity and ECa. This chapter describes a new conversion approach introduced as exact ECa conversion (EEC) that overcomes this limitation and is valid beyond the LIN approximation. Next, the established post-calibration method based on inverted electrical resistivity tomography (ERT) data [Lavoué et al., 2010] is discussed and used to derive universal calibration parameters that allow post-calibration without an ERT reference line. The established methods and novelties are then compared using multi-coil EMI data inversions. The present chapter exemplarily shows and analyzes the VCP and HCP coil modes, whereas the results can be extended for PRP coils.

### 3.1 Conversion between Magnetic Field and Apparent Electrical Conductivity

The LIN approximation of the analytical Equations 2.4 and 2.5 for low induction numbers ( $N_b$ ) obtains a linear relation between the magnetic field ratio and ECa [McNeill, 1980], where the same expression is obtained for the VCP and HCP coil configurations. Computing synthetic data using the analytical and the LIN based equations, discrepancies were observed [McNeill and Bosnar, 1999; Callegary et al., 2007; Beamish, 2011; Delefortrie et al., 2014] for 'relatively large' induction numbers [McNeill, 1980; Hendrickx et al., 2002]. This discrepancy is expected to increase even more for a layered subsurface, since the LIN approximation assumes a homogeneous half-space such that novel approaches are required to fully capture the earth response to an EMI device.

### 3.1.1 Low induction number (LIN) -based conversion

The induction number  $N_b$  is defined as the ratio between the coil separation and the skin depth ( $N_b = s/\delta$ ), compare Section 2.1.1. When using the low induction number approximation, where  $s \ll \delta$  or equivalently  $N_b \ll 1$ , the analytical Equations 2.4 and 2.5 of a homogeneous half-space result in

$$\left(\frac{H_S}{H_P}\right) \approx \frac{\omega\mu_0 s^2 \sigma}{4} j. \quad (3.1)$$

This LIN approximation shows that for very small  $N_b$ , the secondary magnetic field lags  $H_P$  approximately by the 90° emf shift [McNeill and Bosnar, 1999] such that the signal is imaginary or quadrature. Equation 3.1 is given by McNeill [1980] and the basis of several commercial EMI systems returning apparent electrical conductivities. Rearranging Equation 3.1 and assuming that  $\sigma = \text{ECa}$  obtains

$$\text{Im}\left(\frac{H_S}{H_P}\right) \approx \text{ECa} \frac{\omega\mu_0 s^2}{4}, \quad (3.2)$$

which uses the fact that the imaginary part of  $H_S/H_P$ , i.e.,  $\text{Im}(H_S/H_P)$  is linear proportional to the ground electrical conductivity and can be used to model the VCP and HCP magnetic field ratios, indicated in the following as the LIN-FM. Note that the above LIN-FM, Equation 3.2, is valid only when the ground is homogeneous,  $N_b \ll 1$ , and the coil pairs are at zero height above the surface [McNeill, 1980; Hendrickx et al., 2002; Delefortrie et al., 2014]. It is often used to convert the magnetic field ratio into ECa.

### 3.1.2 Comparison of exact EM-FM and LIN model

To investigate the differences between the exact EM-FM data for homogeneous half-space (Equations 2.4 and 2.4) and the LIN-FM (3.2), data for an EMI device with  $s = 1$  m and  $f = 30$  kHz over half-spaces up to 100 mS/m were computed. The exact EM-FM data and the LIN data are indicated in Figure 3.1a for the induction numbers  $N_b = 0.02, 0.04, 0.08, 0.09$  and 0.11. Although the LIN approximation returns the same quadrature value for the VCP and HCP modes, it is clear from Figure 3.1a that for the

small induction numbers the LIN approximation returns too large quadrature values compared to the exact signals, which can also be observed in the time representation shown in Figure 3.1b. In Figure 3.2, the quadrature component of the LIN-FM and the

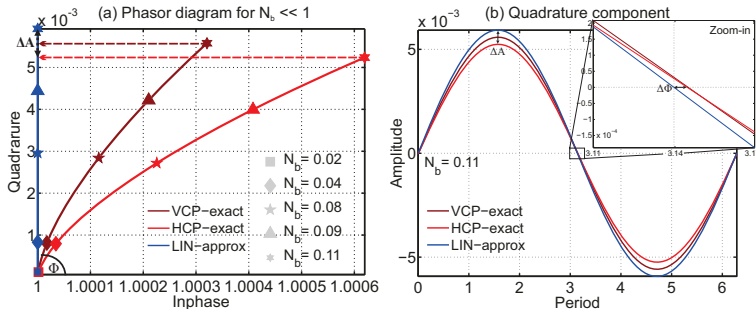


Figure 3.1: (a) Phasor diagram for exact computed VCP and HCP magnetic field components and their LIN representation showing differences in amplitude  $A$  and phase  $\Phi$  for some  $N_b \ll 1$ . In (b) observe the difference in amplitude ( $\Delta A$ , large plot) and phase ( $\Delta\Phi$ , zoom-in) between the exact EM-FM and the LIN model of the quadrature components for  $N_b = 0.11$ .

exact EM-FM formulation are compared for the VCP and HCP mode in the left and right column, respectively, with  $\text{Im}(H_s/H_P)$  as function of the electrical conductivity, with  $s = 1$  m and  $f = 30$  kHz (Figure 3.2a and 3.2b), as function of the coil separation,  $\sigma = 10$  mS/m and  $f = 30$  kHz (Figure 3.2c and 3.2d), and as function of the frequency,  $\sigma = 10$  mS/m and  $s = 1$  m (Figure 3.2e and 3.2f). Note that  $N_b \ll 1$  in all cases. As already indicated when discussing Figure 3.1, the LIN-FM overestimates the magnetic field ratios in all cases, with larger errors for the HCP compared to the VCP mode and non-linear discrepancies can be observed that will also be reflected in the true ECa [Beamish, 2011]. The relative error, plotted in each figure on the right y-axis, shows increasing error for increasing coil separation, electrical conductivity or frequency. The largest error increase was obtained for the coil separation since  $s$  is linearly related to the induction number, whereas the frequency and electrical conductivity are related to  $N_b$  by a square root, see Equation 2.6 together with Equation 2.2. Note that errors of about 18% for  $s = 4$  m (Figure 3.2d) and 13% for  $\sigma = 100$  mS/m (Figure 3.2b) were obtained. These results show the limited range where the LIN model has low errors; for low electrical conductivities ( $\sigma < 12$  mS/m [Beamish, 2011]), small transmitter frequencies (within the low-frequency limit [Callegary et al., 2007]), and especially for small coil separations. Any use of Equation 3.2 beyond these restrictions will result in inaccurate ECa values and limits the otherwise flexible use of multi-coil EMI devices.

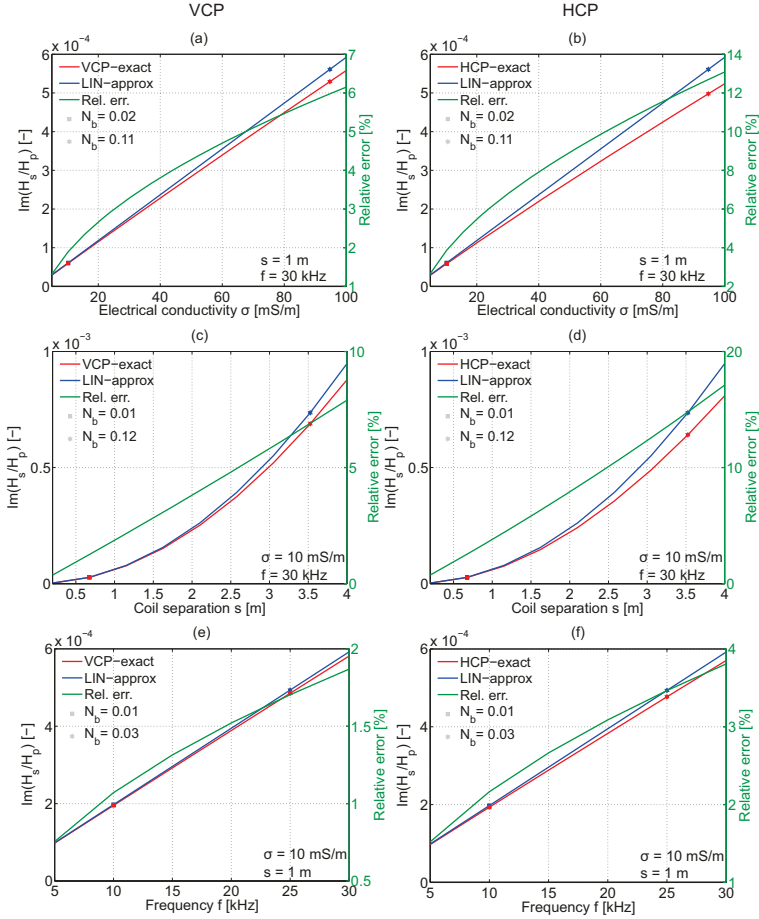


Figure 3.2: Quadrature component of the LIN-FM and exact EM-FM for VCP (left column) and HCP (right column) for a homogeneous earth with (a),(b) increasing half-space electrical conductivities  $\sigma$ , (c),(d) increasing coil separations  $s$  and (e),(f) increasing frequencies  $f$ . The device settings fulfill the LIN conditions such that  $N_b \ll 1$ .

### 3.1.3 Exact non-linear ECa conversion (EEC)

The formerly observed errors require a more accurate conversion method to obtain accurate EMI data that is being optimally used by the commercial multi-coil EMI devices. Here, a non-linear conversion method is developed, which accurately converts the magnetic field ratios into ECa introduced as the exact ECa conversion (EEC).

Instead of using the linear Equation 3.2 to convert the magnetic field ratio into ECa, the EEC approach proceeds as follows. EEC minimizes the error between the imaginary

part of the synthetic or experimental magnetic field ratio and the imaginary part of the magnetic field expression for a homogeneous half-space (Equations 2.4 and 2.5), to estimate the optimum ECa value that best fits the measured magnetic field ratio, as

$$\min \left[ \operatorname{Im} \left( \frac{H_P + H_S}{H_P} \right)_{syn.,exp.}^{VCP,HCP} - \operatorname{Im} \left( \frac{H_P + H_S}{H_P} \right)^{VCP,HCP} (ECa) \right], \quad (3.3)$$

where the non-linear numerical solver `fsolve` in MATLAB was used to find the optimum ECa.

To check the performance of this EEC approach, the LIN-based conversion (Equation 3.2) and EEC (Equation 3.3) are used to convert the magnetic field ratios computed by the exact EM-FM into ECa. Figure 3.3 shows the results for the VCP and HCP modes for  $f = 30$  kHz and different coil separations for a range of half-space electrical conductivities. Whereas the LIN-based conversion showed an increasing error between the true electrical conductivity and the obtained ECa for increasing coil separation and half-space electrical conductivity, the EEC approach obtained ECa values that were equal to the true  $\sigma$  showing an accurate performance of EEC.

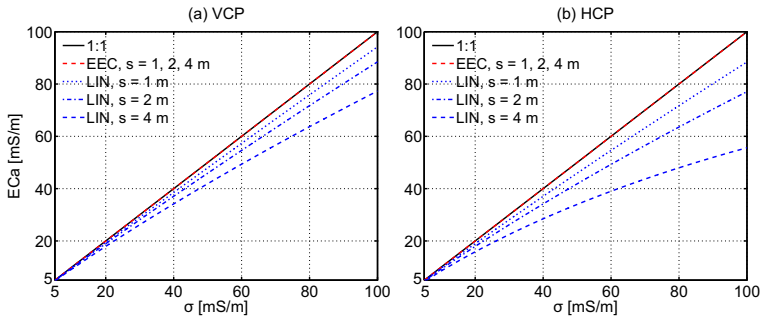


Figure 3.3: Exact ECa conversion (EEC) and LIN based method for (a) VCP mode and (b) HCP mode for different  $s$  with increasing  $\sigma$ . While the LIN based method (blue lines) deviates with larger errors for larger  $s$  from the black 1:1 line, the EEC method (red lines) match it, indicating that EEC performs accurately.

Next, the EEC approach was extended to an  $n$ -layered earth. Equations 2.8 to 2.10 were used to compute the magnetic field ratios for a homogeneous earth (model 1), and three-layered earth with increasing (model 2) and decreasing (model 3)  $\sigma$  with depth as well as a saline example (model 4) for an EMI device with  $s = 1$  m and  $f = 30$  kHz. Table 3.1 shows the obtained ECa values using the LIN-based conversion and EEC.

Table 3.1: ECa values obtained using the LIN-based conversion and EEC for homogeneous and three layer models with increasing and decreasing  $\sigma$  with depth. The magnetic field ratios were computed for an EMI device with  $s = 1$  m and  $f = 30$  kHz using Equations 2.8 and 2.9.

Model	$\sigma_1, \sigma_2, \sigma_3$ [mS/m]	$h_1, h_2$ [m]	VCP			HCP		
			EEC [mS/m]	LIN [mS/m]	Error [%]	EEC [mS/m]	LIN [mS/m]	Error [%]
1	10		10.0	9.8	1.8	10.0	9.6	3.7
2	10, 20, 50	0.3, 0.5	23.0	22.3	2.8	32.8	30.6	6.6
3	50, 20, 10	0.3, 0.5	30.9	29.9	3.2	19.6	18.6	5.1
4	20, 100, 500	0.3, 0.5	137.7	128.3	6.8	240.7	197.7	17.9

Since the EEC approach uses the full solution of a homogeneous half-space to search for an ECa equivalent to a horizontally layered earth, the obtained ECa values better represent the magnetic field data than the linear LIN-based conversion. Similar to the results of Figure 3.2, the LIN-based conversion underestimates the ECa values. The relative errors were larger for the HCP than for the VCP mode because the HCP mode is more inclined than the VCP mode in the phasor diagram (see Figure 3.1), which results in larger deviations from the asymptote.

The error of the presented examples increased up to around 18% with increasing  $\sigma$ . Note that in Figure 3.3 the errors increased with increasing coil separation indicating that the errors dramatically rise when EMI devices with larger  $s$  are used and/or the subsurface is relatively high electrical conductive, e.g., in clay rich or saline areas such that the EEC approach seems preferable to the LIN-based conversion.

### 3.2 Synthetic Multi-Coil EMI Data Inversion using LIN-based Conversion and EEC

To strengthen the above indications, synthetic multi-coil EMI data were inverted. Prior inversion, the magnetic field ratios of the previous models 2 and 3 (increasing and decreasing  $\sigma$  with depth, respectively) were computed for the CMD-MiniExplorer (ME) geometry, i.e., three coplanar receivers with  $s = 0.32, 0.71$  and  $1.18$  m referred to as  $s32, s71$  and  $s118$  using the exact EM-FM, Equations 2.8 and 2.9. These were exactly converted into ECa to obtain accurate ECa values and reconverted into magnetic field ratios using the LIN-based conversion and the EEC approach.

To invert the data (synthetic here and experimental later), the shuffled complex evolution (SCE) algorithm of Section 2.2.1 was used to optimize the five medium parameters  $[\sigma_{1,2,3}, h_{1,2}]$ . The parameter space for  $\sigma_{1,2,3}$  was spanned by taking half of the smallest and doubling the largest calibrated ECa values. For  $h_{1,2}$ , the minimum was set to 0.1 m. The maximum for  $h_1$  was 0.35 m and  $\max(h_2)$  varied between 0.4 and 1.2 m with a default of 0.76 m due to the ME sensitivity, see Figure 1.1a.

The inversion results were evaluated using the normalized absolute model misfit

$$\Delta\sigma = \frac{1}{N} \sum_{k=1}^N \left| \frac{\sigma_k^{true} - \sigma_k^{inv}}{\sigma_k^{true}} \right|, \quad (3.4)$$

where  $\sigma^{true}$  and  $\sigma^{inv}$  are the true model and the inverted electrical conductivities, respectively, and  $k = 1 \dots N$  are centimeter depth increments to implicitly account for the layer thickness deviations.

Table 3.2 shows the inversion results, where the inverted  $\sigma$  distribution using the EEC approach was closer to the true model than the LIN-based conversion as reflected by the smaller model misfits. In the case of decreasing  $\sigma$  with depth, the obtained deviation was possibly due to the limited near surface sensitivity of the EMI device used in this study.

Table 3.2: Three-layer models SCE inversion results using LIN-based and EEC converted data including model misfit of increasing and decreasing electrical conductivity models.

Parameter: / Method	$\sigma_1, \sigma_2, \sigma_3$ [mS/m]	$h_1, h_2$ [m]	$\Delta\sigma$ [%]	Parameter: / Method	$\sigma_1, \sigma_2, \sigma_3$ [mS/m]	$h_1, h_2$ [m]	$\Delta\sigma$ [%]
<b>Model 2</b>	10.0, 20.0, 50.0	0.3, 0.5		<b>Model 3</b>	50.0, 20.0, 10.0	0.3, 0.5	
EEC	10.0, 19.8, 49.9	0.3, 0.5	1.4	EEC	50.0, 22.0, 10.6	0.3, 0.4	9.6
LIN	9.8, 13.5, 61.4	0.2, 0.7	25.0	LIN	50.2, 21.6, 12.0	0.3, 0.4	14.6

Extending the coil configurations with shallow sensing PRP coils ( $s = 1.1$  and  $2.1$  m) exactly reconstructed both models based on EEC because the highest sensitivity of PRP coils at the ground interface, see Figure 1.1, resulted in a better near surface differentiation. Consequently, more coil configurations and/or varying coil angles as shown by Guillemoteau and Tronicke [2015] enhance the imaging capabilities, which improves when using the EEC approach.

### 3.3 Post-Calibration of Multi-Coil EMI Data

#### 3.3.1 ECa shifts in EMI measurements

Several EMI devices require an on-site zero leveling (field calibration) procedure at regular time intervals to obtain reliable EMI measurements in the field, whereas newer multi-coil EMI devices such as the ME, or the DualEM-421 of DualEM, Milton, Canada (DUEM) are factory calibrated. However, external conditions such as metal fences, cables or GPS systems close to the device as well as temperature, solar flares and/or humidity can influence the device's measurement behavior [Gebbers et al., 2009; Suduth et al., 2003] and generate additional magnetic fields that are being sensed by the device. Also the presence of the operator influences the measured EM response [Nüsch et al., 2010].

To investigate the influences on EMI measurements carried out with the ME that has an accuracy of 4% (at 50 mS/m) [GF-Instruments, 2011], ECa values were recorded along a transect with the device either fixed to a crutch and carried close to an operator or mounted on a sled. When different operators carried the EMI device along the transect, the differences were around 1 mS/m. Next, the influences of the field setups were compared using either the crutch (sensor carried close to the operator) or the sled (pulled with about 2 m distance between operator and sled).

Figure 3.4 shows the recorded ECa values for both field setups as cross plots for the VCP and HCP mode with increasing coil separation from top to bottom. The linear regressions, given in the legends of the figures, returned coefficients of determination ( $R^2$ ) larger than 0.98 proving that the measurements strongly correlate, which is of course to be expected since the measurements were carried out along the same transect. The scaling factors were close to one showing that mainly data shifts were present between the field setups. The ECa shifts were significant and around 10 mS/m for the small coil separations. The decreasing data shifts with increasing coil separation indicate a smaller influence of the external conditions to the superimposed secondary magnetic compared to the contribution of the increasing subsurface volume being sensed.

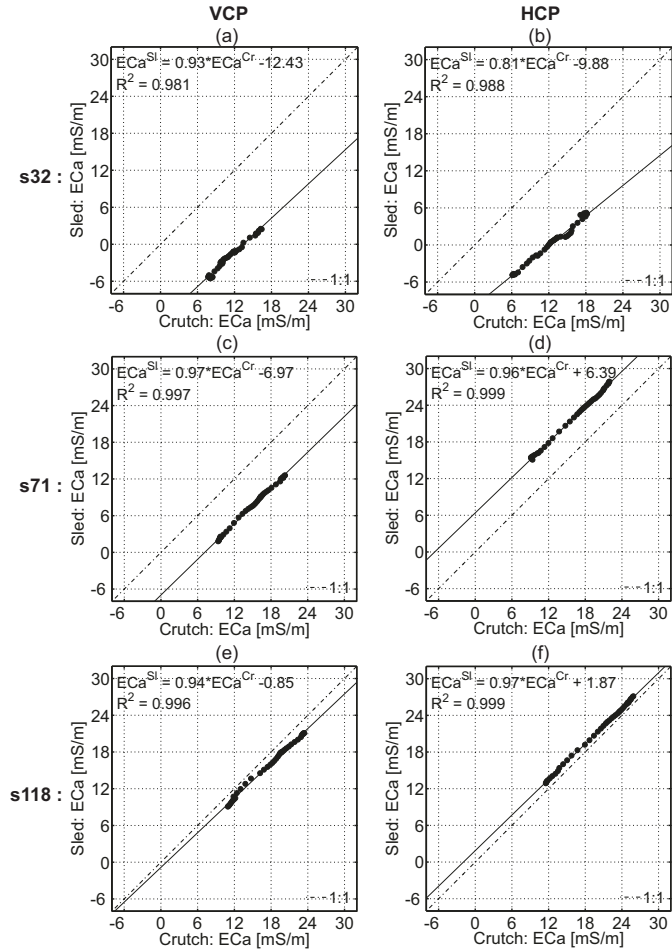


Figure 3.4: ME multi-coil ECa values recorded with crutch (Cr) and sled (Sl) field setup along a transect. VCP in the left and HCP in the right column with increasing s from top to bottom.

These results show the generally strong influence of the field setup on the recorded ECa values such that the sleds were standardized with respect to the equipment. The handheld is attached to a pole at 0.6 m above the EMI device and the GPS system at 1 m height on top. Also, a straight data cable connecting the device and the handheld is used to reduce the possible influence of a winded wire. Nevertheless, ECa shifts remain such that EMI data require a post-calibration to obtain quantitative ECa values that can be used for reliable inversions.

### 3.3.2 Site specific ECa post-calibration using electrical resistivity tomography (ERT)

All the performed measurements used the standardized field setup to record EMI data as similar as possible. To correct the remaining ECa shifts, collocated EMI and ERT measurements are performed along a calibration line of 30 m length having lateral changes in ECa. The post-calibration based on ERT data of Lavoué et al. [2010] was successfully used to invert quantitative EMI data of relatively long ( $> 100$  m) transects [Mester et al., 2011; Minsley et al., 2012]. A suitable calibration line shows a large ECa range that is identified in the beforehand recorded large-scale ECa maps, which are plotted in the field. The selected line represents the ECa distribution of the test site as shown in Chapter 4. If such a line cannot be identified, more transects need to be measured to cover the entire ECa range [Altdorff et al., 2016].

To obtain an ERT model along a 30 m calibration line that can be used to calibrate the multi-coil EMI data, ERT measurements are performed by using a Syscal Pro (IRIS Instruments, Orléans, France) with 120 electrodes using a Dipole-Dipole electrode array with 0.25 m spacing. The Dipole-Dipole electrode array was selected because it was found to be most useful to measure the electrical conductivity changes in the lateral direction [Kirsch, 2009] while resolving the shallow subsurface. The ERT data are inverted using RES2DINV (Geotomo software, Malaysia) with the Robust inversion scheme that uses the  $L_1$ -norm and tends to produce locally constant regions with sharp layer boundaries.

A rectangular region that matches the EMI depth of investigation (estimated by 1.5-s of the largest coil separation) is selected from the trapezoidal ERT tomogram. The obtained electrical conductivity distributions are inserted into the exact EM-FM (Equations 2.8 and 2.9), to model the magnetic field ratios that are accurately converted into ECa using the EEC approach. A linear regression between the predicted and measured ECa ( $ECa^m$ ) values that were recorded in steps of 0.5 m along the calibration line returns regression/calibration parameters (scale and shift) that are necessary to obtain quantitative ECa ( $ECa^g$ ) values.

So far, 43 of these calibration measurements were performed and analyzed. Here, Figure 3.5 shows a cross-plot between measured and predicted ECa for two representative test sites. Site 1 (red dots), measured at the Scheyern research farm close to Munich, showed ECa values ranging from around 0 mS/m for the shallowest to 45 mS/m for the deepest sensing coil configuration. The predicted data ranged from 15 to 70 mS/m. Hence, this calibration line showed a relatively large lateral and vertical ECa range, which resulted in coefficients of determination (see figure legends) larger than 0.87.

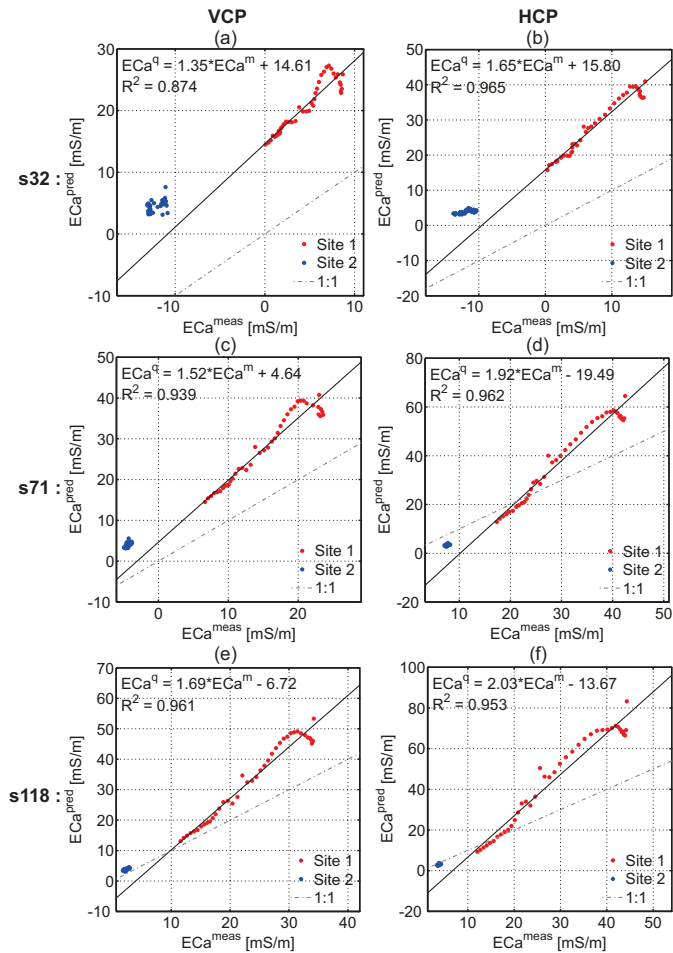


Figure 3.5: Calibration data examples for VCP and HCP with increasing  $s$  from top to bottom in the left and right column, respectively.

In contrast, site 2 (blue dots), which is a forest soil [Altdorff et al., submitted], showed measured ECa values lying close to each other and a very small data range. Also the predicted values showed maximum ECa values of 6 mS/m and narrow ranges of 3 mS/m, indicating a low ground electrical conductivity and low vertical and lateral variations along the calibration line. This resulted in point clouds that cannot be used to perform a linear regression to calibrate these data. These observations indicate a failing calibration using a linear regression when either the measured or the predicted ECa range is  $< 3$  mS/m and/or when the ground electrical conductivity is  $< 5$  mS/m.

### 3.3.3 Deducing universal calibration parameters

Many of these calibration measurements were performed at various test sites and dates. From these data, eight calibration lines were selected having  $R^2 > 0.75$  in the linear regressions between measured and predicted ECa of collocated ERT and EMI data recorded in VCP and HCP mode. These data were measured with the same sled and setup between March and September 2012 at test sites of arable land, bare soil and grass land in Germany as listed in Table 3.3. The following investigates the presence of universal calibration parameters.

Table 3.3: Test sites, coordinates of the field midpoints, land use and figures where the data were used.

Test Site	Field	Date	x-UTM 32U	y-UTM 32U	Land use	Figure
Selhausen	F01 <sup>a</sup>	03/08/12	320996	5638079	arable	3.6, 5.6
Selhausen	F02	26/07/12	321112	5638470	arable	3.6
Selhausen	F09	08/08/12	320612	5638327	bare soil	3.6
Selhausen	F10east	29/06/12	320583	5638370	bare soil	3.6
Selhausen	F10west <sup>b</sup>	29/06/12	320583	5638370	arable	3.4, 3.6, 4.4
Scheyern	F03 <sup>c</sup>	20/03/12	680039	5374017	arable	3.5, 3.6, 3.8
Rollesbroich	F02March	30/03/12	309525	5611541	grass land	3.6
Rollesbroich	F02Sept	10/09/12	309525	5611541	grass land	3.6
Klein Altendorf	-	13/08/12	358137	5608978	arable	3.9

<sup>a</sup>[Rudolph et al., 2015], <sup>b</sup>[von Hebel et al., 2014], <sup>c</sup>[van der Kruk et al., 2015]

Figure 3.6 shows the scale and shift calibration parameters and the obtained  $R^2$  of the selected calibration lines as well as the data of the forested site 2 shown in Figure 3.5. All data nicely lined up from relatively low to relatively high ECa values, which is especially the case for the larger VCP and HCP s71 and s118 coil configurations.

Performing separate linear regressions returned similar regression parameters. Performing one linear regression including all the data returned  $R^2$  values larger than 0.95. These high  $R^2$  values indicate that universal calibration parameters were present that can be used to post-calibrate any EMI data, when recorded with the same device and using the same field setup and data processing. Observe that the point clouds for the forest site 2 were also close to the regression lines indicating that these data might also be calibrated by using a shift only.

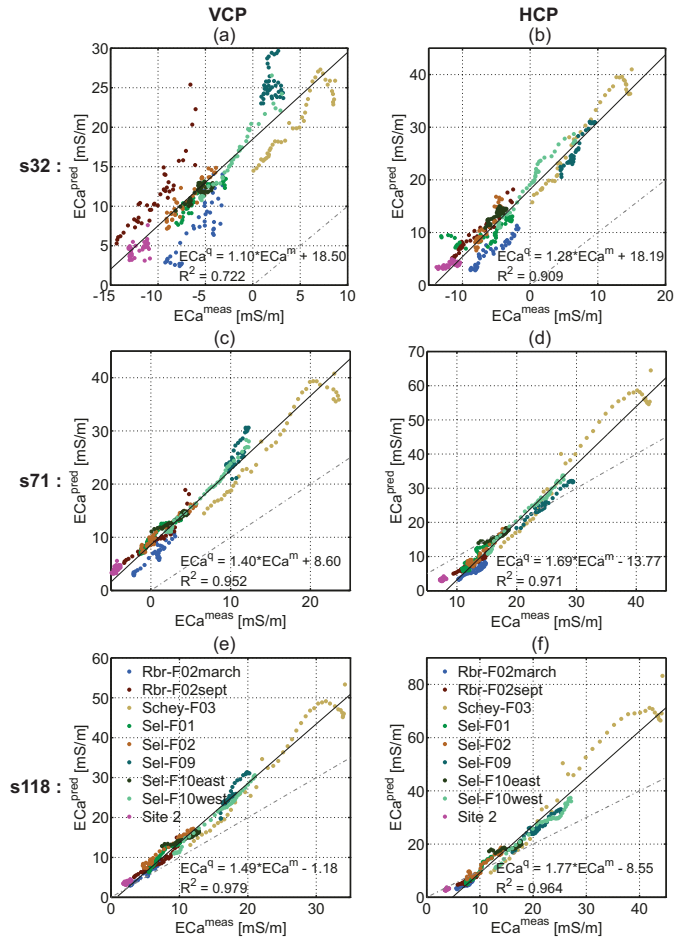


Figure 3.6: Linear regression through VCP (left column) and HCP data (right column) of various test sites and dates using the sled field setup to investigate the presence of universal calibration parameters. Also shown the point clouds of the forested site 2 presented in Figure 3.5.

The very shallow (0-0.25 m) sensing VCP-s32 coil configuration showed a relatively wide spread around the regression line reflected by the lowest  $R^2$  value of 0.72. The spread is probably also caused by the larger soil heterogeneity in the shallow subsurface that limits the assumption of a horizontally layered earth. However, as shown next, the sensitivities of the EMI and ERT for a horizontally layered earth indicate another possible explanation. Figure 3.7 compares the sensitivities of VCP-s32 and HCP-s32 with the Dipole-Dipole electrode array sensitivity used in this study for a horizontally layered earth. Similar to the HCP sensitivity curve, a zero sensitivity at the interface can be observed for ERT when assuming point electrodes [Roy and Apparao, 1971; Roy, 1972; Barker, 1989; Szalai, 2000].

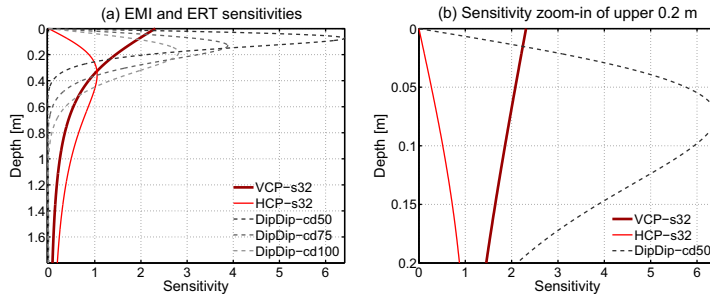


Figure 3.7: (a) Dipole-Dipole sensitivity for three smallest dipole center distances versus VCP and HCP local sensitivities. In (b) Sketch-up of the smallest Dipole-Dipole-cd sensitivities and EMI sensitivities of the upper 0.2 m.

In addition, the use of finite length electrodes reduces the measured potential difference compared to the assumed point electrode case, systematically biasing the apparent electrical conductivity values lower for progressively shorter electrode spacings [Igel, 2007]. These factors explain why it is more difficult to calibrate the very shallow sensing VCP-s32 coil configuration with ERT results for the very shallow subsurface (i.e., over the upper 5-10 centimeters). Here, more research is needed to understand how the very shallow subsurface changes are sensed by the small VCP coil configuration.

### 3.4 Quantitative Transect Inversions of Experimental Multi-Coil EMI Data

In the following, post-calibrated multi-coil EMI data are inverted using the LIN based conversion and the EEC approach. Thereafter, the deduced universal calibration parameters are applied to obtain quantitative ECa values without using an additional (laborious) on-site ERT measurement, where the EMI data were obtained using the standardized field setup and data processing.

#### 3.4.1 Inversion using LIN-based conversion and EEC

Similar to the synthetic data, the inversion results of experimental data acquired at the Scheyern test site using the LIN-based conversion and the EEC approach are compared. Along a 30 m calibration line, the EMI device observed lateral changing ECa values. The ERT reference profile, shown in Figure 3.8a, showed a relatively low electrical conductive upper soil layer of around 0.25 m thickness that was overlying a moderate electrical conductive soil layer. Between 5 and 17 m, the subsurface consisted of a three-layered earth with increasing electrical conductivities with depth. The moderate electrical conductive second layer lay above a high electrical conductive lowest zone separated by a sharp boundary at around 1 m depth. The electrical conductivity of the lowest zone decreased between 17 and 20 m and changed into a two layer system with a low electrical conductive upper layer above a moderate electrical conductive lower zone. From 20 to 25 m, an upward dipping low electrical conductive soil underlay the moderate electrical conductive layer and reduced its thickness.

The inverted ERT data (electrical conductivity distribution) of every 0.5 m was used to predict the magnetic field ratios measured by the EMI device along the profile and converted into ECa using either the LIN-based conversion or EEC, which were then used to post-calibrate the EMI-ECa before inversion. Figure 3.8b shows the SCE inversion results when using the LIN-based conversion. The absolute differences compared to the ERT reference model are shown in Figure 3.8c and an average mean absolute error of 8.6 mS/m with a standard deviation of 12.3 mS/m was obtained. The model misfit  $\Delta\sigma$ , Equation 3.4, was evaluated at each position with a mean value of  $0.45 \pm 0.23$ .

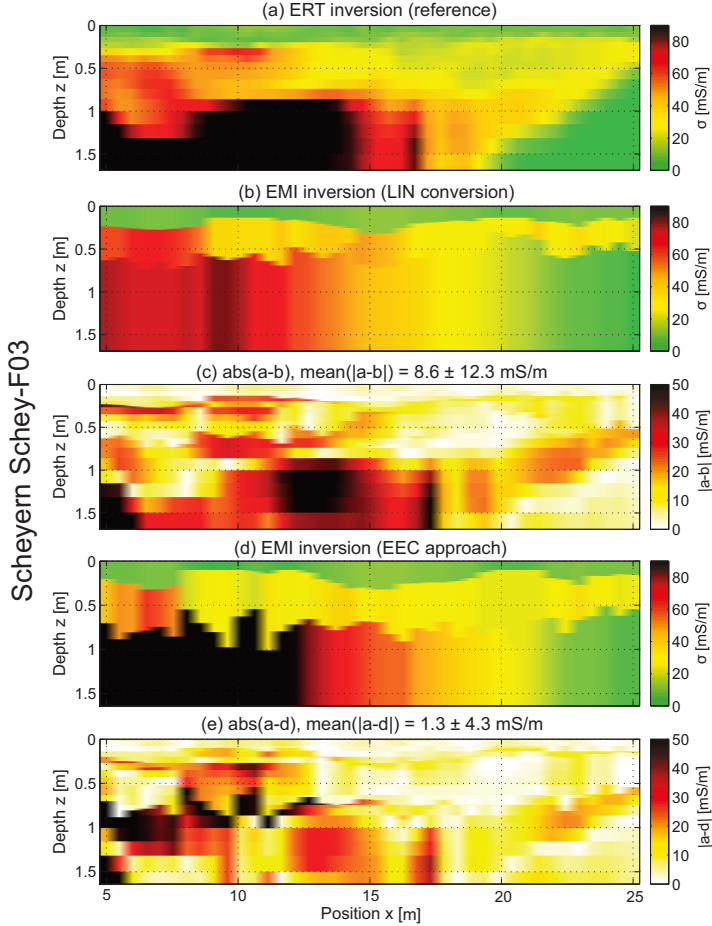


Figure 3.8: Inversion results of (a) ERT data as reference, (b) EMI data using LIN conversion with (c) corresponding difference matrix, (d) EMI data using exact ECa conversion and (e) corresponding difference matrix.

The inversion results using the EEC approach and the corresponding absolute difference plot are shown in Figure 3.8d and 3.8e, respectively. A visual inspection shows a better coincidence with the quantitative electrical conductivities obtained by ERT as the inversion results when using the LIN-based conversion. The better fit with the ERT reference model was also reflected in the mean absolute difference of  $1.3 \pm 4.3$  mS/m and a mean  $\Delta\sigma$  of  $0.42 \pm 0.27$ . These results show that when using post-calibrated EMI data and the EEC approach, inversion results are obtained that well reflect the subsurface properties within the limitation of a three-layer inversion.

### 3.4.2 Inversion of universal calibrated EMI data

The former section showed that EMI data need post-calibration. This calibration can be performed using a 30 m transect that contains data with a sufficiently large ECA range (see Site 1 in Figure 3.5). Here, the universal calibration parameters deduced in Figure 3.6 were applied to EMI data measured over a transect where almost no lateral variations in ECA could be observed such that the site specific calibration resulted in a point cloud and could not be used for calibration purposes (similar to the site 2 data shown in Figure 3.5). Figure 3.9a shows the inverted ERT results that roughly showed a two layered system with a relatively low electrical conductive upper layer of 1 m thickness and a lower zone with relatively high electrical conductivities.

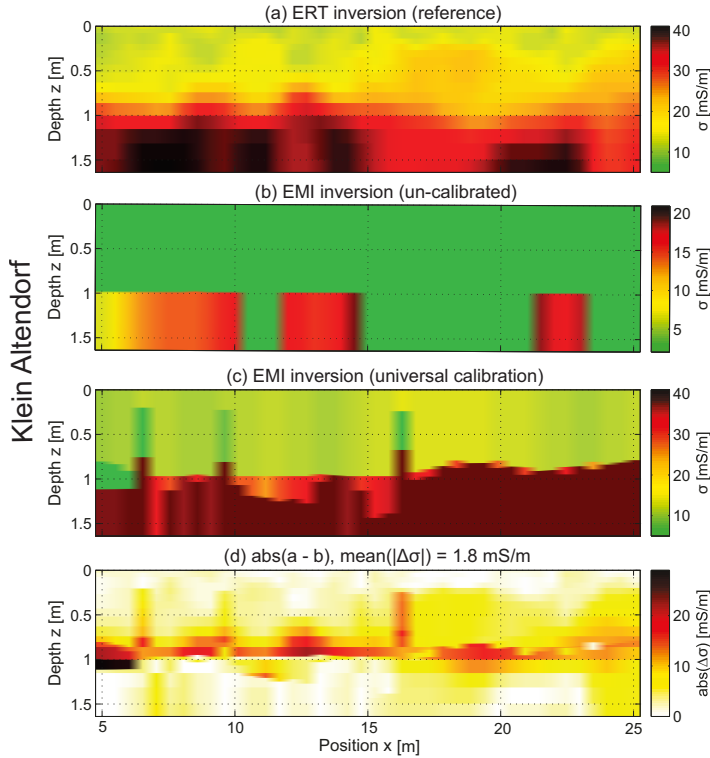


Figure 3.9: Inversion results of (a) ERT, (b) un-calibrated EMI data, (c) universally calibrated EMI data and (d) the corresponding difference of the Klein Altendorf test site, where no site specific calibration was achievable.

Figure 3.9b shows the inverted subsurface model of un-calibrated EMI data that differed completely from the ERT reference model indicating the need of calibration as also discussed by Mester et al. [2011] and shown in the following Chapter 4. Figure 3.9c shows the EMI inversion results when using the universal calibration parameters of Figure 3.6 and Figure 3.9d shows the absolute difference to the ERT reference. Whereas the ERT inversion results mainly showed a two-layered model, the three-layer EMI inversion also returned a mainly two-layered model that approached the quantitative electrical conductivity changes of the ERT results, which was also reflected in relatively low mean absolute difference values of  $1.8 \pm 3.1$  mS/m and mean  $\Delta\sigma$  of  $0.22 \pm 0.05$ . Similar deviation values were obtained when inverting quantitative EMI data calibrated using a site specific ERT-based post-calibration as presented in Figure 3.8. These results show the applicability of the universal calibration parameters to obtain quantitative ECa that can be inverted in combination with the EEC approach to get reliable quantitative images of the subsurface.

### 3.5 Conclusions

This chapter discussed in detail how to improve the handling of EMI data by introducing the non-linear EEC approach that is valid beyond the LIN approximation, while accurately converting the magnetic field ratios into ECa. The post-calibration based on ERT data and subsequent inversion resulted in quantitative transect images, where the ECa values matched the range of the entire test site. If such a line is not identifiable, the alternative post-calibration approach that is based on vertical electrical sounding (VES) data as shown in a separate Appendix A can be used. Note that the presented VES-based post-calibration approach includes PRP, VCP and HCP coils that sense up to 6 m depth.

The calibration approaches obtain coil specific calibration parameters by linear regressions between measured and predicted EMI-ECa that can be applied to large-scale data, which obtains quantitative areal ECa values that enable quasi-3D EMI-inversions that are expected to improve when including the EEC approach.



## Chapter 4

### Quasi-3D Test Site

### Characterization Using Inverted

### Quantitative Multi-Coil

### Electromagnetic Induction Data<sup>1</sup>

---

<sup>1</sup>adapted from von Hebel et al. [2014]: Three-dimensional imaging of subsurface structural patterns using quantitative large-scale multi-configuration electromagnetic induction data

## Overview

In the current chapter, multi-coil EMI data were inverted to resolve large-scale 3D subsurface structures. The recorded ECa values were post-calibrated following the approach of Section 3.3.2 and processed with a novel filter strategy. RegridDED quantitative ECa data of each grid node were independently inverted using the parallelized three-layer SCE code of section 2.2.1 that run on the JUROPA supercomputer of Forschungszentrum Jülich. The obtained results were validated by independent grain size distribution maps and previously performed ERT measurements.

### 4.1 Selhausen Bare-Soil Field

The bare-soil field (32U 320583 5638370 UTM) is located in the southern part of the Lower Rhine Embayment in North-Rhine-Westphalia, close to Selhausen (Germany), and is part of TR32 (TransRegional Collaborative Research Center) and of TERENO (TERrestrial ENvironmental Observatories). TR32 investigates the complex patterns in soil-vegetation-atmosphere systems to improve general modeling concepts in the view of global climate change. TERENO is a long-term research programme to catalogue the ecological, social and economic impacts of global change at a regional level.

The size of the bare-soil field is about 60 m in North-South (N-S) and 190 m in East-West (E-W) direction. It is weakly inclined toward the West with a slope of around 4° at the steepest part between 100 and 150 m E-W, see Appendix Figure B.1a. The sediments are Quarternary, which are mostly fluvial deposits from the Rhine/Meuse and Rur river system covered by floodplain sediments from the Pleistocene and Holocene. Generally, the topsoil water content is lower in the eastern than in the western part of the test site and the groundwater table fluctuates seasonally but is typically below 3 m depth [Weihermüller et al., 2007].

The soil type of the bare-soil was described as silty loam according to the USDA textural classification with a distinct gradient in soil texture (coarse to fine) from East to West. Figure 4.1 shows the grain size distribution of the upper 0.3 m sampled at a 10 by 10 m soil sampling grid. The eastern part of the test site is mainly composed of coarse

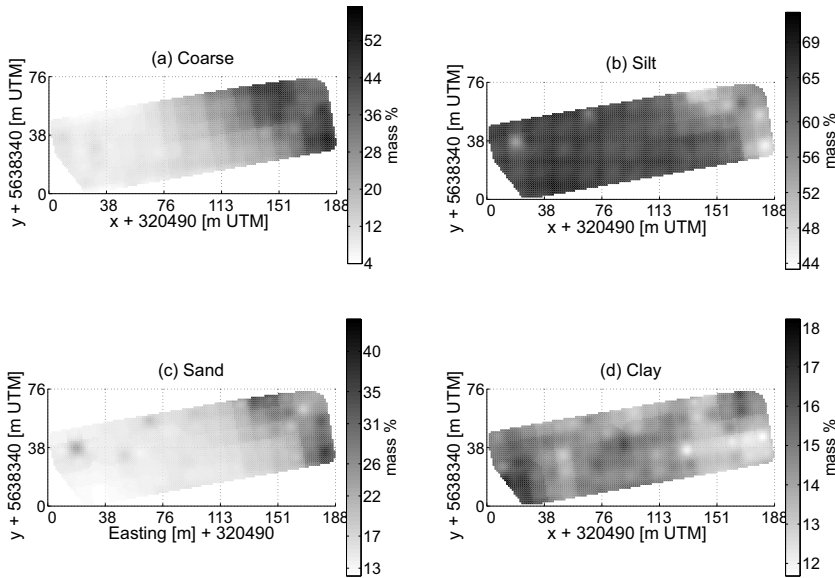


Figure 4.1: Grain size distribution for a 10 by 10 m coarse grid of the upper 30 cm depth at the bare-soil field. a) Coarse fraction, b) silt, c) sand, d) clay. The distribution shows a clear trend over the entire test site with a higher gravel content in the eastern part and variably distributed sand, silt and clay rich areas toward the West.

material ( $> 2$  mm) with a mass fraction up to 50% and a considerable amount of sand. Toward the West, the silt and clay content increase up to 69 and 18%, respectively.

## 4.2 EMI and ERT Data Acquisition

EMI measurements were carried out at the Selhausen bare-soil field on 29<sup>th</sup> June 2012 using the CMD-MiniExplorer (ME) housing three coplanar coils (s32, s71, and s118) to sense different but overlapping sensing volumes up to approximately 1.8 m depth, where Figure 4.2 shows the complementary sensitivities of the VCP and HCP coils. The VCP mode shows the largest sensitivity to near-surface layers and no sensitivity at deeper depths, while the HCP mode shows no sensitivity at the near-surface and highest sensitivities for deeper depths.

Before the measurements, the EMI device was acclimated to outside temperature using a 30 minute warm-up time and then pulled on a wooden sled, see Figure 5.2a, behind an all-terrain-vehicle (ATV) at approximately 6 to 8 km/h. The recordings

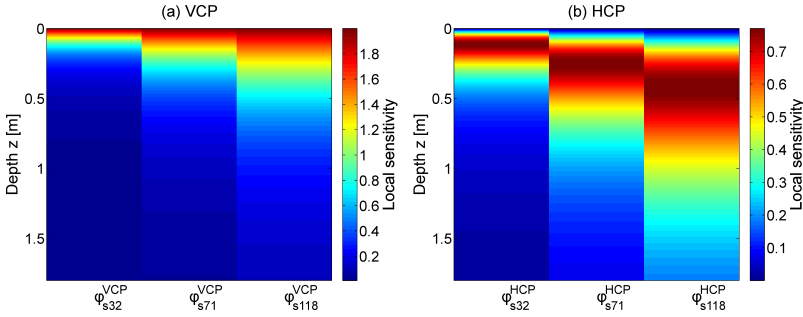


Figure 4.2: (a) VCP and (b) HCP local sensitivities vs. depth for the CMD-MiniExplorer (ME) s32, s71 and s118 coil configurations.

were carried out with a sampling rate of 10 Hz, hence ECa data were measured every 16 to 18 cm. Over the whole survey area, first east-western tracks with about three meter distance and thereafter perpendicular tracks with about 13 m distance were continuously recorded first in VCP and then in HCP mode. Each coil configuration measured very similar ECa values at the intersections of the tracks, which indicates that no time drift occurred in the data. In total, six high-resolution data sets each with approximately 55000 measurements were recorded and simultaneously georeferenced with a single frequency global positioning system (GPS) using the standard positioning service. The total acquisition time of the 1.1 ha large area was 4.5 h including warm-up time as well as assembling and disassembling the equipment.

To calibrate the EMI data, a suitable 30 m transect with strong lateral variations of soil apparent electrical conductivity (referred to as the 2012-transect in the following) was identified in the large-scale EMI measurements. On this calibration line, EMI and ERT data were consecutively acquired as described in the calibration section 3.3.2. The ERT data set contained 6715 measurements at various depth levels down to 3.4 m and the acquisition time of the 30 m line was about three hours, including installation, data acquisition, and removal of electrodes and cables.

On 28<sup>th</sup> May 2009 and 21<sup>st</sup> October 2010, 120 m long ERT transects were measured using a 15 m overlap roll-along procedure at two different locations by Lavoué et al. [2010] and Busch et al. [2014]. The locations of the 2009-, 2010-, and 2012-transects are shown in the Appendix, Figure B.1b. Whereas the 2012-transect was used for post-calibration and as a reference for the EMI-inversion, the 2009-, and the 2010-transect

was used as an independent validation of the quasi-3D EMI-inversion results.

### 4.3 Data Processing and Filtering

The recorded ERT data were filtered using the automatic filtering and deviation filter, set to 2.5%, provided by PROSYS II (IRIS Instruments, Orleans, France). The subsequent data set was inverted using RES2DINV with the Robust inversion scheme.

Since the EM-FM used in the n-layer SCE inversion scheme assumes a horizontally layered earth, novel filter strategies were implemented to remove EMI data measured at locations where strong lateral heterogeneity is present. The 2012-transect (calibration line) EMI data were processed by excluding values larger and smaller than the median plus/minus two times the median absolute deviation. The excluded values were replaced using linear interpolation between neighboring values. To flatten peaks in the data, a 5 point (or 2.5 m) simple moving average was applied.

Large-scale EMI data are rarely normally distributed [Minsley et al., 2012], although required in most filter strategies. To overcome this limitation, a novel histogram-filter to identify and exclude outliers was developed. The histogram-filter bins the EMI-ECa into 15 equally spaced containers and computes the percentage of the data within each container. A bin containing less than 0.5% of the data is considered to carry outliers and is thus removed. This filter strategy effectively removes outliers without assuming a normal distribution. In addition, strongly laterally varying ECa values were excluded, when the deviation between the actual and adjacent recordings exceeded 1 mS/m. Finally, a 10 point moving average, i.e., one 10 Hz sampling term, smoothed the filtered data. Due to filtering, the six multi-coil EMI data sets were unequally long and thus interpolated with a nearest neighbor approach to a common grid with 1.25 m in each spatial direction.

## 4.4 Results and Discussion

### 4.4.1 Calibration and three-layer inversions of transect data

The EMI data measured along the 2012-transect that was identified in the large-scale measurements is presented in Figure 4.3a. Here, the six coil configurations (3 coil offsets for VCP and HCP modes) showed increasing  $EC_a$  values with increasing sensing depth ranging from approximately 1 mS/m for the very shallow sensing VCPs32 coil to about 25 mS/m for the deepest sensing HCPs118 coil at the beginning of the transect. Toward the end of the calibration line, a decreasing trend with a drop of about 5 to 10 mS/m was observed for all coil configurations indicating a structural change along the 2012-transect. Note that even negative values were measured pointing toward the need for calibration.

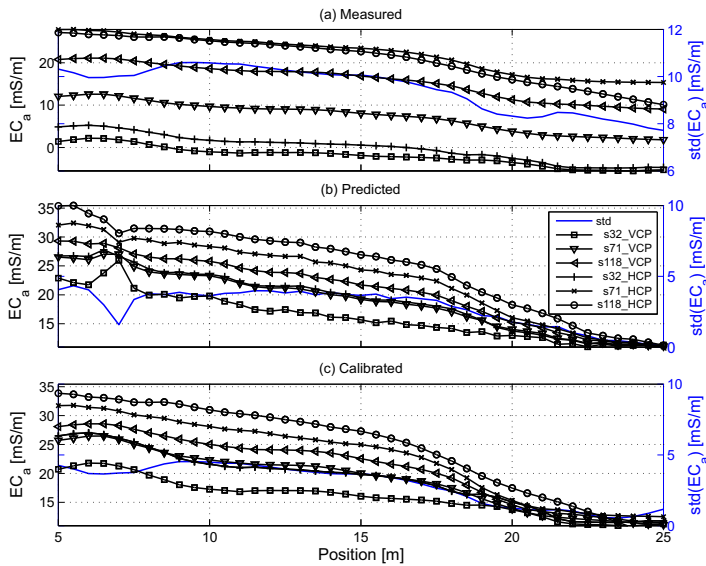


Figure 4.3: (a) Measurements smoothed with a simple moving average over five positions, (b) predicted EMI- $EC_a$  using inverted ERT data as input in the EM-FM (Equations 2.8 and 2.9) and (c) post-calibrated EMI data using linear regression parameters (see Figure 4.5). Note that (b) and (c) show a similar  $EC_a$  range, whereas (a) shows a similar trend but different range. The blue lines are the standard deviations at each position, where a small deviation indicates more uniform soil conditions.

The colocated ERT measurement showed a high repeatability, since the mean quality factor of the raw data was 0.33% and the standard deviation 2.53%. The applied filtering discarded 1.44% (97 out of 6715) of the data. The subsequent data set was inverted and the absolute error was 1.6% after five iterations. This indicates that the ERT data were described well by the inverted subsurface electrical conductivity model (Figure 4.4b). Note that the first and last five meter of the ERT transect are not presented because the inversion results are less reliable here. Moreover, the depth range of the presented ERT inversion result is reduced to match the maximum EMI sensing depth (see Figure 4.4a).

To indicate the EMI sensing volume, the definition of McNeill [1980] is used for the vertical dimension, whereas the sensing radius of Callegary et al. [2012] was considered for the lateral dimension, i.e., approximately 1.5-s. A comparison of EMI sensing volumes (Figure 4.4a) with the corresponding ERT sensing volumes ( $\approx$  electrode distance divided by 2, Figure 4.4b) clearly shows that for small and large electrode distances the EMI sensing volume is larger or smaller, respectively. To avoid that inverted ERT images are overly smoothed in the lateral direction (i.e., more than the maximum lateral EMI sensing dimension of about 2 m), the small Dipole-Dipole arrays with a small electrode spacing and a Robust Inversion approach was used, that previously showed to function, see Chapter 3. Moreover, this inversion approach results in piecewise constant electrical conductivity areas that approximately match the size of the EMI sensing volume. Nevertheless, future work should explore which ERT acquisition strategies are best suited for EMI calibration.

Inversion results for uncalibrated EMI data are presented in Figure 4.4a. Evidently, this inversion result does not match the electrical conductivity distribution obtained by the ERT inversion results shown in Figure 4.4b. Next, the EMI data were post-calibrated using the inverted ERT data as input in Equations 2.8 and 2.9 to predict ECa values for the three ME coil separations in VCP and HCP mode, respectively, along the calibration line. Compared to the measured EMI data, the predicted ECa curves shown in Figure 4.3b have similar shapes but different quantitative values.

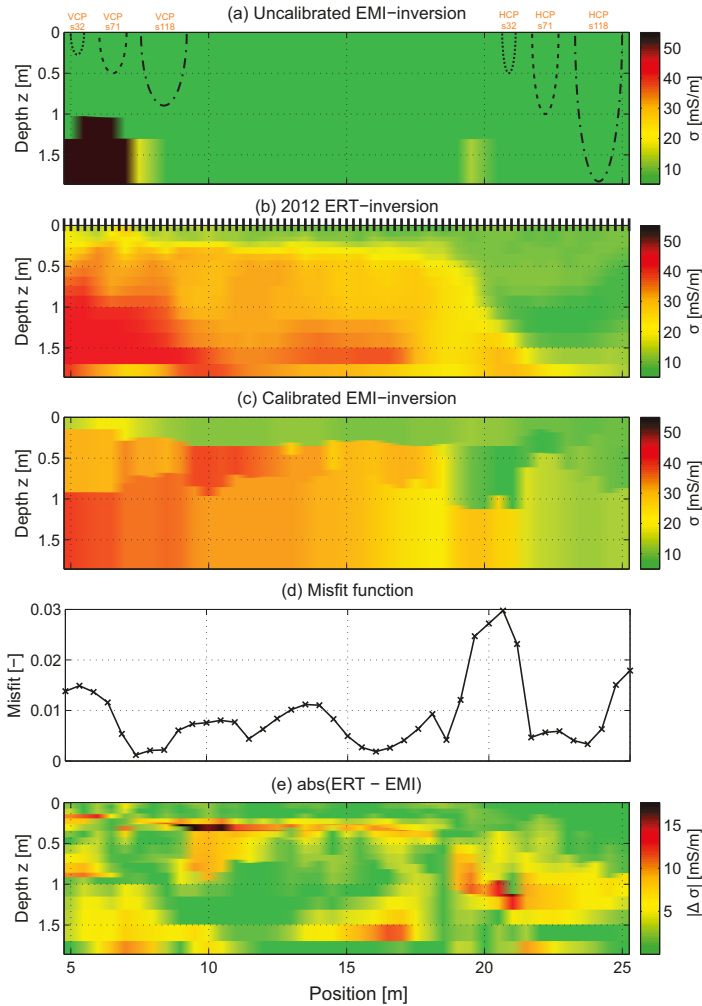


Figure 4.4: (a) Inversion of uncalibrated EMI data and ME sensing volumes for s32, s71 and s118 for VCP (left) and HCP (right), (b) ERT-reference and calibration line and electrode array with 0.25 m spacing, (c) inversion of calibrated EMI data, (d) corresponding data misfit, Equation 2.11, and (e) absolute difference between ERT and EMI.

To investigate the difference between the measured and predicted ECa values in more detail, these ECa values are plotted against each other in Figure 4.5. The left column shows the VCP mode while the right column shows the HCP mode with increasing coil separation, s32, s71 and s118, from top to bottom. The predicted data have mostly larger ECa values compared to the measured data such that a clear deviation from the 1:1 line is observed. Hence, the measured EMI data were biased and not suitable

for inversion (as shown in Figure 4.4a). The bias was removed by a linear regression between measured and predicted ECa for each coil configuration, which returned  $R^2$  values larger than 0.93 in all cases (see Figure 4.5). The obtained regression parameters (scale and shift) are provided in the legends of Figure 4.5 and indicate that each coil configuration requires a specific calibration to remove the bias from the measured EMI data.

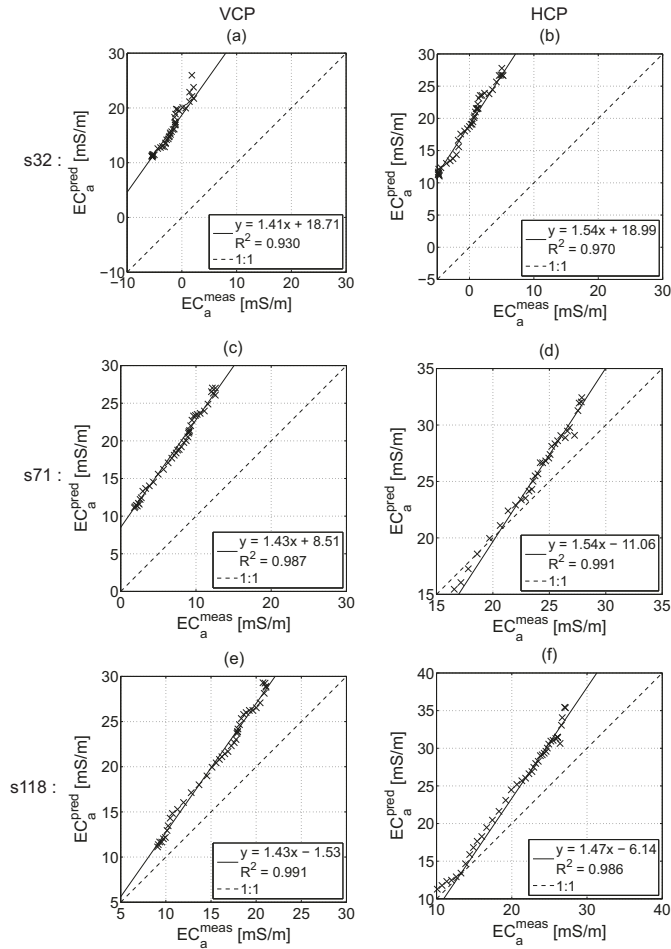


Figure 4.5: Linear regression plots for measured and predicted data of each coil separation for VCP in (a), (c) and (e). The HCP mode is shown in (b), (d) and (f). Two coil specific regression parameters (scale and shift), indicated in the legends, calibrate the EMI data. Note the coefficients of determination ( $R^2$ ).

To investigate the bias, Table 4.1 shows the mean absolute deviation (MAD) between the uncalibrated and calibrated data, which was largest for the small coil offsets with values up to 19 mS/m. Therefore, these corrections are dominant over a possible bias due to uncertain ERT inversion results that have a minor influence compared to the post-calibrations needed to obtain reliable ECa values.

Figure 4.3c shows the calibrated EMI data that are now very similar to the predicted curves presented in Figure 4.3b. Analyzing the standard deviation of all ECa values as a measure for the variation of the electrical conductivity with depth, relatively small values were observed be-

tween 20 and 25 m indicating a more homogeneous subsurface, whereas the larger standard deviation between 5 and 20 m provides a strong indication for a layered subsurface, since the ECa values increase with increasing DOI. These homogeneous and layered parts of the calibration line are also clearly visible in the ERT inversion (Figure 4.4b), which provides confidence that the calibrated ECa values can now be considered accurate, unbiased and quantitative.

The calibrated ECa values of the six EMI coil configurations were inverted with the SCE inversion approach for a three-layer medium without regularization. The obtained results are presented in Figure 4.4c and show smoothly changing electrical conductivity values. Compared to the ERT inversion results, the shallow low conductivity layer with an electrical conductivity of 10 mS/m was well reconstructed by the EMI inversion in terms of absolute conductivity as well as layer thickness. For the deeper structures, the profile can be divided into three parts. A clear layering was found between 5 and 18 m. The SCE inversion scheme reasonably reconstructed the interface around 0.8 m depth for the first 5 to 9 m in terms of both layer thickness and electrical conductivity. Instead of an increasing electrical conductivity with depth as can be observed in the ERT data, a high conductive intermediate layer was obtained by the EMI inversion between 9 and 18 m, which is probably due to a limited sensitivity for the deeper layers of the coil configurations of the ME (compare the sensitivities, Figure 4.2).

Table 4.1: Mean absolute deviation (MAD) between calibrated and uncalibrated EMI data shown in Figure 4.3a and 4.3c.

Coil separation	MAD(calibrated, uncalibrated)	
	VCP [mS/m]	HCP [mS/m]
s32	19.0	17.9
s71	2.3	11.6
s118	3.8	5.1

The down-dipping transition zone between 18 and 22 m was approximated with an abrupt change of the electrical conductivity distribution in both lateral and vertical directions, because the inversion algorithm assumes a horizontally layered medium. Note that this region was associated with larger misfits between measured and modeled EMI data (Figure 4.4d), which indicates that the used model is not entirely appropriate to explain the data. This can only be resolved with a two- or three- dimensional EMI forward and inverse scheme, which will significantly increase the required computational resources. Between the last 22 to 25 m, a homogeneous electrical conductivity area was present in the ERT data that was also well reconstructed by the EMI-inversion.

Figure 4.4e shows the absolute difference between the ERT and the calibrated EMI inversion results. Here, it can be seen that the EMI inversions were well able to reconstruct the reference model, since almost 90% of the absolute electrical conductivities deviated less than the maximum MAD of 5.8 mS/m. Especially the shallow top layer was well reconstructed, whereas larger differences were present in the deeper subsurface. The largest deviations could be observed at the layer boundaries. On the one hand, this can be caused by the regularization used in the ERT inversion that smears the interfaces between adjacent structures, whereas the EMI inversion returns sharp layer boundaries. On the other hand, the EMI device has an accuracy of 4% and additional errors can occur during the interpolation on a regular grid.

#### 4.4.2 Quasi-3D inversions of quantitative large-scale EMI data

The obtained calibration parameters as shown in Figure 4.5 for the six coil configurations were applied to the filtered and re-gridded large-scale EMI data. The resulting calibrated ECa maps are shown in Figure 4.6 for the VCP and HCP mode in the left and right column, respectively, with increasing coil separation from top to bottom. For all EMI coil configurations, low ECa values around 5 mS/m were observed in the East indicating a relative homogeneous area. Beyond a sharp south-northern directed ECa boundary, higher ECa values were observed in the western part of the test site. This is consistent with the grain size distribution shown in Figure 4.1, where finer material was present in the western part and coarse material was present in the eastern part.

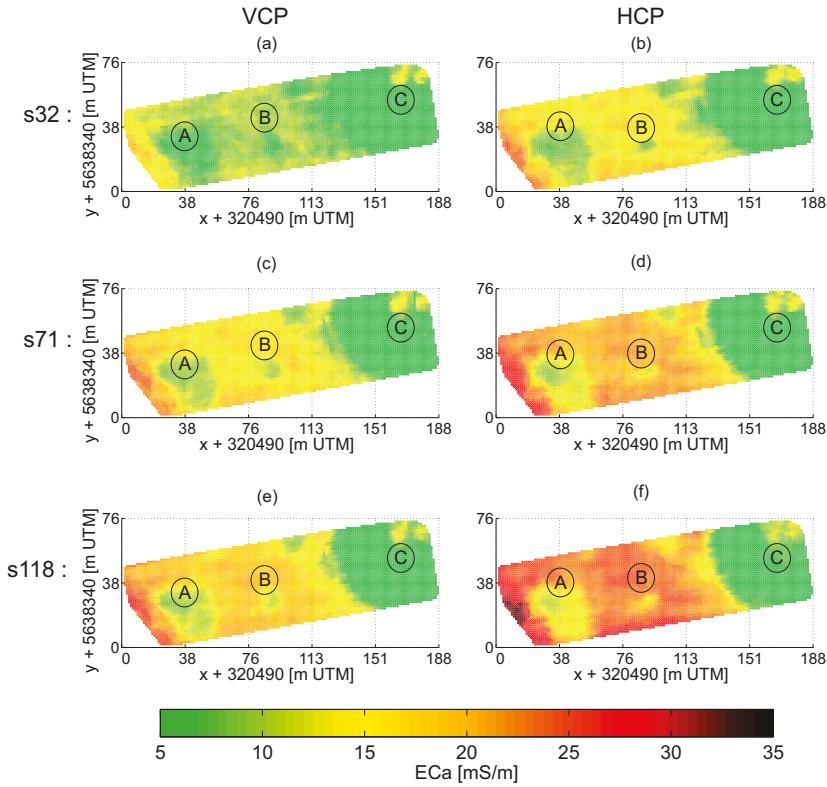


Figure 4.6: Quantitative ECa maps, histogram filtered and re-gridded, for VCP and HCP coil configuration for (a), (b) s32, (c), (d) s71, and (e),(f) s118.

In addition to these main patterns, three smaller contrasting zones can be distinguished; zone A has low ECa values for all coil configurations, which seems to coincide with a lower amount of clay shown in Figure 4.1d. Zone B shows low ECa values but was not observed in the grain size maps, Figure 4.1, and seem to not extend as deep as zone A because the ECa increased with the deepest sensing HCP coils compared to the shallower sensing configurations. Zone C seems to coincide with higher clay and silt contents shown in Figures 4.1b and 4.1d.

Although the measured EMI data are consistent with the soil textural information, it is important to note that the grain size distribution were obtained for the upper 30 cm on a 10 by 10 m coarse sampling grid, whereas the ECa values have been measured and re-sampled on a higher resolution grid such that high resolution information were obtained.

At each grid node, the six quantitative ECa values were inverted for a three-layer 1D electrical conductivity model. The results were stitched together to obtain a quasi-3D three-layer model of the electrical conductivity distribution of the subsurface. Figure 4.7 shows horizontal slices through the obtained model at three different depth levels (0.25, 0.55 and 1.55m). A movie of vertical depth slices running South to North through the three-dimensional electrical conductivity volume of the Selhausen test site can be found on the DVD provided with this thesis.

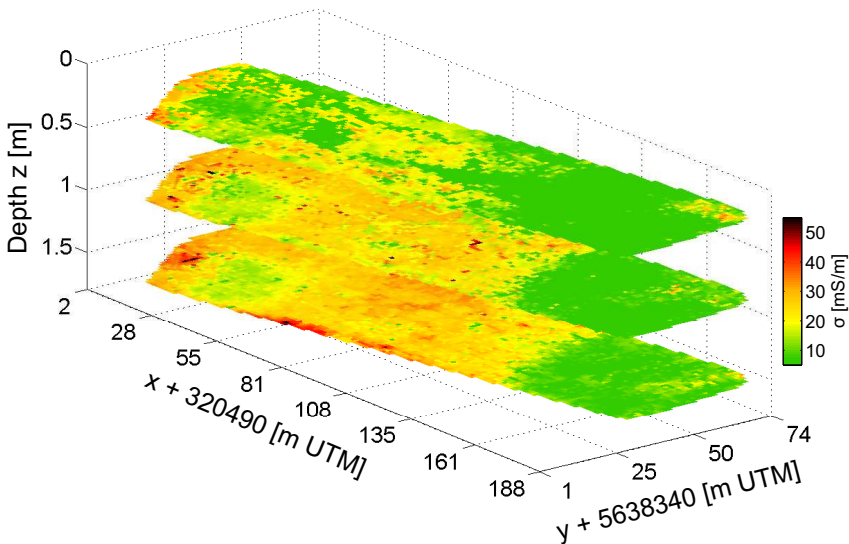


Figure 4.7: Horizontal depth slices at 0.25 m (ploughing zone), 0.55 and 1.55 m intersecting the main structures.

Figure 4.8 shows two vertical cross-sections through the quasi-3D electrical conductivity volume in the middle panel, where the ploughed layer of about 30 cm thickness can be clearly identified. As already indicated in the calibrated ECa maps, patch A clearly extends to larger depths than patch B. Figure 4.8 also presents a comparison between the inverted EMI data and the two independent 120 m long ERT transects measured in 2009 and 2010 in the lower and upper panel, respectively. Overall, the main electrical conductivity structures were remarkably similar. The lower panel clearly shows the patches A and B and the three-layer area in the West. In the upper panel, the noticeable transition of the two-layer medium to a homogeneous medium at about 120 m was found by the three-layer SCE inversion.

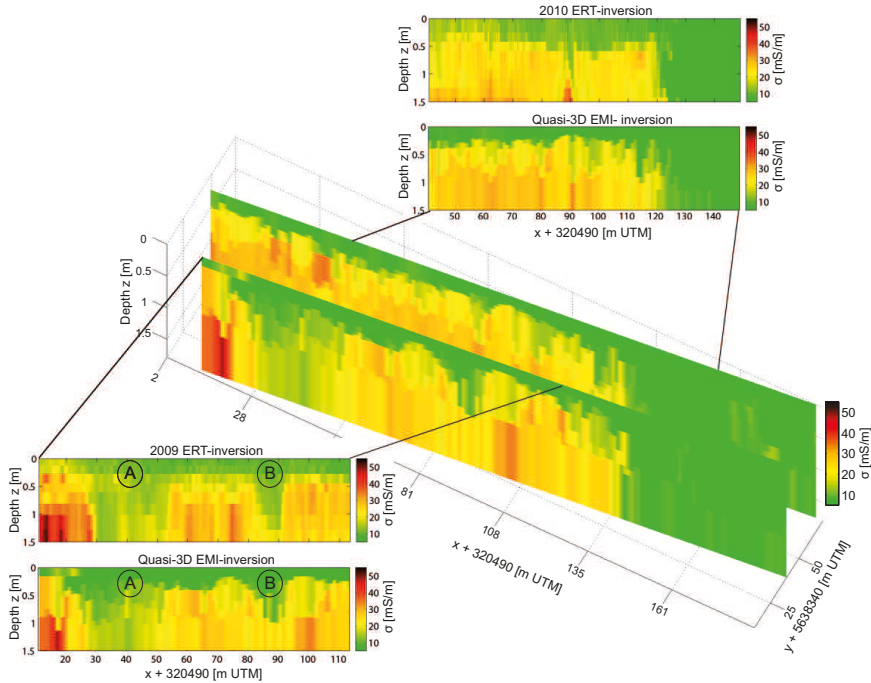


Figure 4.8: Quasi-3D inversion slices and close-ups validated with 2009-transect and 2010-transect. The quasi-3D EMI inversion reconstructs the main features and layer properties discovered by the ERT measurements performed in 2009 and 2010.

To conclude, the main structural patterns in the EMI and ERT data match well and are likely related to variations in soil texture. Remaining small scale differences are to be expected because the ERT and EMI measurements in Figure 4.8 were performed at different dates with different weather conditions. From 1<sup>st</sup> until 27<sup>th</sup> May 2009 in total 43 mm rain were observed, while the sum of precipitation from 1<sup>st</sup> until 20<sup>th</sup> October 2010 was up to 35 mm. In June 2012, it rained 75 mm until the 28<sup>th</sup> (see the weather data of June 2012 in the Appendix, Figure B.2) such that the soil was most probably drier in 2009 and 2010 than in 2012. However, in 2009 and 2010 about 5 and 8 mm precipitation were totally observed five days before the data acquisition, while only  $\approx 1$  mm rain occurred in the five days before for the 2012 survey. Since the soil water content contributes to the EMI signal, we assume that remaining differences in electrical conductivity values might be caused by differences in the soil states, indicating that in future studies, repeated large-scale EMI measurements during dry and wet conditions can be used to identify hydrologically active areas within the 3D volume.

## 4.5 Conclusions

The novel quasi-3D large-scale inversion algorithm for calibrated multi-coil EMI data returns three-layer models at each grid location assuming a horizontally layered earth, while revealing lateral and vertical structural electrical conductivity patterns, which are related to the observed variations in soil texture and soil water content. To obtain the soil water content, repeated large-scale EMI measurements and inversions at different soil states are needed such that the electrical conductivity changes and hence soil water dynamics within certain layers can be observed, which will be a future task.



## Chapter 5

# Imaging of Buried Paleo-River Channels by Joint Data Inversion of Multiple Electromagnetic Induction Devices

## Overview

The current chapter analyzes two campaigns performed at a test site that is characterized by buried paleo-river channels. In campaign I, the CMD-MiniExplorer (ME) recorded ECa values that were post-calibrated based on ERT data. This survey essentially revealed the paleo-river channels and the observed ECa patterns were related to the leaf area index (LAI) and to soil texture in general [Rudolph et al., 2015]. Here, the quantitative EMI-ECa values were inverted for three-layers that basically show the paleo-river channel structures within a limited depth resolution of the upper meter.

The depth of investigation was increased in campaign II, that aimed at improved vadose zone characterization by a joint inversion of multiple EMI device data that obtained the lateral and vertical paleo-river channel dimensions at selected transects. The EMI data were recorded with the ME plus the custom-made CMD-SpecialEdition (SE) and the DualEM-421 (DUEM). The extended coil configurations of up to 24 coils investigated depths up to 6 m and allowed to extend the SCE inversion code as described in Section 2.2.1 from three- to n-layers. The parallelized code run on the IBG-3 (Institute of Bio- and Geoscience, Agrosphere, Forschungszentrum Jülich) computer cluster using 27 processors with up to 2 GB RAM each. To perform quantitative inversions, the EMI-ECa values were calibrated using the novel post-calibration approach that is based on vertical electrical sounding (VES) data (detailed in the Appendix A). The obtained inversion results were validated with soil cores of relatively deep boreholes.

### 5.1 Selhausen Paleo-River Channel Field

The paleo-river channel field (32U 320996 5638079 UTM) is close to the bare-soil field and has an area of about 2.55 ha ( $\approx 170$  by 150 m). The test site is almost flat, see Figure 5.1a, around 1.7 km away from today's Rur river bed and is approximately 0.5 km apart from the bare-soil field presented in Chapter 4, see Figure 5.1b. Whereas two third of the bare-soil field are situated in the Lower Terrace (LT) consisting mainly of silty loam (see Figure 4.1), the paleo-river channel field lies in a sand and gravel dominated Upper Terrace (UT) [Rudolph et al., 2015].

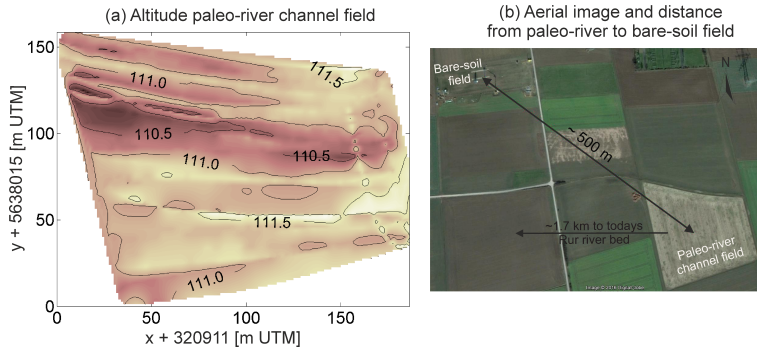


Figure 5.1: (a) Topography and (b) aerial image of the paleo-river channel field, where also the distance to the bare soil field of Chapter 4 is shown.

These sediments were deposited in the Pleistocene between the Early and High Weichselian glaciation ( $\approx 115000$  to  $13000$  years before present). Due to meltwater in the Late Weichselian and Early Holocene, the ancient Rur river formed breakaways and secondary channels [Milbert, 2016]. Within these channels, finer material was transported with a relatively low flow rate compared to the main course. As time went by, the secondary channels dried up, leaving the finer material in the gravelly surrounding, and aeolian sediments covered the paleo-river remnants.

## 5.2 EMI Field Setup

Between the two surveys campaign I and campaign II, the EMI field setup changed. Whereas in campaign I the ME was placed in a wooden sled, new sleds were constructed together with the ZEA-1 (Central Institute for Engineering, Electronics and Analytics, Engineering and Technology, Forschungszentrum Jülich) for the ME and the newly purchased and custom-made CMD-SpecialEdition (SE) as well as for the DUALEM-421 (DUEM). The new sleds were made of plastic to suppress any influence of current conducting media close to the EMI devices, while being robust, stable, and easy to assemble. The wooden and the new plastic sleds are presented in Figure 5.2.

The ME and the SE carry three and six coplanar receiver coils, respectively, and the DUEM houses three perpendicular plus three coplanar receiver coils in one unit, see Table 2.1, such that up to 24 coil configurations investigate the subsurface with different

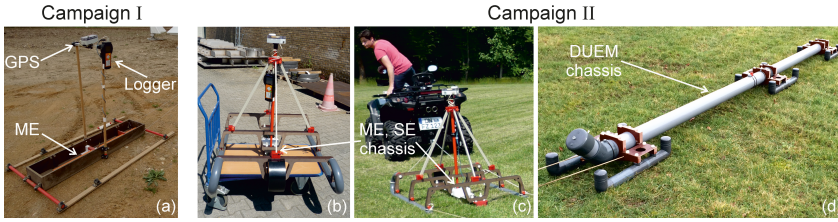


Figure 5.2: (a) Wooden sled of the ME used for the bare-soil survey in Chapter 4 and in campaign I, (b), (c), and (d) show the newly constructed plastic sleds of the ME, SE, and DUEM, respectively, that were used in campaign II.

but overlapping sensing volumes. All sensitivities are presented in Figure 5.3a and 5.3b for the shallow sensing VCP/PRP and the deep sensing HCP coil configurations, respectively, showing that the multiple devices are complementary and highly resolve the upper 3 to 4 m depth.

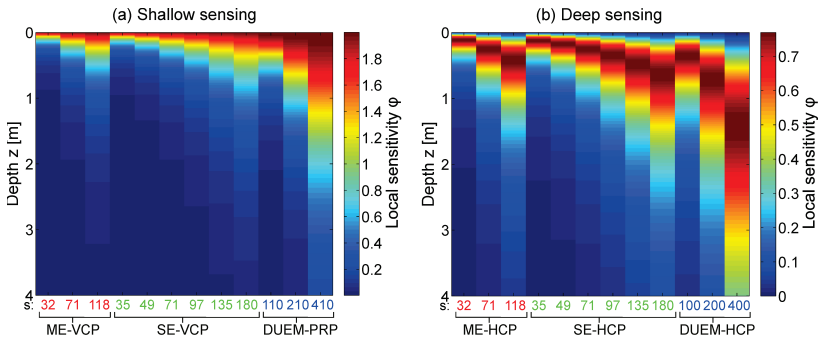


Figure 5.3: (a) Shallow and (b) deep sensing coil configurations of CMD-MiniExplorer (ME), CMD-SpecialEdition (SE), and DualEM-421 (DUEM)

## 5.3 EMI Surveys

### 5.3.1 Large-scale data acquisition

Campaign I was performed with the ME in July 2012, where the large-scale measurements and data handlings were similar to those of the bare-soil field. The acquisition and processing steps are detailed in Section 4.2 and Section 4.3, respectively.

Campaign II took place in July and August 2015. Before the actual survey, a synthetic study was performed to balance between survey duration and the obtained infor-

mation. Since the ME and the SE carry coplanar coils, the study sought the optimum device combination to resolve the structures by the large-scale inversions in one go. Based on the campaign I and the bare-soil field results, the study (presented in Figure B.3) showed an optimum device arrangement to characterize the paleo-river channel field and possibly the surrounding area for future measurements when the ME record in VCP and the SE in HCP mode plus the DUEM, which results in 15 coil configurations that well resolve the upper 2 to 3 m depth.

To record the data, each EMI device was placed in the sleds and warmed up for approximately 30 min. The sleds were then pulled by an all-terrain-vehicle (ATV) with approximately 6 to 8 km/h and EMI data were recorded with a 5 Hz sampling rate using the ME-VCP and the SE-HCP mode (the DUEM failed to record) such that nine coil configurations delivered approximately 30000 ECa records for each receiver. The tracks were mainly East-West (E-W) directed with a distance of around 7 m. Sparse North-South (N-S) directed tracks with a distance of around 30 m were measured to observe possible temporal ECa drifts at the track overlaps.

The multi-coil EMI data were processed using the histogram-filter described in Section 4.3. To enable data inversion comparison, both the campaign I and campaign II ECa values were interpolated onto a common grid with 1.25 m node spacing using the MATLAB function `TriScatteredInterp` that performs a Delaunay triangulation between measurement positions to re-grid the data.

### 5.3.2 Transect measurements

During campaign II, transect data were acquired using all 24 coil configurations to invert for the paleo-river channel dimensions. Along two transects (T1 and T2) that were crossing the paleo-river channels (see in Figure 5.4), EMI data were continuously recorded with the 5 Hz sampling rate while a distant operator towed the sleds. For these data, more processing was required to obtain regular spaced (every 25 cm) ECa values due to the following reasons. As can be seen in Figure 5.2d, the DUEM sled had no option to attach a GPS system. Instead, a second operator carrying the GPS walked parallel to the sled. The speed of the sled dragging person and the GPS carrier differed, which resulted in a displacement between the GPS and the actual measurement

position. Occasionally, ECa values were recorded without moving the sled, which caused large positioning scatters due to the low accuracy and precision of the used single frequency GPS systems. Moreover, due to the different lengths of the three sleds (around 4.5 m for the DUEM, 2 m for the SE and 1.2 m for the ME), the start and stop positions deviated such the measured lines differed from the actual transect length.

Aligned and regularly spaced multi-coil ECa values were obtained by the following steps. Firstly, the non-moving positions were discarded and the DUEM data positions were newly linear interpolated, since the sled was pulled straight along the transect line while the movements of the GPS carrier deviated. In the next steps, all data were interpolated to the 25 cm distances, outliers were removed using the histogram-filter, and a smoothing was applied. To this end, displaced peaks in the ECa curves of the 24 coil configurations were adjusted using the `findpeaks` function of `MATLAB` that aligned the equidistant ECa values.

### 5.3.3 Post-calibration and validation data

In campaign I, colocated EMI and ERT measurements were performed and processed as described in the post-calibration part Chapter 3, to obtain quantitative multi-coil ECa values that enable large-scale quasi-3D inversion. The inverted data were mainly the basis of campaign II but were also used to approach a 3D field capacity model as shown in the Appendix B.4, where soil texture was upscaled based on the inverted electrical conductivities and a pedo-transfer function was used to calculate the lateral and vertical field capacity due to predicted changes in soil texture. The soil sampling was based on the ECa maps (see Figure 5.4e), where soil probes were extracted by an Auger to a maximum depth of 1 m. The layers in the Auger probes were visually identified and the sand, silt, and clay contents of each horizon were analyzed in an external laboratory.

**Colocated VES and EMI data:** To post-calibrate the ECa values recorded during campaign II, colocated EMI and vertical electrical sounding (VES) measurements were performed. Three suitable calibration locations (CL) that showed relatively low, intermediate and high electrical conductivity changes in the ECa maps of campaign I

(see Figure 5.4f) were selected. At each CL, the EMI sleds and the electrode arrays were E-W and N-S directed to measure parallel and perpendicular to the paleo-river channels.

The VES data were acquired using the Schlumberger array starting with 0.1 m spacing between each of the four electrodes. The distances of the outer electrodes (AB) were increased around the common midpoint in 0.1 m steps until  $AB = 1.2$  m to resolve the very shallow subsurface electrical properties, which is needed for the very shallow sensing EMI coil configurations; see also Figure 3.7 that compares the sensitivities of the direct current methods and EMI. Next, the AB distances were increased in 0.2, 0.4, and 0.5 m steps until  $AB = 15$  m, see Table A.1 in the Appendix, to match the depth of investigation of all EMI coil configurations.

The VES data were inverted, results shown in the Appendix A.3, and the obtained layered electrical conductivities were inserted into the exact EM-FM (Equations 2.7 to 2.9) to predict EMI-ECa. To measure EMI-ECa values, the devices recorded data for around 30 seconds at the VES midpoint of each calibration location and the mean ECa were used in the subsequent linear regressions. The regression parameters were applied to the large-scale and transect data and quantitative multi-coil ECa values were obtained.

**Colocated ERT and EMI data:** In August 2015, ERT data were acquired to have additional information regarding the calibration parameters obtained by the VES post-calibration approach. The EMI data here were continuously recorded along the calibration line using the ME-VCP, SE-HCP, and the DUEM. The data were processed using the histogram filter and regularly (every 0.5 m) spaced. Next, linear regressions between the resampled and predicted ECa were performed and the obtained regression parameters were compared to the VES-based calibration parameters, see Table A.2 in the Appendix.

**Ground truth data:** Based on the campaign I results, three boreholes (BH) were drilled at each of the two transects T1 and T2 to validate the n-layer EMI inversion results and to capture the paleo-river channel dimensions. Two of the boreholes at T1

were located at the expected marginal area of the E-W directed paleo-river channel and the third BH at its expected deepest depth (see Figure 5.4f). At T2, two boreholes were drilled in the two branches of the N-S directed paleo-river channel and one BH in the expected gravelly part between the observed meander. The depths of the soil horizons were measured and a textural analysis was carried out according to DIN ISO 11277 [2002] to compare the sand, silt, and clay contents with the inverted electrical conductivities.

## 5.4 Large-Scale Data Inversion Results

The re-gridded and quantitative large-scale ECa maps of the six ME coil configurations (s32, s71, and s118 in VCP and HCP mode) used in campaign I are presented in Figure 5.4. The VCPs32 and VCPs71 coils showed ECa values of around 8 mS/m over most parts of the field, whereas the VCPs118 as well as the HCP coils showed generally low ECa values of around 5 mS/m, except for two prominent structures with apparent electrical conductivities up to 15 mS/m. One structure run approximately N-S through the middle of the field that also showed a relatively small branch directed toward the East. The second prominent structure was running westward that seemed connected to the N-S structure in the northern part of the field. These main patterns as well as an additional patch in the south-western corner were identified as paleo-river channels [Rudolph et al., 2015] belonging to a larger paleo-river system in that area.

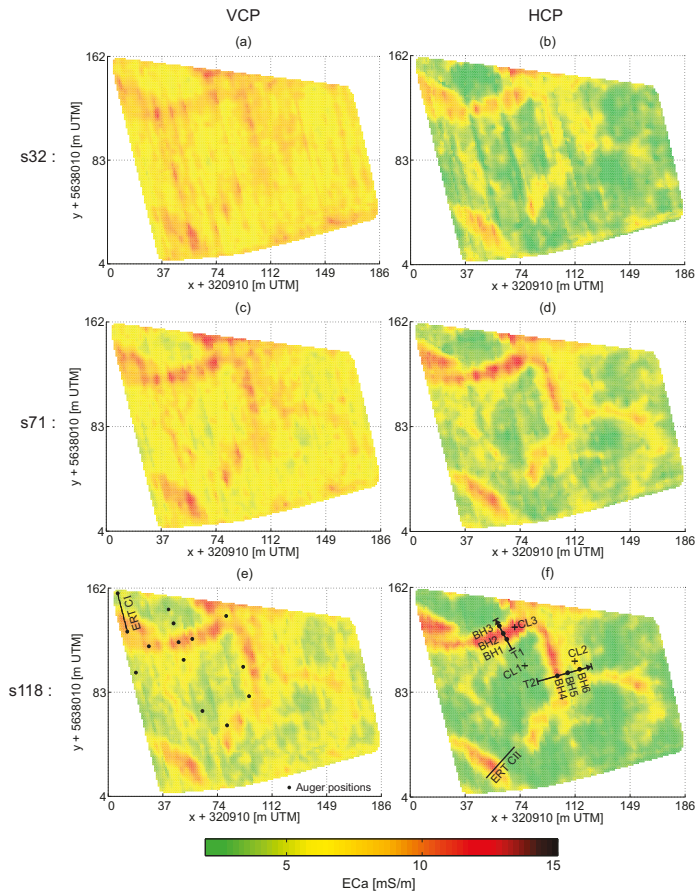


Figure 5.4: Quantitative ECa maps measured with the ME in campaign I for VCP (left) and HCP (right) column with increasing  $s$  from top to bottom. (e) Shows additionally the Auger positions and the ERT line of campaign I and (f) shows the VES post-calibration locations (CL1 to CL3) and the ERT line, the traverses T1 and T2 for detailed inversions and the validation boreholes (BH) drilled in campaign II.

The quantitative EMI data of the approximately 2.55 ha large test site were inverted for three-layers, which obtained a quasi-3D subsurface electrical conductivity model that can be used for ground characterizations. Figure 5.5a presents an upper and two lower slices through that volume, which basically shows that the upper part was relatively homogeneous and no paleo-river channels were present close to the surface opposed to the ECa map of the very shallow sensing VCPs32 coil configuration that showed the paleo-river channel structures, Figure 5.4a. This indicates that the EMI signal is more influenced by material of deeper depths than expected by the cumulative

response definition that states that 70% of the signal originate in the DOI, i.e., the upper 25 cm (0.75-s) for the VCPs32 coil configuration.

Using the inversion results instead of the apparent electrical conductivity for vadose zone characterizations directly improves studies that rely on subsurface parameters. For example, a completely new insight was obtained when comparing the correlation between the ECa of VCPs32 and LAI with the correlation between  $\sigma_1$  and LAI at the Auger positions, where the leaf area index values were derived from satellite images taken after a drought period by Rudolph et al. [2015]. Whereas LAI-ECa obtained a coefficient of determination ( $R^2$ ) of 0.63, the  $R^2$  of LAI- $\sigma_1$  was 0.15 indicating that the ploughing layer only played a minor role in the plant performance such that e.g., a crop/root modeler should consider using inverted electrical conductivities instead of ECa.

A cut through the 3D volume is presented in Figure 5.5b. Roughly, the inverted lateral and vertical  $\sigma$  values clearly reflected the sand and gravel dominated UT sediments by relatively low electrical conductivities (around 5 mS/m) and the finer textured paleo-river channel fillings by  $\sigma$  values of up to 25 mS/m.

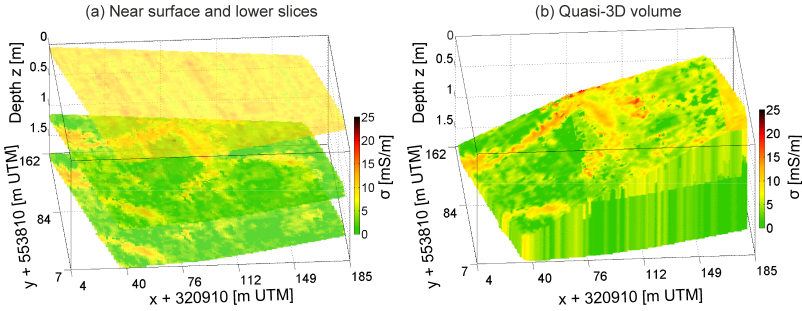


Figure 5.5: Three-layer inversion results of CMD-MiniExplorer data acquired at campaign I, where (a) shows upper and lower slice and (b) the complete 3D volume.

To detail the obtained inversion results, Figure 5.6a shows a horizontal and vertical slice within the 3D volume. The horizontal slice, inserted at 1 m depth, nicely intersects the main paleo-river channel depth that was found by the ERT-reference line presented in Figure 5.6b. The ERT-reference line started in the UT sediments (5 to 12 m transect length), passed a transition zone between 12 and 18 m, and ended above the E-W directed paleo-river channel between 18 and 25 m. Whereas the UT part and the

transition zone showed a two to three layered earth, the paleo-river channel part could be better described by four/five layers within the resolved upper 2 m depth.

For comparison, Figure 5.6c shows the three-layer ME data inversion result that found the main structures, however differences to the ERT-reference were present. Both, the ERT and the EMI-inversion similarly reconstructed low electrical conductivities at the UT part, a transition zone, and a relatively high electrical conductive upper ploughing layer. Above the paleo-river channel (meter 18 to 25), the ERT-reference showed an intermediate electrical conductive (8 mS/m) middle layer of approximately 30 cm thickness, whereas the EMI-inversion reconstructed here a 10 cm thick layer with 5 mS/m, which resulted in a mismatch of the upper interface depth of the paleo-river channel.

In a three-layer inversion, the lowest zone extends to infinity and the cumulative depth of the upper two layers reconstructed by the EMI-inversion was approximately 0.25 m such that the upper paleo-river channel interface deviated from the ERT-reference. Moreover, the lower boundary of the paleo-river channel observed at approximately 1.8 m depth in the ERT-reference can not be reconstructed by the used three-layer EMI-inversion. On the other hand, the ME could also not detect this layer boundary (maximum DOI  $\approx 1.8$  m, see ME-HCP configuration in Figure 5.3) such that more coil configurations are needed to capture the paleo-river channel depths and to enable an n-layer inversion.

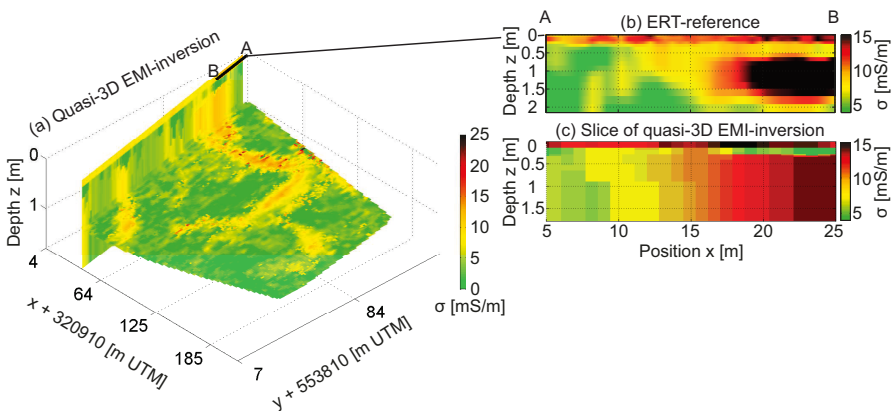


Figure 5.6: (a) The horizontal slice intersects the paleo-river channels at 1 m depth and the vertical slice represents an elongated ERT transect shown in (b). For comparison, (c) shows the extracted quasi-3D EMI inversion results at the ERT measurement positions.

In campaign II, the ME and the SE were used to record ECa values up to approximately 2.7 m depth. The quantitative data were interpolated to the campaign I grid (the ECa maps are shown in the Appendix Figure B.5), and jointly inverted. Figure 5.7 compares the campaign I and campaign II inversion results along the paleo-river channels. Note the different z-axis scale of 1.8 and 2.7 m in Figures 5.7a and 5.7b for the ME and for the joint ME & SE inversions, respectively. A movie for both campaigns showing horizontal depth slices progressing from top to bottom through the obtained 3D volume is included in the thesis.

The results indicate that the deeper sensing SE coil configurations detected the lower paleo-river channel boundaries that were imaged at around 2 m depth as similarly seen by the smooth inverted ERT-reference (Figure 5.6b). However, the two distinct upper layers (ploughing and middle layer above the paleo-river channel) that were found in the ME data inversions shown in Figure 5.7a were reconstructed here as one thicker layer.

The reasons lie in the soil states due to the weather conditions, where lower temperatures and relatively high rain fall rates were observed before campaign I and higher temperatures and no rain a few days before campaign II (see Figure B.2 in the Appendix for more detail). Technically, the ME is well suited to sense relatively shallow layer boundaries (compare Figure 5.3), which allowed to set the layer thicknesses in the SCE code of Section 2.2.1 to 0.35 m for the first and 0.76 m for the second layer. This differentiated the upper 1 m depth, where a wet ploughing layer and a probably drier intermediate layer above the paleo-river channel were present and the channel was described by the lowest zone in that three-layer inversion.

To invert the large-scale data of campaign II, the parameter space with respect to the layer boundary depths could be increased due to the deeper sensing SE coils, which resulted in a good reconstruction of the main subsurface contrasts. The upper subsurface was relatively dry (due to low precipitations and high temperatures) such that the previously distinct layers were reconstructed as one thicker layer with low electrical conductivities. The second layer, i.e., the paleo-river channel, was comparatively wet due the finer material that also showed a higher field capacity (Appendix B.4) and the lowest zone was gravelly. Therefore, the material property changes were reflected by

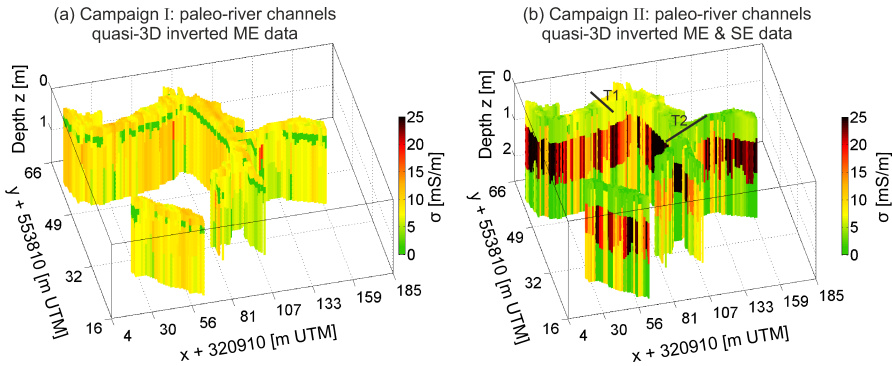


Figure 5.7: Extracted paleo-river channels of three-layer SCE inversion for (a) quantitative ME and (b) jointly inverted quantitative ME and SE data and the two transects for the detailed analysis plotted on top.

the SCE inversion by a change of low-high-low  $\sigma$  for  $h_{1,2}$  and the lowest zone.

However, the inverted upper and lower paleo-river channel interfaces appeared very straight, which indicates that the inversions converged to the maximum layer thicknesses such that more layers are needed to describe the subsurface as already indicated by the previous ERT-reference (Figure 5.6b). To assure stable inversion for more distinct layers, the proposed inversion scheme that incorporates no smoothing and damping parameters to obtain sharp layer boundaries need an overdetermined system and therefore more available data (coil configurations) than parameters.

## 5.5 Detailed transect inversions

To enhance imaging capabilities, all 24 EMI coil configurations were used to measure two transects (T1 and T2) perpendicular to the E-W and to the N-S directed paleo-river channels, see Figure 5.7b. The processed and post-calibrated ECa values were inverted for 2, 3, 4, and 5 layers and the performance was evaluated by the corresponding misfits. Moreover, the obtained results were validated by extracted soil cores and compared to the soil textural information.

**Transect T1**

Transect T1 run over the E-W directed paleo-river channel crossing its expected deepest depth. The actual measurement line was 25 meter long that shortened to around 15 m (2.5 to 17.5 m) due to the sled positions and GPS precision. Figure 5.8a shows the obtained ECa values of the 24 coil configurations. Whereas the deepest sensing DUEM-HCPs400 showed the lowest ECa values of around 8 mS/m over the whole transect length, the DUEM-HCPs200 obtained the largest data ranging from 12 mS/m in the beginning over 20 mS/m approximately in the middle to 10 mS/m at the end of the transect. The other coil configurations obtained ECa values in-between.

Inverting these data for two layers resulted roughly in two homogeneous blocks, see Figure 5.8b, that do not describe the observed subsurface structures as shown by the previous EMI and ERT inversions and as reflected by the relatively large misfits displayed in Figure 5.8e. The three-layer inversion result is presented in Figure 5.8c. Comparing the results with the joint ME-VCP & SE-HCP 3-layer inversions that showed straight interfaces, the inversion of all 24 coils resolved a more naturally shape of the paleo-river channel (slightly curved instead of straight) until transect meter 11. From 11 m toward the end, the channel dives into deeper depths as can be seen in the four- and five-layer inversions in Figure 5.8d and Figure 5.8e, respectively, such the inversion was not able to reconstruct this part but converged to the maximum allowed layer thickness set in the SCE code.

Both, the four- and five-layer inversions were visually almost identical in the first 13 m, which was reflected in the overlying misfit curves. Between 13 and 15 m the channel seems weakly inclined dipping downwards that was reconstructed by the four-layer inversion with an abrupt change and a relatively straight interface toward the end at 17.5 m. Such a dipping event is more difficult to reconstruct as reflected by the largest misfits in that part. This was also noted previously, where the misfit curves raised above dipping events and/or relatively large differences to ERT-reference models were observed, see Figure 4.4 and Figure 3.8. The larger differences at dipping events are attributed to the forward model that assumes a horizontally layered earth such that a future task should consider a 2D or 3D forward model to reconstruct these events.

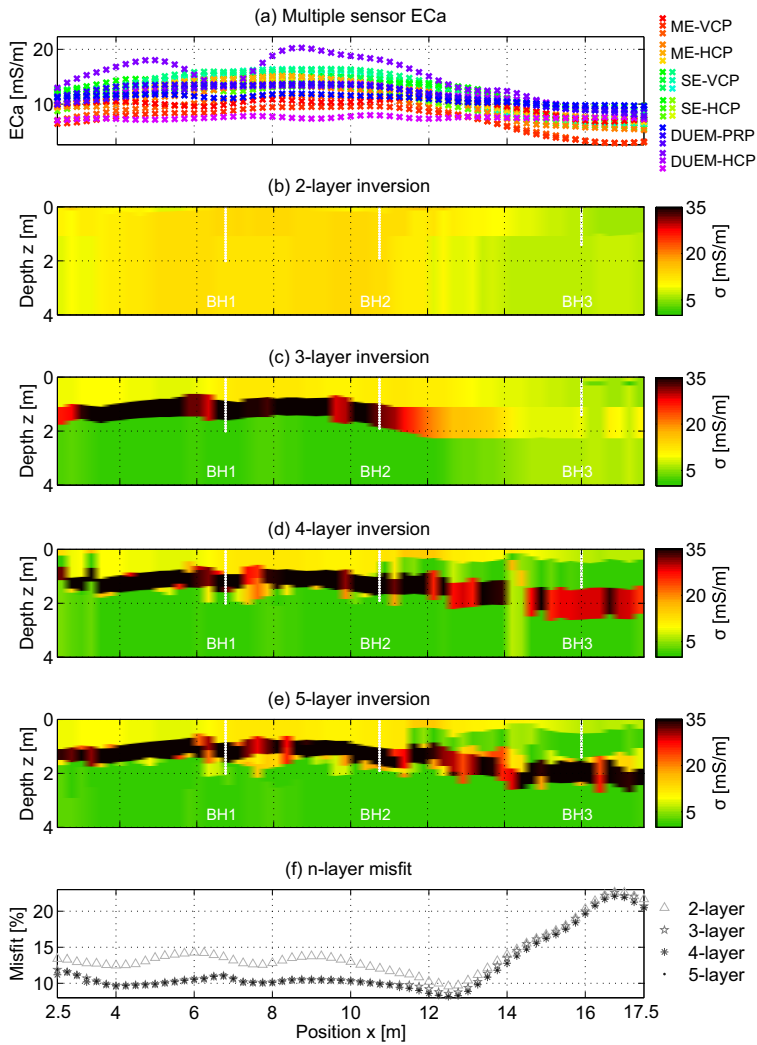


Figure 5.8: Multiple EMI device data and the boreholes of transect T1, see Figure 5.4f. Here, (a) shows the post-calibrated ECa values that were inverted for (b) 2-layer, (c) 3-layer, (d) 4-layer, and (e) 5-layer. (f) Shows the corresponding misfits at each position.

To validate the inversion results, boreholes of up to approximately 2 m depth were drilled and the cores were partitioned for textural analysis. A 1:1 comparison of the four- and the five-layer inversion results with the soil texture determined for each horizon of the extracted soil columns is presented in the Appendix Figures B.7 and B.8. The upper panel of Figure 5.9 compares the inverted layer boundaries of the four-

and five-layer inversion with the real paleo-river channel interfaces that were measured along the extracted soil cores using a tape. The lower panel displays the soil cores and shows details of the main soil material.

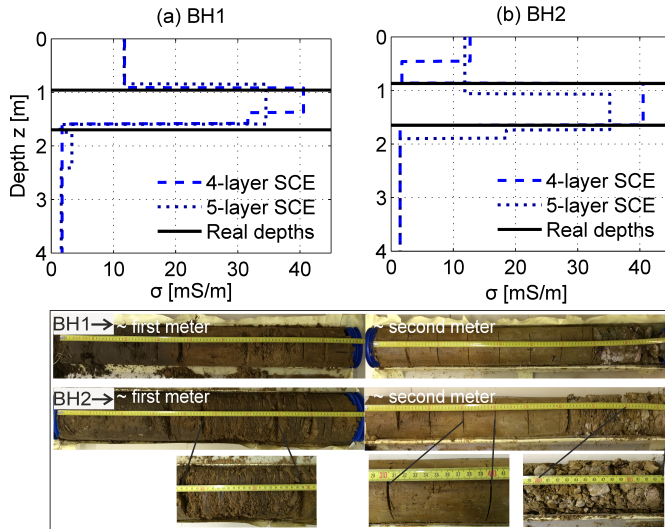


Figure 5.9: Comparison of four/five-layer inversion result compared to the soil cores drilled at transect T1.

Both, the four- and five-layer inversions matched the measured paleo-river channel depths indicating a well performance and therefore the applicability of the proposed method, i.e., sophisticated forward modeling and inversions incorporating the  $L_1$ -norm without smoothing and damping to assure sharp layer boundaries, to resolve the complex subsurface where the soil abruptly changes with depth, see soil core photos in the lower panel of Figure 5.9.

**Transect T2**

Transect T2 crossed the N-S directed paleo-river channel, passed a probably gravelly zone and included the eastward directed branch of the channel structure (compare Figure 5.4f). The actual length was 39 m that shortened to 35 m (0.5 to 35.5 m transect length) due to processing. Figure 5.10a shows the apparent electrical conductivities of the 24 coil configurations. The smallest ECa values were around 5 mS/m obtained by the ME-VCP and the largest values were up to 15 mS/m for the DUEM-HCPs200. The ECa curves generally increased in the beginning with a peak at around 12.5 m, then decreasing until 25 m, and then increasing, peaking and falling again in the last 10.5 m.

Similar to the previous transect, the data were inverted for 2- 3- 4- and 5-layers displayed in Figure 5.10b, 5.10c, 5.10d, 5.10e, respectively, and the corresponding misfits are shown in Figure 5.10f. Increasing the layers increased the subsurface differentiation, where the four- and five-layer inversions seem to image the most details.

The boreholes were located at the main N-S directed paleo-river channel (BH4), at the eastwards directed branch (BH6), and in-between channel and branch (BH5), where the ME data of campaign I suspected a gravelly zone. Contrary, the subsurface model obtained by jointly inverting the ME, SE, and DUEM data of campaign II indicate that the paleo-river channel was present below BH5. The extracted soil core of BH5 only showed coarse material within the drilled 1.2 m, which confirmed the expectation of no paleo-river channel during the field work such that the drilling stopped. Since the joint inversion results revealed the presence of the channel deeper than the drilling depth, a future campaign will drill deeper for validation.

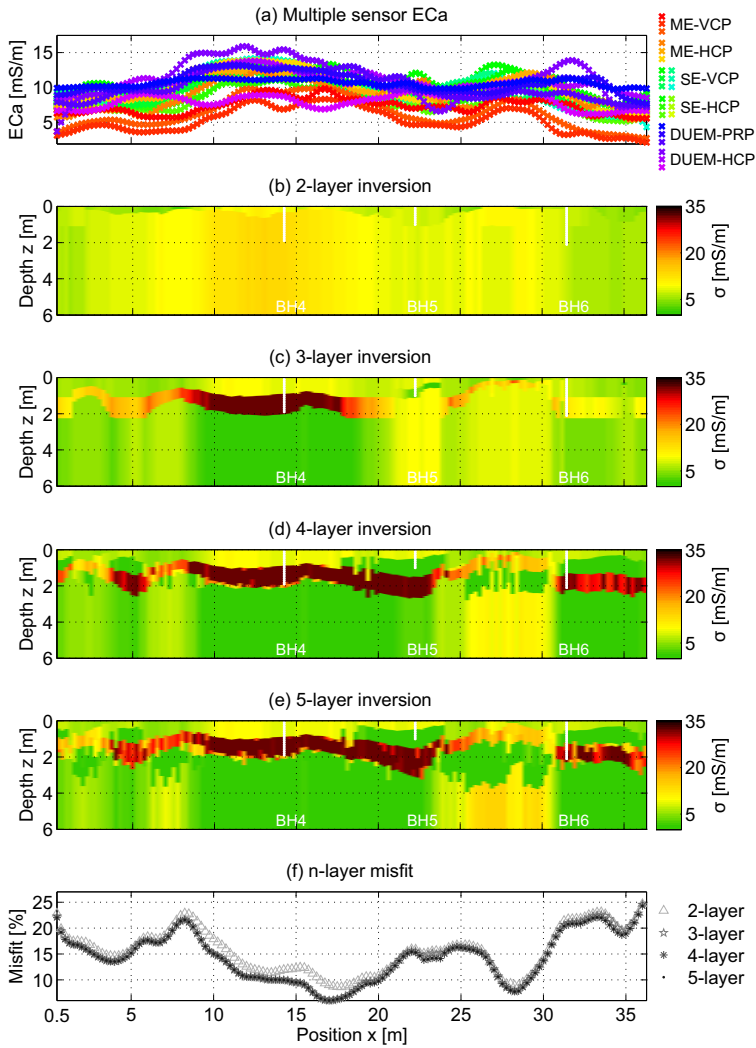


Figure 5.10: Multiple EMI device data and the boreholes of transect T2, see Figure 5.4f. Here, (a) shows the post-calibrated ECa that were inverted for (b) 2-layer, (c) 3-layer, (d) 4-layer, and (e) 5-layer. (e) Shows the corresponding misfits at each position.

The comparison of the inverted and real layers depths of the boreholes BH4 and BH6 (located above the paleo-river channels) is shown in Figure 5.11 in the upper panel and the lower panel shows the photos of the respective soil cores. The 4- and 5-layer inversions reconstructed the paleo-river channel interfaces although the material within the N-S directed channel differed to the previous observations.

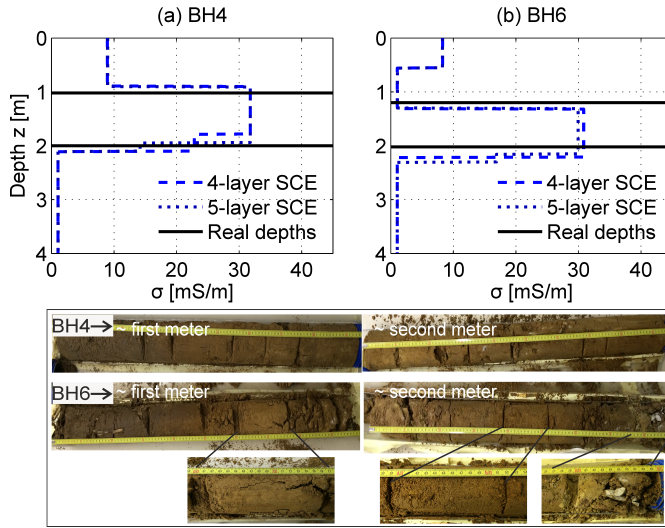


Figure 5.11: Comparison of four/five-layer inversion result compared to the soil cores drilled at transect T2.

The 1:1 comparison of the 4- and 5-layer inversion results with the extracted soil columns is presented in the Appendix Figures B.7 and B.8. These show that mainly the sand contents increase within the N-S directed paleo-river channel, while clay stays relatively stable and the inverted electrical conductivities were nevertheless relatively high. Since the E-W directed paleo-river channel material showed decreasing sand and increasing clay contents, the texture analysis interpreted together with the inversion results indicate that the soil composition differed between the channels but furthermore that different clay types were present. This indicates that the paleo-river channels formed at different times and/or that the channels were not directly connected. In future work, a luminescence dating (accuracy  $\pm 1000$  a) or even an analysis of pollen will be conducted to determine the age and/or the formation of these channels.

## 5.6 Conclusions

The paleo-river channels showed a relatively fine textured soil that has a higher field capacity than the surrounding gravelly material thus supplying water to the plants especially under drought conditions. To evaluate the impact of such a complex subsurface system on plant performance and yield, exact imaging tools are the key to improve

hydrological as well as root models.

To improve the imaging, multiple EMI device data were used together with sophisticated forward and inverse modeling strategies to quantitatively characterize the subsurface, where it was shown that the use of multi-coil devices enabled a multi-layer electrical conductivity inversion. The obtained results were validated with extracted soil cores such that the presented combination and joint inversion of quantitative multi-coil EMI data of multiple EMI devices improves vadose zone characterizations.

## Chapter 6

# Final Conclusions and Outlook

The presented topics showed novelties that were developed during the doctoral studies but of course studying and re-thinking never stops. On the next pages, the main objectives are summarized, conclusions are drawn, and the outcomes are discussed. Finally, an outlook to future work is presented.

### 6.1 Conclusions and Discussions

#### **Post-calibration**

Since external influences shift the recorded ECa values up to factor of 2, as observed when comparing the EMI data measured along the same transect using different field setups, the static shifts must be compensated by post-calibrating the EMI-ECa values. A calibration line that ideally covers the measured ECa range of the entire field can be obtained by pre-investigating the test site using large-scale EMI measurements. The calibration parameters obtained at that line calibrate in turn the large-scale ECa values such that these can be quantitatively inverted.

When merging several well-performing ( $R^2 > 0.75$ ) calibration lines of different test sites and dates, universal calibration parameters were returned that can consequently reduce/spare the extra ERT field work to obtain quantitative ECa data. Note that it is here very important to use the same EMI field operation e.g., the same device with the same field setup including the sled, the handheld, GPS, and cables as well as similar data processing.

The equipment was extended with new EMI devices and newly constructed sleds

such that the derived universal calibration parameters were not applicable to newly acquired data meaning that new calibration lines needed to be recorded. However, ERT measurements are time consuming (relative to EMI measurements) and matching the ECa range of the entire test site with only one calibration line was not always successful. Moreover, the ERT setup strategy was adapted to the CMD-MiniExplorer. The Dipole-Dipole electrode array with 0.25 m spacing in combination with the Robust inversion scheme of RES2DINV was chosen to have a as high near surface sensitivity as possible with ERT and to obtain piecewise constant regions within the ME DOI's. The newly purchased EMI devices increased the DOI's up to 6 m. To match the very shallow to deep resolutions with ERT, at least one small and one larger electrode offset ERT measurement and possibly different ERT inversion schemes would have been needed for successful multiple EMI device calibrations.

To overcome these limitations, the more flexible vertical electrical soundings (VES) were considered. The presented results look promising however, the optimum electrode array to resolve close to surface need to be found. Ideally, very small electrode distances deliver information for the very shallow sensing EMI coils. However, the chosen 0.1 m distances produced the following error chain. Firstly, an artificial high current density was introduced between the electrodes resulting in low apparent resistivities. Inverting these 'false' data resulted in too large  $\sigma$  for the shallow layers and thus in too large predicted EMI-ECa values for the shallow sensing coil configurations such that these were not useful for calibration. For the deeper sensing coil configurations, this error was compensated by the natural data of the deeper VES measurements such that the approach conclusively shows a large potential to replace the ERT-based post-calibration.

### **Inversions**

By inverting post-calibrated multi-coil EMI data including the EEC approach, high quality quantitative images of the subsurface were obtained that reflected the lateral and vertical electrical conductivity changes with the main benefit that EMI measurements can be carried out quickly due to their inductive coupling with the ground such that large-scale studies are possible. Depending on the subsurface complexity and the depth of investigation of the EMI devices, the subsurface was described with up to five-layers.

The large-scale EMI data acquired at two different test sites (ME at a 1.1 ha bare-soil field and ME as well as joint ME-VCP & SE-HCP at a 2.55 ha field characterized by paleo-river channels), allowed to invert for three-layers because the proposed inversion scheme requires more data than medium parameters for stable inversion since no smoothing and damping parameters are considered to assure sharp layer boundaries. The quasi-3D EMI-inversions revealed patterns related to the observed variations in soil texture and soil water content. At the bare-soil field, the differences in the  $\sigma(z_i)$  between the EMI-inversions and the independent ERT transects were attributed to different soil states between the different years and at the paleo-river channel field, the EMI-inversions reflected dry and wet soil states between campaign I and campaign II.

However, the inversions of the ME data obtained in campaign I were only able to reliably resolve the upper 1 m depth due the main sensitivity of the ME coil configurations in the upper meter. The joint inversion of ME & SE data acquired during campaign II reconstructed the main material changes with a deeper resolution compared to campaign I but the inversions converged to parameter space boundaries such that the obtained results do possibly not reflect the real layer boundaries. A better reconstruction may be obtained by increasing the search space, however, the space was set according to the data, where the layer thicknesses were determined by the imaging capabilities of the EMI devices reflected by the coil specific DOI's.

An improved depth resolution was obtained by the extension of the coil configurations due to new EMI devices. The 24 coil configurations enlarged the depth of investigation as well as the resolution of certain depth intervals due to the similar DOI's among some of the coil configurations of the three EMI devices. Because of both higher resolution and deeper depth information, the layers in the inversions could be increased.

Of course, increased number of parameters increased the inversion time. To invert for example the 15 m long transect T1, the 27 processors of the IBG-3 computer cluster took around 9 minutes for the two-layer inversion and around 1, 2, and 4 hours for the three-, four-, and five-layer inversions, respectively. The two-layer inversion was not able to reconstruct the subsurface. The three-layer inversion better resolved the paleo-river channel shape compared to the reduced large-scale setup, except for the part where the channel dipped downwards. This dipping event was better reconstructed by

the four- and five-layer inversions, which even resolved small-scale soil textural changes as well as the upper and lower interfaces of the paleo-river channel such that future measurements use more coil configurations when covering/inverting the full area.

### **Findings and usage of the inversion results**

The obtained results were compared to soil texture and can be furthermore correlated with other soil properties such as clay content, mineralization, and soil water content. Here it was shown, that the inverted electrical conductivities contain more information of the soil properties than the measured ECa value. The  $R^2(\text{LAI-ECa}^{\text{VCPs32}})$  was 0.63, which allows to conclude that the upper subsurface contributes to plant performance, remember the DOI of VCPs32 is approximated similar deep as the ploughing layer. On the other hand, the  $R^2(\text{LAI-}\sigma_1)$  was 0.15 showing that the upper soil layer plays a minor role (under drought conditions). Therefore, interpreting ECa values in terms of depth should be carefully done and models that rely on subsurface parameters such as plant/root models should rather use EMI-inversion results instead of ECa values.

These findings encouraged to upscale the soil textural changes based on the inverted electrical conductivities to obtain a 3D field capacity (FC) model. The Auger probes were mainly taken at or close to the paleo-river channels, which resulted in an agreement of the predicted FC with literature values. However, the main part of the field is sand and gravel dominated that were not reflected by the obtained FC such these results need improvement, e.g., by taking more soil probes over the entire area. Moreover, a residual (error) analysis may be performed to better grasp the details and handle the results.

Uncertainty analysis is an emerging research field. Since the presented results were obtained using a deterministic inversion approach, a first attempt to perform uncertainty analysis was initiated by implementing the probabilistic DREAM algorithm. However, the outcome of DREAM strongly depends on the measurement error input. To determine the error here, each EMI device was positioned E-W and N-S at three different locations at the paleo-river channel field and recorded data for around 30 seconds. The coil specific standard deviation of each of the six measurements were averaged and passed to DREAM. The obtained inversion results differed from the real paleo-river channel depths such that more research is needed to handle the required

input for DREAM such that an uncertainty analysis becomes feasible.

### **Measurements and field setup**

Since field work is always exciting and never the same, the EMI equipment was standardized to assure as comparable measurements as possible. For example, each EMI device always use the same handheld, GPS, and even the same data cables that are attached to the respective EMI sled at the same positions that are always towed with the same distance to the ATV and the sleds are in the same order.

Nevertheless, the field setup is still open for improvements. One issue is the used single-frequency GPS that provides low accuracy and precision. To resolve large-scale structures the GPS is sufficient. However, when for example repeated long-term measurements are performed, the possible deviations in the meter scale may impact the outcome and will certainly complicate interpretations such that a differential GPS may be considered for future measurements.

## 6.2 Outlook

The conducted doctoral studies were part of Cluster B6 that reside in the interdisciplinary project TR32 (Transregional Collaborative Research Centre 32) funded by the Deutsche Forschungsgemeinschaft (DFG). The focuses lie on the role of patterns in the terrestrial systems.

Recently, the third phase of TR32 started, where B6 aim to improve hydrological models by geophysical data. Therefore, the next steps start by investigating an increased area of approximately the size shown in Figure 6.1, where the satellite image nicely shows the paleo-river channel patterns. The impact of these structures on the subsurface hydrology will be investigated by repeated EMI measurements and inversions. Analyzing the electrical conductivity changes over time allows to separate the stable soil properties from the dynamics attributed to the soil water content changes. Moreover, GPR measurements will be included to capture the structural organization of the soil (layer depths, soil texture) and the associated soil hydraulic properties of the large paleo-river system.



Figure 6.1: Focus area around the investigated bare-soil and paleo-river channel field to characterize the impact of the paleo-river channels.

## Appendix A

EMI post-calibration based on  
inverted vertical electrical  
sounding (VES) data

## A.1 VES Data Acquisition

This chapter introduces a novel calibration approach based on inverted vertical electrical sounding (VES) data. VES measurements use four electrodes (two current supplying electrodes AB and two, MN, that measure the potential) to obtain the vertical electrical conductivities at a specific location while several soundings distributed over the test site provide additional lateral information [Knödel, 2007].

During the docotoral studies, the EMI equipment was extended such that the depth of investigation increased up to 6 m. To match the DOI's of the very shallow and the deep sensing coils, the AB electrodes were stepwise increased from 0.1 to 15 m (see Table A.1), where the depth of investigation of direct current methods is approximately  $AB/2$  [van Nostrand, 1984]. The data were recorded at suitable calibration locations (CL). Similar to the ERT based post-calibration, the VES spots are choosen where the large-scale ECa maps show relatively low, intermediate and high ECa values. To record VES data at these locations, the Lippmann 4 point light hp earth resistivity meter (Lippmann Geophysikalische Messgeräte, Schauffing, Germany) is used.

Table A.1: Vertical electrical sounding electrode distances of the Schlumberger array used to resolve the very shallow subsurface (needed for VCPs32) and to match the deeper DOI's (up to  $\approx 6$  m).

AB/2 [m]	0.2	0.3	0.4	0.5	0.6	0.8	1.0	1.2	1.6	2.0	2.4	3.2	4.5	7.5
MN/2 [m]	0.1	0.1	0.1	0.1	0.2	0.2	0.2	0.4	0.4	0.4	0.8	0.8	1.5	1.5

At the VES midpoint, the EMI devices continuously record ECa for about 30 seconds and the mean value is used in the linear regressions between measured and predicted ECa. To predict ECa, the VES data are inverted using the following inverse-modeling scheme.

## A.2 Forward and Inverse Modeling of VES Data

To obtain the layer electrical conductivities  $\sigma(z_i)$  (reciprocal of the electrical resistivity) from the measured apparent resistivities  $\rho_a$ , the data can be modeled for homogeneous and isotropic layers according to Koefoed [1970] as

$$\rho_a = s^2 \int_0^\infty T(\lambda) J_1(\lambda s) \lambda d\lambda, \quad (\text{A.1})$$

with

$$T_n(\lambda) = \frac{T_{i+1}(\lambda) + \rho_i \tanh(\lambda h_i)}{[1 + T_{i+1}(\lambda) \tanh(\lambda h_i) / \rho_i]}, i = n - 1, \dots, 1. \quad (\text{A.2})$$

Here  $s = AB/2$ ,  $J_1$  denotes the first order Bessel function of the first kind,  $\lambda$  is the integration variable. The resistivity transform function  $T(\lambda)$  is obtained recursively, where  $n$  denotes the number of layers and  $\rho_i$  and  $h_i$  are the  $i$ -th electrical resistivity and the  $i$ -th layer thickness, respectively [Gupta et al., 1997; Ekinici and Demirci, 2008].

For the inversions, the  $n$ -layer SCE algorithm of chapter 2.2.1 used the classical sum of squared error likelihood function to maximize the probability of a parameter set being the global optimum.

The optimized parameter set is assumed to reflect the true electrical conductivity distribution at the particular calibration location and is inserted into the exact EM-FM, Equations 2.7 to 2.9, to obtain the magnetic field ratio that is converted into ECa using the EEC approach (Section 3.1). Next, linear regressions are performed between the measured and predicted ECa values of all calibration locations to obtain the coil specific calibration parameters that can be applied to the large-scale EMI data to obtain the quantitative ECa values.

### A.3 Multiple EMI Device Data Post-Calibration Based on Inverted VES data

The present section uses the data obtained at the paleo-river channel field in July 2015, Chapter 5. The VES electrode array and the EMI sleds were directed East-West (E-W) and North-South (N-S) at three calibration locations (CL) to measure inline and crossline data with respect to the paleo-river channels. The EMI data were recorded using the CMD-MiniExplorer (ME), the CMD-SpecialEdition (SE), and the DualEM-421 (DUEM) and the VES data were acquired as shown in Table A.1. Figure A.1 shows the measured and inverted VES data.

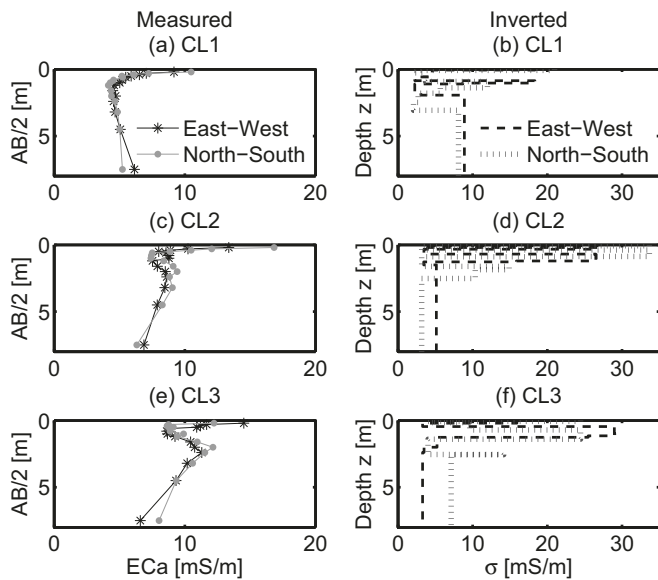


Figure A.1: VES data inversion results of the three calibration locations, where the data were recorded in east-west and in north-south direction.

The measured data of the E-W and N-S directions showed almost overlying curves indicating a relatively high repeatability. CL1 was located at the gravelly terrace, CL2 was located close to a North-South directed paleo-river channel and CL3 was located above an East-West directed channel. Note the relatively high apparent electrical conductivities recorded for the first three measurements ( $AB/2 = 0.1, 0.2, 0.3$  m) that may be artificial due to a very high current density introduced by small electrode

distances [Igel, 2007]. This resulted in the inversions in relatively high  $\sigma$  values for the upper layers and therefore in relatively high predicted ECa for the shallow sensing EMI coil configurations, see Figure A.2.

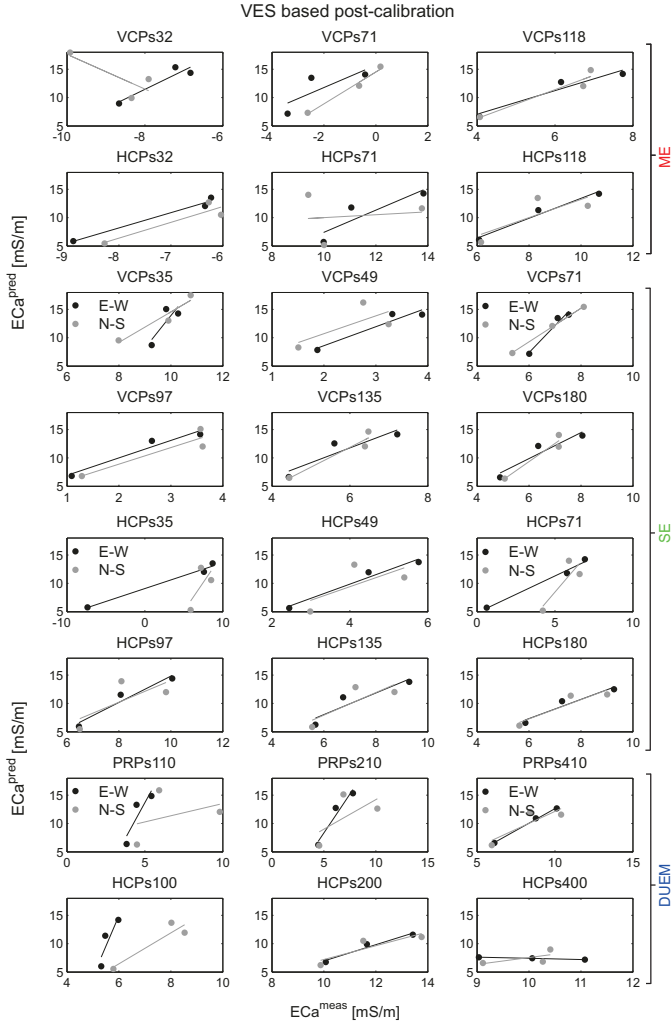


Figure A.2: The inverted VES data were inserted in to the EM-FM to predict multi-coil ECa values for the ME, the SE and the DUEM device for east-west (E-W) and north-south (N-S) directed measurements.

The linear regression parameters between measured and predicted EMI-ECa corresponding to Figure A.2 are presented in Table A.2 that also shows the regression parameters of the colocated ERT and EMI measurements performed in August 2015,

where EMI data were recorded only for ME-VCP, SE-HCP, and the DUEM.

Table A.2: Linear regression parameters scale, shift (a, b), and the  $R^2$  of VES based post-calibration of ME, SE and DUEM data related to Figure A.2 as well as the parameters of the ERT based post-calibration. Note that colocated EMI and VES were recorded in July 2015 whereas EMI and ERT data were recorded in late August 2015. The regression parameters used to post-calibrate the EMI data are colored.

	a, b, $R^2$	a, b, $R^2$	a, b, $R^2$	a, b, $R^2$	a, b, $R^2$	a, b, $R^2$
	ME-VCP			ME-HCP		
	s32	s71	s118	s32	s71	s118
E-W	3.3, 38, 0.89	2.0, 16, 0.62	2.0, -1, 0.93	<b>2.7, 30</b> , 0.98	<b>2.0, -12</b> , 0.78	<b>1.8, -4</b> , 0.97
N-S	3.1, -13, 0.65	2.8, 15, 0.98	2.5, -4, 0.92	2.8, 29, 0.85	0.3, 7, 0.02	1.6, -2.8, 0.63
ERT	<b>1.7, 22</b> , 0.81	<b>2.2, 8</b> , 0.76	<b>2.3, -7</b> , 0.92			
	SE-VCP					
	s35	s49	s71	s97	s135	s180
E-W	5.7, -43, 0.70	<b>3.4, 2</b> , 0.92	4.8, -21, 0.96	3.1, 4, 0.95	2.6, -4, 0.84	2.3, -4, 0.90
N-S	<b>2.7, -12</b> , 0.92	3.2, 4, 0.51	<b>3.0, -9</b> , 0.99	<b>2.9, 3</b> , 0.86	<b>3.5, -9</b> , 0.92	<b>3.2, -10</b> , 0.93
	SE-HCP					
	s35	s49	s71	s97	s135	s180
E-W	0.5, 9, 0.99	2.5, -0.1, 0.97	1.3, 5, 0.99	<b>2.3, -8.4</b> , 0.94	<b>1.9, -3</b> , 0.86	<b>1.7, -3</b> , 0.93
N-S	2.0, -5, 0.48	2.4, -0.1, 0.46	3.2, -8, 0.73	1.9, -5, 0.52	2.0, -4, 0.68	1.7, -3, 0.86
ERT	<b>2.9, -9</b> , 0.93	<b>2.6, -5</b> , 0.95	<b>2.6, -3</b> , 0.95	2.9, -16, 0.97	3.1, -12, 0.97	3.0, -11, 0.95
	DUEM-PRP			DUEM-HCP		
	s110	s210	s410	s100	s200	s400
E-W	5.0, -11, 0.80	2.7, -5, 0.94	1.5, -3, 0.99	10.66, -49, 0.79	1.4, -7, 0.96	-0.2, 10, 0.99
N-S	<b>0.7, 7</b> , 0.14	<b>1.0, 4</b> , 0.40	<b>1.3, -0.5</b> , 0.74	<b>2.7, -10</b> , 0.86	<b>1.2, -5</b> , 0.78	<b>1.2, -5</b> , 0.43
ERT	2.0, -4, 0.61	2.1, -4, 0.47	3.3, -15, 0.44	2.5 -7, 0.37	4.4 -35, 0.47	11.4, -94, 0.62

The obtained parameters were used to post-calibrate the transect and large-scale EMI data of campaign II, where the regression parameters that showed the largest  $R^2$  were selected, except for the very shallow sensing coils (overestimated ECa predictions). Here, the regression parameters of the ERT based post-calibration were selected. The colored values in Table A.2 indicate the selections. Note, the digits were rounded here due to displaying purposes but not in the actual post-calibrations. Figure A.3 shows an example of the post-calibration. The parameters were applied to the uncalibrated data shown in Figure A.3a to obtain post-calibrated multi-coil ECa values of all 24 coil configurations, see Figure A.3b.

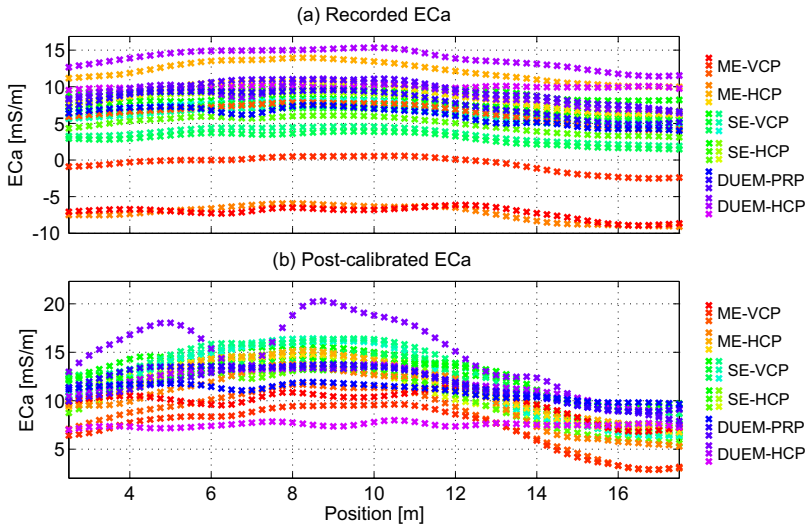


Figure A.3: Multiple EMI device data for (a) recorded and processed ECa and (b) the post-calibrated ECa.

As can be seen, the negative values of the shallow sensing ME-VCP coils were shifted positive and all multi-coil ECa values can be considered quantitative, since the inversions of these data reconstructed the soil layers with negligible deviations, compare Section 5.5. This indicates that the VES-based post-calibration approach is a suitable replacement for the ERT-based calibration with the additional benefits of more flexibility in the field, its relatively fast and easy assembling, and that VES can cover almost every depth of investigation.



## Appendix B

# Supplementary Data for Test Site Characterizations

## B.1 Bare-Soil Field Topography and Aerial Image

The bare-soil field, located in the Lower Terrace, covers around 1.1 ha with a size of 190 m in East-West (E-W) and 60 m in North-South (N-S) direction, see Figure B.1a. From East to West, the elevation drops 5 m with the steepest part (slope  $\approx 4^\circ$ ) between 100 and 150 m E-W. Figure B.1b shows the relatively short post-calibration line as well as the ERT transect positions of 2009 and 2010 that were used to validate the quasi-3D EMI inversion results.

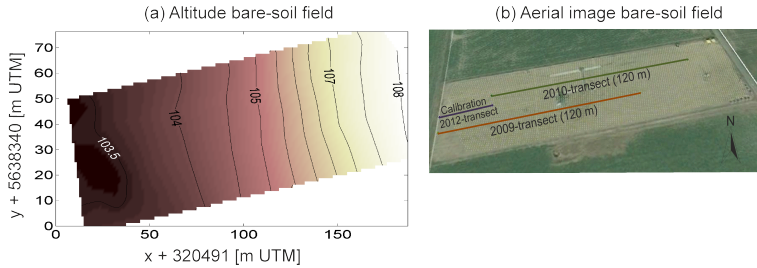


Figure B.1: (a) Topography and (b) aerial image of the bare-soil that also shows the relatively short (30 m long) post-calibration line as well as the two independent 120 m long ERT transects of 2009 and 2010 that validated the large-scale quasi-3D inversion results.

## B.2 Weather Conditions Before and During the Large-Scale Surveys

The precipitation plays an important role with respect to the ground electrical conductivity distribution and thus the recorded ECa because  $\sigma$  generally increase with increasing soil water content. Different soil states were observed at the bare-soil field, where the EMI inversion results showed similar structures but different electrical conductivities as two independent ERT transects measured two and three years before the EMI survey, Figure 4.8.

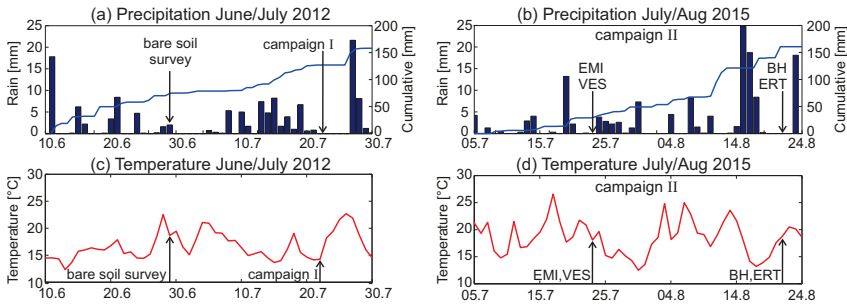


Figure B.2: Mean daily precipitations and temperatures before and during the large-scale surveys at the bare soil field of Chapter 4 as well as before/during campaign I and campaign II that were performed at the paleo-river channel field presented in Chapter 5. The data were provided by the meteorological station of Forschungszentrum Jülich approximately 5 km apart from the test sites.

At the paleo-river channel field, the different soil states were observed in the comparison between the inversion results of campaign I and campaign II, see Figure 5.7.

To relate the soil states to the precipitation, Figure B.2a and Figure B.2b show the rain fall and temperatures before and during the performed surveys that were conducted to study the subsurface electrical conductivity structures that are related to the vadose zone characteristics.

### B.3 Synthetic Study to Obtain Optimal EMI Field Setup for Paleo-River Channel and Surrounding Field Characterizations

A large-scale survey is time intensive, especially when a detailed measurement campaign is planned that includes , large-scale EMI survey, recordings along specific transects, calibration data measurements (EMI plus VES and/or ERT) as well as soil sampling including Auger or deep drilling, bulk density probes, plus TDR and/or Hyprop for soil hydrology.

Currently, three EMI devices with up to 24 coil configurations can be used for the EMI based subsurface characterizations. For this, the entire test site is surveyed twice since the ME and SE measure either in VCP or in HCP mode. Therefore, a synthetic study presented in Figure B.3 was performed to find a compromise between survey

duration and information content.

Based on the bare-soil and paleo-river channel field, five models layered earth models (Figure B.3b) were used to generate data for the three EMI devices, Figure B.3a. Model 1 and 2 represent the paleo-river channel field and the models 3 to 5 the surrounding area. The inversion were carried out the SCE code for four-layers.

The inversion result of the 24 coil configurations is displayed in Figure B.3c, showing that all models were reconstructed. When inverting the data of the reduced setup, the inversions were able to describe the data with negligible deviations for model 1. Thus, the proposed field setup (ME-VCP, SE-HCP, DUEM) delivers the required information while saving time. Of course, similar studies can be performed that optimize the field setup to resolve other subsurface conditions by combining other possible coil configurations.

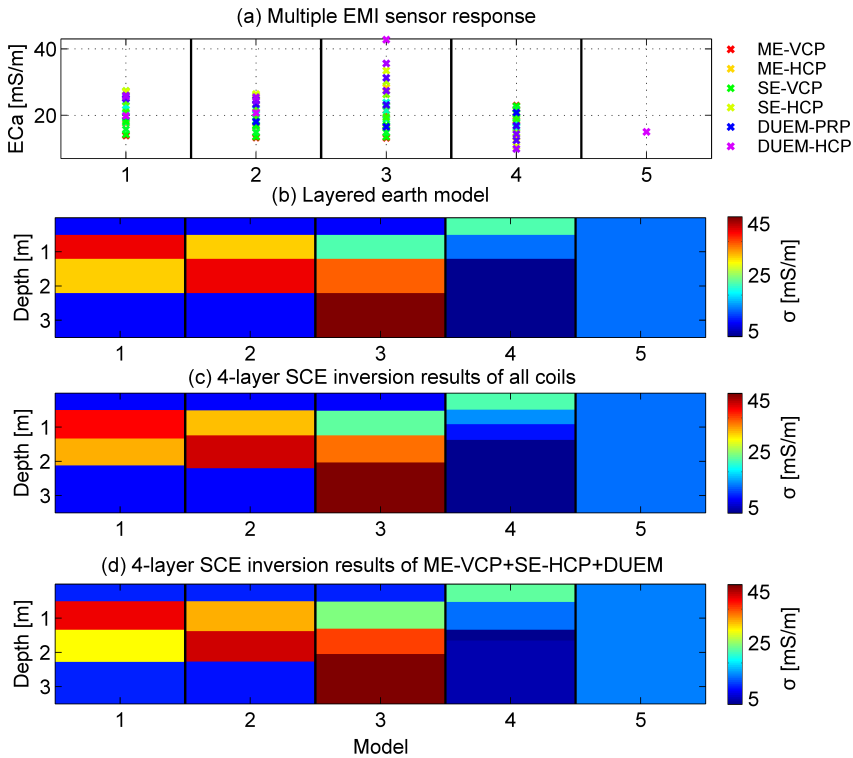


Figure B.3: Synthetic study to obtain a compromise between measurement time and large-scale information to reconstruct the expected electrical conductivity distribution at the paleo-river channel field presented in Chapter 5.

## B.4 Pedo-Transfer Functions to derive the Field Capacity

### B.4.1 Pedo-transfer model

Information of soil hydraulic parameters are often cumbersome and expensive to obtain [Vereecken et al., 1990] especially when covering large areas [Schaap et al., 2004]. These limitations have been addressed by the development of pedo-transfer functions, e.g., [Van Genuchten, 1980], that use relatively easy measurable soil textural information to estimate the soil hydraulic properties. Here, ROSETTA of Schaap et al. [2001] was used to estimate the saturated and residual water contents  $\Theta_s$  and  $\Theta_r$ , respectively, the air entry pressure  $\alpha$ , and the pore-size distribution parameter  $n$  of the given soil composition. These water retention parameters can be used in the Van Genuchten [1980] equation

$$\Theta(h) = \Theta_r + \frac{\Theta_s - \Theta_r}{(1 + (\alpha|h|)^n)^{(1-1/n)}}, \quad (\text{B.1})$$

to calculate the water content  $\Theta(h)$  at any pressure head  $h$ . In soil science, the pressure head is often expressed by the dimensionless pF value, i.e., the potential of a soil matrix to held water against gravity [Hartge and Horn, 2014]. The water content at a matrix tension of pF 1.8 ( $= -10^{1.8} \Leftrightarrow h \approx -60$  cm) is defined as the field capacity (FC) [Durner and Iden, 2011], where FC quantifies the soil's maximum plant available water balanced with air such that a soil at field capacity is considered ideal for crop performance.

Here, the sand, silt, and clay contents of the Auger probes were correlated with the inverted electrical conductivities and the obtained regression parameters were used to upscale the soil textural information to the individual layers. The obtained sand, silt, and clay contents were then used in ROSETTA to obtain the Van Genuchten [1980] parameters. These were inserted into Equation B.1 to predict the FC variations over depth attributed to the structural changes reflected by the lateral changing  $\sigma(z_i)$ .

### B.4.2 Toward 3D field capacity

The quantitative EMI data of the approximately 2.55 ha large test site were inverted for three layers, which obtained a quasi-3D subsurface electrical conductivity model

presented in Figure B.5a. Roughly, the inverted lateral and vertical  $\sigma$  values clearly reflected the sand and gravel dominated UT sediments by relatively low electrical conductivities (around 5 mS/m) and the finer textured paleo-river channel fillings by  $\sigma$  values of up to 25 mS/m.

The depth-dependent electrical conductivity changes were extracted at the Auger positions and correlated to the sand, silt, and clay contents of the specific horizons using linear and exponential regression models. To judge between the models, the coefficient of determination ( $R^2$ ) was used. In the linear case,  $R^2$  of 0.016, 0.139, and 0.395 were obtained for the  $\sigma(z_i)$ -silt, -sand, and -clay regressions, respectively. Hence, no, low and moderate correlations were obtained for the inverted electrical conductivities with silt, sand, and clay such that silt was excluded in the following regression analysis. The exponential model (Figure B.4) increased the  $R^2$  to 0.157 and 0.440 for  $\sigma(z_i)$  with sand and clay, respectively. Therefore, the exponential models were used in the upscaling approach of the sand and clay contents based on the quasi-3D inverted electrical conductivities, while the silt content was obtained by closing the mass balance.

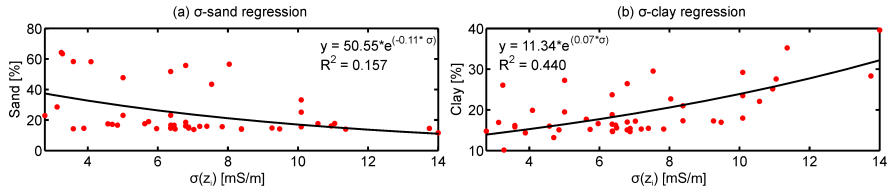


Figure B.4: Exponential regression between  $\sigma(z_i)$  and (a) sand and (b) clay. The obtained parameters were used to upscale the textural information based on the inverted electrical conductivities to the entire field.

The obtained lateral and vertical sand, silt, and clay distributions were used in ROSETTA to estimate the water retention parameters that were inserted into Equation B.1 to calculate the 3D field capacity based on the inverted electrical conductivities, see Figure B.5b. The predicted field capacity of the UT sediments was around  $0.35 \text{ m}^3/\text{m}^3$ , which is overestimated because Saxton and Rawls [2006] for example found approximately half of that value for sandy soils. This misestimate was probably due to the sparse Auger probings that were mainly taken along the paleo-river channels, see Figure 5.4e, which resulted in limited UT soil samples such that too few information

about the coarser sediments were obtained. However, the FC of the paleo-river channel material was estimated with  $\approx 0.45 \text{ m}^3/\text{m}^3$  that coincides with the literature values for silty and clay rich soils [Saxton and Rawls, 2006] indicating that the three-layer inversions of the ME data could describe the upper 1 m (Auger) depth.

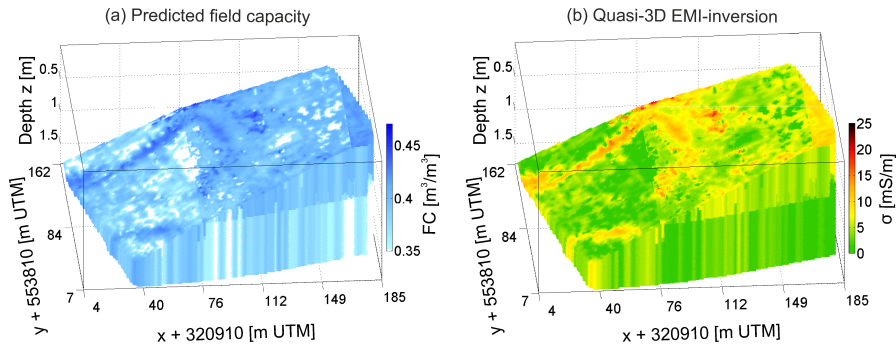


Figure B.5: Diagonally layer cut through (a) the quasi-3D EMI inversion results and (b) the predicted field capacity of the approximately 2.55 ha large paleo-river channel field.

## B.5 Large-Scale ECa Maps of campaign II

In campaign II, large-scale EMI data were recorded with the ME in VCP and the SE in HCP mode. The available data could be used for three-layer inversions with a deeper resolution compared to campaign I. Whereas the first survey delivered information up to about 1.80 m depth, the deepest sensing HCPs180 coil of campaign II measured up to  $\approx 2.70$  m.

In both campaigns, the ME recorded ECa values in the VCP s32, s71, and s118 coil configurations that are most sensitive close to the surface, decrease rapidly with depth. The ECa values of the VCP coils were relatively high ( $\approx 10 \text{ mS/m}$ ) in the first campaign (Figure 4.6), whereas relatively low in the second campaign indicating a relatively moist and dry ploughing layer in campaign I and campaign II, respectively, due to high and low precipitation rates in July 2012 and July 2015, Figure B.2.

The ECa values of the material surrounding the paleo-river channels were relatively low ( $\approx 5 \text{ mS/m}$ ) for the shallow and for the intermediate deep sensing coil configurations (VCPs32, VCPs71, VCPs118, HCPs49, HCPs71) except for HCPs35 probably due to

post-calibration errors. The ECa values of the deep sensing coil configurations, i.e., HCPs97, HCPs135, and HCPs180, increased to approximately 7-10 mS/m indicating an increasing electrical conductivity with depth.

The paleo-river channels were not visible with the VCPs32 coil configuration, relatively weak for VCPs71 ( $ECa \approx 7$  mS/m), and prominently for the VCPs118, HCPs71, and HCPs97 ( $ECa$  approximately 11-15 mS/m). For the deep sensing HCPs135 and HCPs180 coils, the ECa values decreased again to  $\approx 10$  mS/m such that the paleo-river channels are interpretively expected between 0.5 m and 1.5 to 1.8 m depth.

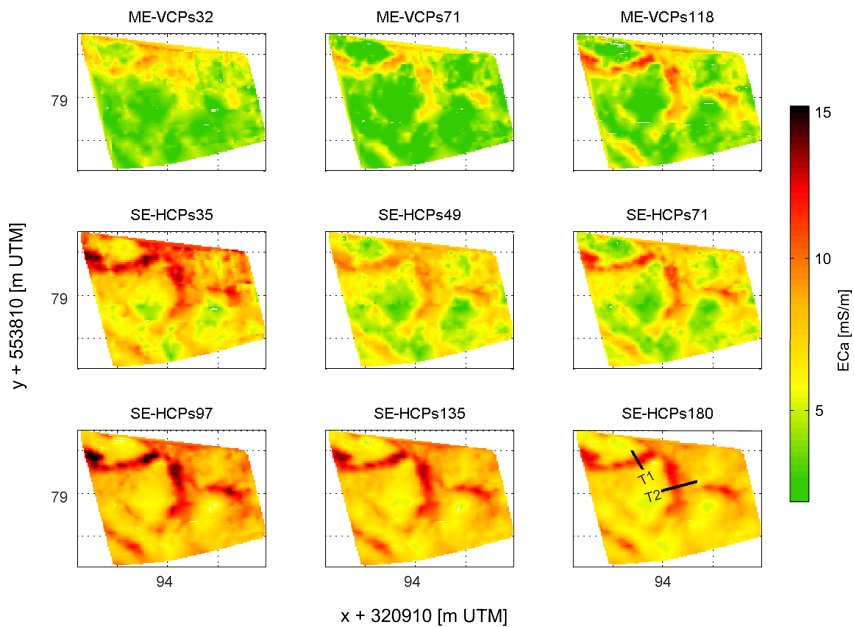


Figure B.6: Multiple device large-scale ECa maps of campaign II recorded at the paleo-river channel field, where the SE-HCPs180 map shows the locations of the two transects (T1 and T2) that were used in the detailed analysis.

## B.6 Additional Transect Analysis Results

### Transect T1

The present section compares the four- and five-layer inversion results obtained at the borehole locations of transect T1 with the extracted soil cores in the Figures B.7 and B.8, respectively. The upper panel shows the inverted electrical conductivities and the textural information of the soil horizons as well as with the predicted field capacity. The lower panel compares the  $\sigma(z_i)$  with the sand and clay contents that nicely shows that the horizons were well reconstructed and that the inverted electrical conductivities follow the clay contents and therefore the predicted field capacity.

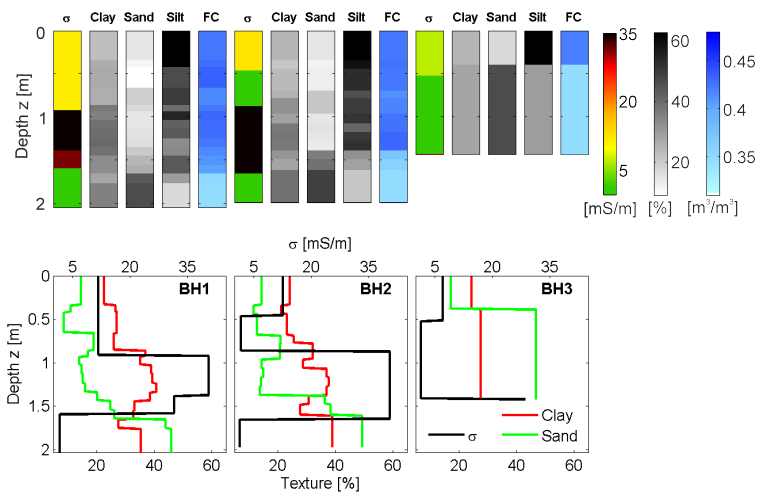


Figure B.7: Four-layer inversion results compared to the soil cores drilled at transect T1.

Both inversion schemes resolved subtle details in the soil compositions. For example, the 4-layer inversion reconstructed a layer with 35 mS/m at around 1 m depth that decreased to 30 mS/m at around 1.5 m depth. At approximately these depths, the clay content decreased from around 40 to 35% while the sand content increased. The 5-layer inversions obtained similar details showing that the EMI methodology can be used for quantitative vadose zone characterizations.

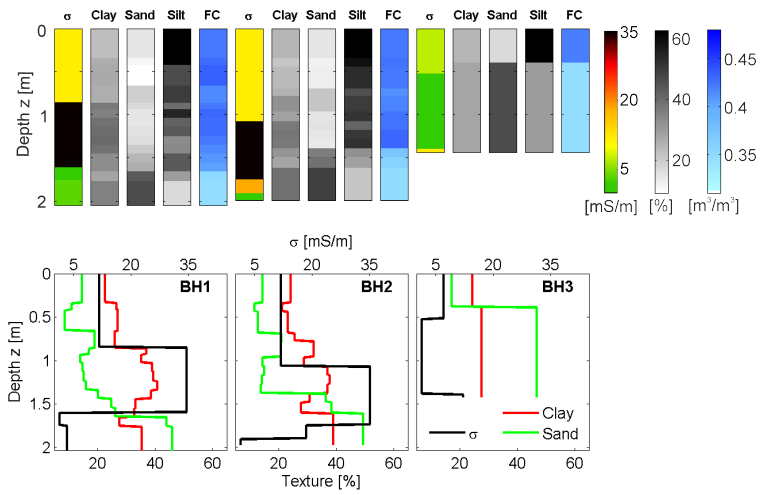


Figure B.8: Five-layer inversion result compared to the soil cores drilled at transect T1.

## Transect T2

Whereas T1 crossed the E-W directed paleo-river channel, T2 was perpendicular to the N-S directed channel. The four-layer and five-layer inversion results extracted at the borehole locations are compared to the analyzed soil texture in Figure B.9 and B.10, respectively. Similar to the T1 results, the inversions obtained details in the soil textural changes. However, the results were not as clear as the T1 results because the  $\sigma(z_i)$  seem to follow the sand contents that increase in the N-S directed paleo-river channel (while sand decreased in T1), which indicates that the clayey material in these N-S directed channels show a higher electrical conductivity compared to the E-W directed channel.

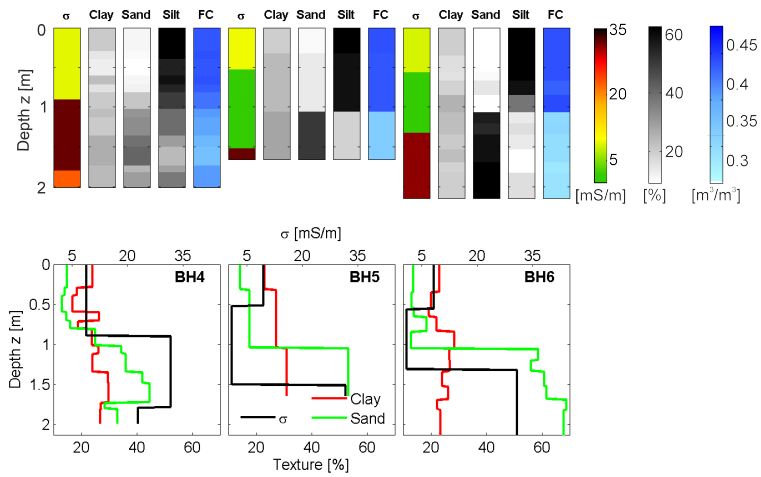


Figure B.9: Four-layer inversion results compared to the soil cores drilled at transect T2.

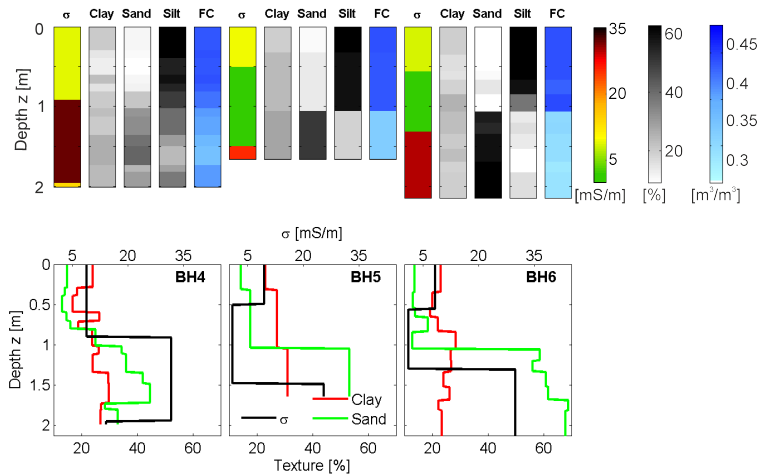


Figure B.10: Five-layer inversion results compared to the soil cores drilled at transect T2.



## Appendix C

# DREAM on Synthetic and Experimental Data

### C.1 Synthetic Data Inversion using SCE and DREAM<sub>ZS</sub>

This section tests the reliability of the inversion algorithms on two three-layer models that were based on agricultural field properties, where  $h_{1,2} = [0.3, 0.9]$  m and  $\sigma_{1,2,3}$  were 10, 20, and 50 mS/m either increasing or decreasing. These models together with the ME, SE, and DUEM settings were used in the exact EM-FM (Equations 2.7 to 2.9) to generate synthetic data. The synthetic measurements of all 24 coil configurations (compare Table C.1) were noise-free and contaminated with 4% random noise because the ME and SE have a reported accuracy of 4% at 50 mS/m [GF-Instruments, 2011].

Table C.1: Multi-coil EMI device configurations used to generate the synthetic measurements in the present and next section and used in the later parts to characterize the test sites.

EMI device	Receiver	Orientation	Separation [cm]	Frequency [kHz]	Coil # in Figure C.2e, C.2f, C.3
ME	3	VCP , HCP	32, 71, 118	30	1:3 , 4:6
SE	6	VCP , HCP	35, 49, 71, 97, 135, 180	25.17	7:12 , 13:18
DUEM	3 + 3	PRP + HCP	110, 210, 410 + 100, 200, 400	9	19:21 , 22:24

The noisy and noise-free data were inverted for three-layers such that a five-dimensional parameter search space was explored by both SCE and DREAM. Since the algorithms require a sufficiently large parameter space, the lower and upper bounds

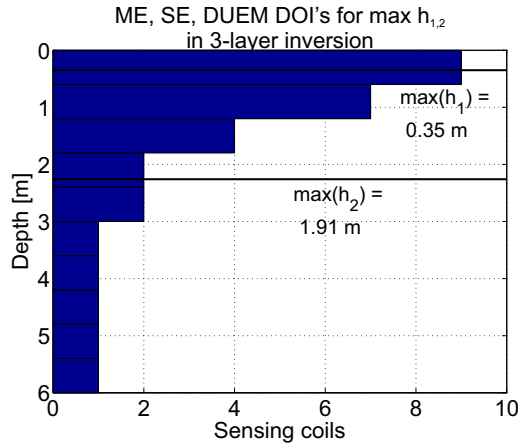


Figure C.1: Histogram over the depth of investigations of multiple EMI devices used to set the maximum layer thicknesses of the parameter search space.

for the three electrical conductivities were set by multiplying the min and max ECa by 0.5 and 2, respectively. For the layer thicknesses, the lower bound was 0.1 m while for the upper bound the DOI's and prior information were used to set  $h_1 = 0.35 \text{ m}$  and  $h_2 = 1.91 \text{ m}$  (see Figure C.1). Note, that when inverting for more layers, the maximum thicknesses decrease while the resolution increases (within the imaging capabilities determined by the DOI's).

Figure C.2 shows the models (red lines) and the SCE and DREAM reconstructions in blue and black, respectively. In the case of noise-free data, both algorithms perfectly reconstructed the true models with increasing and decreasing  $\sigma$  with depth (Figures C.2a and C.2b), where SCE took around 3 hours to converge to the global minimum after 2412 CCE and shuffling processes. In DREAM, 50000 runs were evaluated, which took around 14 hours on a laptop with 2.2 GHz Intel(R) Core(TM) I5 processor and 12 GB RAM.

In the case of noise-contaminated synthetic data, SCE converged in around 2 hours exploring 2407 parameter combinations and the 50000 runs in DREAM needed around 11.5 hours. The model reconstructions of SCE and DREAM are shown in Figure C.2c and C.2d for the cases of increasing and decreasing electrical conductivity with depth, respectively. Visually inspected, both algorithms optimized parameter sets, i.e., the most likely or maximum a posteriori (MAP) set for DREAM, that were close to the true

models. However, the error in the reconstruction of the low electrical conductive upper layer (increasing  $\sigma$  with depth) propagated into depths, whereas the upper part in the decreasing case was better reconstructed resulting in a better reconstruction of the deeper parts. Observing the last 10000 runs of DREAM, grey shaded, the true models were included, which indicates the applicability for uncertainty analysis.

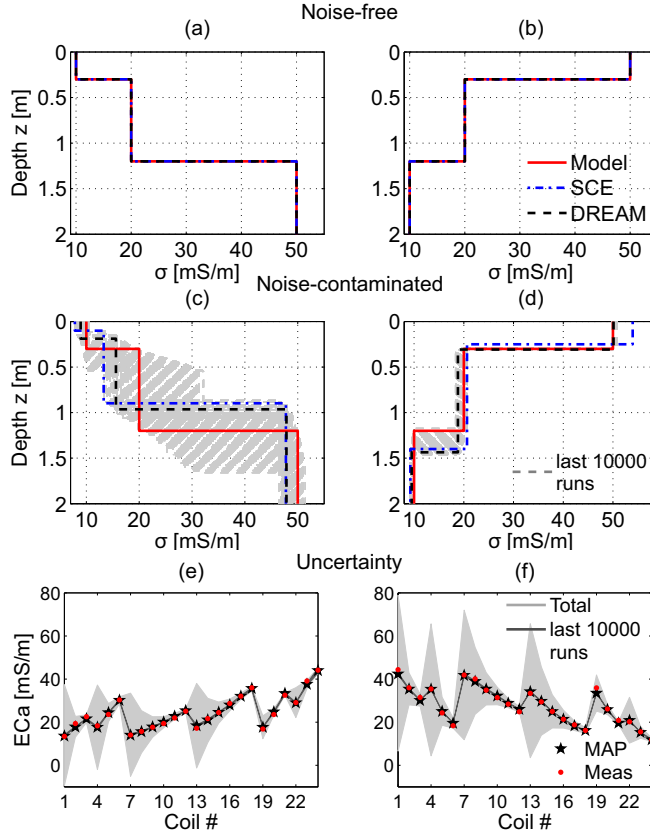


Figure C.2: SCE and DREAM reconstructions of the red models shown in blue and black for (a), (b) noise-free and (c), (d) noisy data including the last 10000 runs of DREAM. (e) and (f) show the total and least uncertainties in light and dark grey. Black stars and red dots show the maximum a posteriori (MAP) values and the measurements. In Table 2.1 the coil # are related to the EMI device coil configurations.

The uncertainties are shown in Figure C.2e and C.2f. To better grasp the results, the magnetic field ratios (the quantity in the inversions) were converted into synthetic ECa values using the exact ECa conversion described in Section 3.1. Overall, the uncertainties decrease with increasing runs, since the last 10000 evaluations formed a very narrow

area around the synthetic ECa. For the individual coil configurations, the uncertainties decrease with increasing coil separation for all EMI devices, use Table 2.1 to relate the coil # on the x-axis to the respective EMI device and coil configuration, however in both cases the MAP values converged close to the synthetic measurements. To conclude, the implemented SCE algorithm reconstructs the presented cases of noise-free and noise-contaminated data reasonably well and relatively fast indicating its applicability to experimental EMI data and the DREAM algorithm is well suited to analyze the uncertainties that are inherent in the measurements.

## C.2 Experimental Data Inversion using SCE and DREAM<sub>ZS</sub>

Figure C.3a shows a histogram over the coil specific depth of investigations that was used to set the maximum layer depth in the inversions. Here, the possible boundaries for four layers are presented. In Figure C.3b the expected error of the measurements are presented. The data were recorded for around 30 seconds at the three calibration locations in E-W and N-S direction to draw the standard deviation (std). For each EMI device, see Table 2.1 to relate the coil # to the specific coil configuration, the mean value of the coil specific std was converted to the magnetic field (the quantity being inverted) and passed to DREAM.

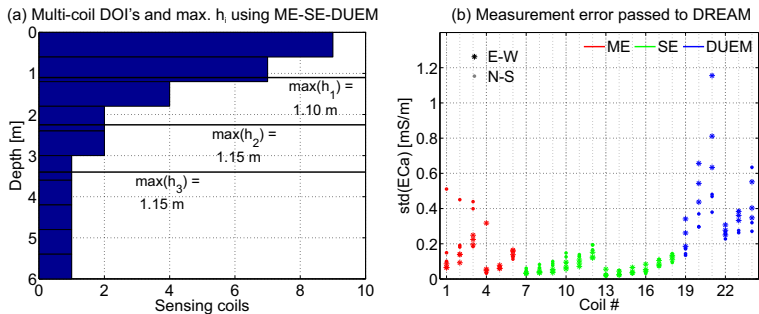


Figure C.3: (a) Maximum layer boundaries used for the four-layer inversions of campaign II data used here to span the DREAM parameter space. (b) Standard deviation of the multiple EMI devices used to estimate the measurement error that was passed to DREAM. Each device was directed E-W and N-S to record data for around 30 sec at the three calibration locations.

The multi-coil ECa values of the boreholes BH1 and BH2 of transect T2 were inverted for four layers using SCE and DREAM presented in Section 2.2. The model runs in DREAM were set to 300000, which took around 45 hours to invert the data of the two borehole locations, whereas the parallelized SCE code inverted relatively fast on the IBG3 computer cluster.

Figure C.4 shows the obtained results of SCE and DREAM as well as the last 10000 model runs of DREAM compared to the real paleo-river channel depths. In both BH1 and BH2, the DREAM algorithm reconstructed a thicker paleo-river channel compared to the real depths and the SCE code, which was compensated with a lesser (approximately 5 mS/m) electrical conductivity compared to the SCE inversion results.

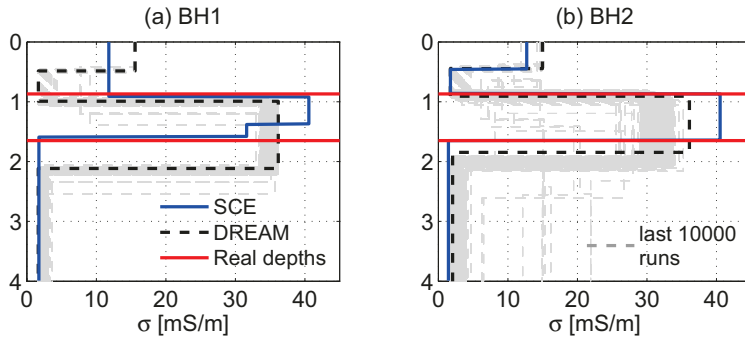


Figure C.4: Multi-coil ECa values inverted at the borehole locations (a) BH1 and (b) BH2 using the four-layer SCE (blue) and DREAM (black) inversion algorithms. Also shown the last 10000 runs of DREAM (grey shaded) as well as the real paleo-river channel depths in red.

Conclusively, the DREAM algorithm strongly depends on the expected error that was possibly not well enough determined such that more research is needed to optimize DREAM for the EMI-inversion uncertainty analysis.



# Bibliography

- Abdu, H., Robinson, D. A., Seyfried, M., Jones, S. B. (2008): Geophysical imaging of watershed subsurface patterns and prediction of soil texture and water holding capacity, *Water Resources Research*, 44, W00D18. [2](#)
- Adamchuk, V. I., Hummel, J. W., Morgan, M. T., Upadhyaya, S. K. (2004): On-the-go soil sensors for precision agriculture, *Computers and Electronics in Agriculture*, 44, 71–91. [3](#)
- Aldorff, D., Bechtold, M., van der Kruk, J., Vereecken, H., Huisman, J. A. (2016): Mapping peat layer properties with multi-coil offset electromagnetic induction and laser scanning elevation data, *Geoderma*, 261, 178–189. [25](#)
- Aldorff, D., von Hebel, C., Borchard, N., van der Kruk, J., Bogena, H., Vereecken, H., Huisman, J. A. (submitted): Potential of catchment-wide soil water content mapping using electromagnetic induction in a forest ecosystem, *Soil Use and Management*. [27](#)
- Auken, E., Christiansen, A. V., Jacobsen, B. H., Foged, N., Sørensen, K. I. (2005): Piecewise 1D laterally constrained inversion of resistivity data, *Geophysical Prospecting*, 53, 497–506. [11](#)
- Barker, R. D. (1989): Depth of investigation of collinear symmetrical four electrode arrays, *GEOPHYSICS*, 54, 1031–1037. [29](#)
- Beamish, D. (2011): Low induction number, ground conductivity meters: A correction procedure in the absence of magnetic effects, *Journal of Applied Geophysics*, 75, 244–253. [5](#), [16](#), [18](#)
- Bikowski, J., Huisman, J. A., Vrugt, J. A., Vereecken, H., van der Kruk, J. (2012): Integrated analysis of waveguide dispersed GPR pulses using deterministic and Bayesian

- inversion methods, *Near surface geophysics*, 10, 641–652. [14](#)
- Binley, A., Hubbard, S. S., Huisman, J. A., Revil, A., Robinson, D. A., Singha, K., Slater, L. D. (2015): The emergence of hydrogeophysics for improved understanding of subsurface processes over multiple scales, *Water Resources Research*, pp. n/a–n/a. [1](#)
- Bogena, H. R., Herbst, M., Huisman, J. A., Rosenbaum, U., Weuthen, A., Vereecken, H. (2010): Potential of Wireless Sensor Networks for Measuring Soil Water Content Variability, *Vadose Zone Journal*, 9, 1002–1013. [2](#)
- Busch, S., van der Kruk, J., Vereecken, H. (2014): Improved characterization of fine-texture soils using on-ground GPR full-waveform inversion, *Ieee Transactions on Geoscience and Remote Sensing*, 52, 3947–3958. [38](#)
- Callegary, J. B., Ferre, T. P. A., Groom, R. W. (2007): Vertical spatial sensitivity and exploration depth of low-induction-number electromagnetic-induction instruments, *Vadose Zone Journal*, 6, 158–167. [5](#), [16](#), [18](#)
- Callegary, J. B., Ferre, T. P. A., Groom, R. W. (2012): Three-Dimensional Sensitivity Distribution and Sample Volume of Low-Induction-Number Electromagnetic-Induction Instruments, *Soil Science Society of America Journal*, 76, 85–91. [41](#)
- Corwin, D. L., Lesch, S. M. (2003): Application of soil electrical conductivity to precision agriculture: Theory, principles, and guidelines, *Agronomy Journal*, 95, 455–471. [3](#)
- Corwin, D. L., Plant, R. E. (2005): Applications of apparent soil electrical conductivity in precision agriculture, *Computers and Electronics in Agriculture*, 46, 1–10. [3](#)
- Dafflon, B., Hubbard, S. S., Ulrich, C., Peterson, J. E. (2013): Electrical Conductivity Imaging of Active Layer and Permafrost in an Arctic Ecosystem, through Advanced Inversion of Electromagnetic Induction Data, *gsvadzone*, 12, -. [5](#)
- Dejong, E., Ballantyne, A. K., Cameron, D. R., Read, D. W. L. (1979): Measurement of apparent electrical conductivity of by an electromagnetic induction probe to aid salinity surveys, *Soil Science Society of America Journal*, 43, 810–812. [3](#)

- Delefortrie, S., Saey, T., Van De Vijver, E., De Smedt, P., Missiaen, T., Demerre, I., Van Meirvenne, M. (2014): Frequency domain electromagnetic induction survey in the intertidal zone: Limitations of low-induction-number and depth of exploration, *Journal of Applied Geophysics*, 100, 14–22. [16](#), [17](#)
- Doolittle, J. A., Sudduth, K. A., Kitchen, N. R., Indorante, S. J. (1994): Estimating depths to claypans using electromagnetic induction methods, *Journal of Soil and Water Conservation*, 49, 572–575. [3](#)
- dos Santos, V. R. N., Porsani, J. L. (2011): Comparing performance of instrumental drift correction by linear and quadratic adjusting in inductive electromagnetic data, *Journal of Applied Geophysics*, 73, 1–7. [4](#)
- Duan, Q. Y., Sorooshian, S., Gupta, V. K. (1992): Effective and efficient global optimization for conceptual rainfall-runoff models, *Water Resources Research*, 28, 1015–1031. [11](#)
- Duan, Q. Y., Gupta, V. K., Sorooshian, S. (1993): Suffled complex evolution approach for effective and efficient global minimization, *Journal of Optimization Theory and Applications*, 76, 501–521. [12](#)
- Durner, W., Iden, S. C. (2011): Bodenphysikalische Versuche, TU Braunschweig,, Institut für Geoökologie, Abteilung Bodenkunde und Bodenphysik. [89](#)
- Ekinci, Y. L., Demirci, A. (2008): A Damped Least-Squares Inversion Program for the Interpretation of Schlumberger Sounding Curves, *Journal of Applied Sciences*, 8, 4070–4078. [79](#)
- Fitterman, D. V., Labson, V. F. (2005): 10. Electromagnetic Induction Methods for Environmental Problems, in: *Near-Surface Geophysics*, pp. 301–356. [7](#)
- Gebbers, R., Lueck, E., Dabas, M., Domsch, H. (2009): Comparison of instruments for geoelectrical soil mapping at the field scale, *Near Surface Geophysics*, 7, 179–190. [4](#), [23](#)
- GF-Instruments (2011): CMD electromagnetic conductivity meter user manual V. 1.5, GF Instruments s.r.o. Geophysical Equipment and Services. [23](#), [97](#)

- Guillemoteau, J., Tronicke, J. (2015): Non-standard electromagnetic induction sensor configurations: Evaluating sensitivities and applicability, *Journal of Applied Geophysics*, 118, 15–23. [22](#)
- Gupta, P. K., Niwas, S., Gaur, V. K. (1997): Straightforward inversion of vertical electrical sounding data, *Geophysics*, 62, 775–785. [79](#)
- Hardie, M., Doyle, R. (2012): Measuring soil salinity, in: *Methods Molecular Biology*, edited by Shabala, S., Cuin, T. A., vol. 913, pp. 415–425, Springer, New York Heidelberg Dordrecht London, 2012/08/17 edn. [2](#)
- Hartge, K. H., Horn, R. (2014): *Einführung in die Bodenphysik*, Schweizerbart Science Publishers, Stuttgart, Germany. [89](#)
- Hendrickx, J. M. H., Borchers, B., Corwin, D. L., Lesch, S. M., Hilgendorf, A. C., Schlue, J. (2002): Inversion of soil conductivity profiles from electromagnetic induction measurements: Theory and experimental verification, *Soil Science Society of America Journal*, 66, 673–685. [16](#), [17](#)
- Igel, J. (2007): *On the Small-Scale Variability of Electrical Soil Properties and its Influence on Geophysical Measurements*, Ph.d. thesis, Johann Wolfgang Goethe University. [29](#), [81](#)
- ISO 11277, D. (2002): *Bestimmung der Partikelgrößenverteilung in Mineralböden*, DIN Deutsches Institut für Normung e.V. [58](#)
- Kaufman, A. A., Keller, G. V. (1983): *Frequency and transient soundings*, *Methods in geochemistry and geophysics* ;16, Elsevier Scientific Pub. Co., Amsterdam ; New York. [4](#)
- Keller, G. V., Frischknecht, F. (1966): *Electrical methods of geophysical prospecting*, *International Series of Monographs in Electromagnetic Waves*, Pergamon Press, Oxford, New York, 10. [4](#)
- Kerr, Y. H., Waldteufel, P., Wigneron, J. P., Martinuzzi, J. M., Font, J., Berger, M. (2001): Soil moisture retrieval from space: The Soil Moisture and Ocean Salinity (SMOS) mission, *Ieee Transactions on Geoscience and Remote Sensing*, 39, 1729–1735. [2](#)

- Kirsch, R. (2009): Groundwater geophysics, Springer-Verlag Berlin Heidelberg New York, Berlin; Heidelberg, 2 edn. [25](#)
- Knödel, K.; Lange, G. V. H.-J. (2007): Environmental Geology, Springer-Verlag Berlin Heidelberg New York, Heidelberg. [78](#)
- Koefoed, O. (1970): A fast method for determining the layer distribution from the raised kernel function in geoelectrical sounding, Geophysical Prospecting, 18, 564–570. [79](#)
- Laloy, E., Vrugt, J. A. (2012): High-dimensional posterior exploration of hydrologic models using multiple-try DREAM((ZS)) and high-performance computing, Water Resources Research, 48, 18. [13](#), [14](#)
- Lavoué, F., van der Kruk, J., Rings, J., Andre, F., Moghadas, D., Huisman, J. A., Lambot, S., Weihermüller, L., Vanderborght, J., Vereecken, H. (2010): Electromagnetic induction calibration using apparent electrical conductivity modelling based on electrical resistivity tomography, Near Surface Geophysics, 8, 553–561. [4](#), [5](#), [16](#), [25](#), [38](#)
- Lesch, S. M., Rhoades, J. D., Lund, L. J., Corwin, D. L. (1992): Mapping soil-salinity using calibrated electromagnetic measurements, Soil Science Society of America Journal, 56, 540–548. [3](#)
- Linde, N., Vrugt, J. A. (2013): Distributed Soil Moisture from Crosshole Ground-Penetrating Radar Travel Times using Stochastic Inversion, Vadose Zone Journal, 12. [13](#), [14](#)
- Mboh, C. M., Huisman, J. A., Vereecken, H. (2011): Feasibility of Sequential and Coupled Inversion of Time Domain Reflectometry Data to Infer Soil Hydraulic Parameters under Falling Head Infiltration, Soil Sci. Soc. Am. J., 75, 775–786. [11](#), [12](#)
- McNeill, J. D. (1980): Electromagnetic terrain conductivity measurement at low induction numbers, Technical Note TN-6. Geonics Ltd., Mississauga, ON, Canada. [3](#), [5](#), [16](#), [17](#), [41](#)
- McNeill, J. D., Bosnar, M. (1999): Application of "dipole-dipole" electromagnetic sys-

- tens for geological depth sounding, Technical Note TN-31. Geonics Ltd., Mississauga, ON, Canada. [5](#), [16](#), [17](#)
- Mester, A., van der Kruk, J., Zimmermann, E., Vereecken, H. (2011): Quantitative two-layer conductivity inversion of multi-configuration electromagnetic induction measurements, *Vadose Zone Journal*, 10, 1319–1330. [5](#), [10](#), [11](#), [25](#), [33](#)
- Milbert, G. (2016): Altersbestimmung von verschütteten Flußstrukturen Selhausen. [53](#)
- Minsley, B. J., Smith, B. D., Hammack, R., Sams, J. I., Veloski, G. (2012): Calibration and filtering strategies for frequency domain electromagnetic data, *Journal of Applied Geophysics*, 80, 56–66. [4](#), [25](#), [39](#)
- Moghadas, D., Andre, F., Bradford, J. H., van der Kruk, J., Vereecken, H., Lambot, S. (2012): Electromagnetic induction antenna modelling using a linear system of complex antenna transfer functions, *Near Surface Geophysics*, 10, 237–247. [4](#)
- Montzka, C., Moradkhani, H., Weihermüller, L., Franssen, H.-J. H., Canty, M., Vereecken, H. (2011): Hydraulic parameter estimation by remotely-sensed top soil moisture observations with the particle filter, *Journal of Hydrology*, 399, 410–421. [2](#)
- Nüsch, A., Dietrich, P., Werban, U., Behrens, T. (2010): Acquisition and reliability of geophysical data in soil science, 19th World Congress of Soil Science - Solutions for a Changing World. [4](#), [23](#)
- Piikki, K., Wetterlind, J., Soderstrom, M., Stenberg, B. (2015): Three-dimensional digital soil mapping of agricultural fields by integration of multiple proximal sensor data obtained from different sensing methods, *Precision Agriculture*, 16, 29–45. [3](#)
- Robinson, D. A., Jones, S. B., Wraith, J. M., Or, D., Friedman, S. P. (2003): A Review of Advances in Dielectric and Electrical Conductivity Measurement in Soils Using Time Domain Reflectometry, *Vadose Zone Journal*, 2, 444–475. [2](#)
- Robinson, D. A., Campbell, C. S., Hopmans, J. W., Hornbuckle, B. K., Jones, S. B., Knight, R., Ogden, F., Selker, J., Wendroth, O. (2008): Soil moisture measurement for ecological and hydrological watershed-scale observatories: A review, *Vadose Zone Journal*, 7, 358–389. [1](#)

- Robinson, D. A., Lebron, I., Kocar, B., Phan, K., Sampson, M., Crook, N., Fendorf, S. (2009): Time-lapse geophysical imaging of soil moisture dynamics in tropical deltaic soils: An aid to interpreting hydrological and geochemical processes, *Water Resources Research*, 45. [2](#)
- Robinson, D. A., Abdu, H., Lebron, I., Jones, S. B. (2012): Imaging of hill-slope soil moisture wetting patterns in a semi-arid oak savanna catchment using time-lapse electromagnetic induction, *Journal of Hydrology*, 416, 39–49. [2](#)
- Rosas-Carbajal, M., Linde, N., Kalscheuer, T., Vrugt, J. A. (2013): Two-dimensional probabilistic inversion of plane-wave electromagnetic data: Methodology, model constraints and joint inversion with electrical resistivity data, *Geophysical Journal International*. [13](#)
- Rosenbaum, U., Bogaen, H. R., Herbst, M., Huisman, J. A., Peterson, T. J., Weuthen, A., Western, A. W., Vereecken, H. (2012): Seasonal and event dynamics of spatial soil moisture patterns at the small catchment scale, *Water Resources Research*, 48. [2](#)
- Roy, A. (1972): Depth of investigation in Wenner, three-electrode and dipole-dipole DC resistivity methods, *Geophysical Prospecting*, 20, 329–340. [29](#)
- Roy, A., Apparao, A. (1971): Depth of investigation in direct current methods, *Geophysics*, 36, 943–959. [29](#)
- Rubin, Y.; Hubbard, S. (2005): *Hydrogeophysics*, vol. 50, Springer-Verlag, Dordrecht, The Netherlands. [1](#)
- Rudolph, S., van der Kruk, J., von Hebel, C., Ali, M., Herbst, M., Montzka, C., Patzold, S., Robinson, D. A., Vereecken, H., Weihermuller, L. (2015): Linking satellite derived LAI patterns with subsoil heterogeneity using large-scale ground-based electromagnetic induction measurements, *Geoderma*, 241, 262–271. [2](#), [27](#), [52](#), [58](#), [60](#)
- Saey, T., De Smedt, P., Islam, M. M., Meerschman, E., De Vijver, E. V., Lehouck, A., Van Meirvenne, M. (2012): Depth slicing of multi-receiver EMI measurements to enhance the delineation of contrasting subsoil features, *Geoderma*, 189, 514–521. [5](#)
- Saey, T., De Smedt, P., De Clercq, W., Meerschman, E., Islam, M. M., Van Meirvenne,

- M. (2013): Identifying Soil Patterns at Different Spatial Scales with a Multi-Receiver EMI Sensor, *Soil Science Society of America Journal*, 77, 382–390. [3](#)
- Santos, F. A. M., Triantafyllis, J., Bruzgulis, K. E., Roe, J. A. E. (2010): Inversion of multiconfiguration electromagnetic (DUALEM-421) profiling data using a one-dimensional laterally constrained algorithm, *Vadose Zone Journal*, 9, 117–125. [5](#)
- Saxton, K. E., Rawls, W. J. (2006): Soil Water Characteristic Estimates by Texture and Organic Matter for Hydrologic Solutions, *Soil Science Society of America Journal*, 70. [90](#), [91](#)
- Schaap, M. G., Leij, F. J., van Genuchten, M. T. (2001): rosetta: a computer program for estimating soil hydraulic parameters with hierarchical pedotransfer functions, *Journal of Hydrology*, 251, 163–176. [89](#)
- Schaap, M. G., Nemes, A., van Genuchten, M. T. (2004): Comparison of Models for Indirect Estimation of Water Retention and Available Water in Surface Soils, *Vadose Zone Journal*, 3, 1455–1463. [89](#)
- Shanahan, P. W., Binley, A., Whalley, W. R., Watts, C. W. (2015): The Use of Electromagnetic Induction to Monitor Changes in Soil Moisture Profiles beneath Different Wheat Genotypes, *Soil Sci. Soc. Am. J.*, 0, -. [4](#)
- Sheets, K. R., Hendrickx, J. M. H. (1995): Noninvasive soil water content measurement using electromagnetic induction, *Water Resources Research*, 31, 2401–2409. [2](#)
- Slob, E., Fokkema, J. (2002): Coupling effects of two electric dipoles on an interface, *Radio Science*, 37. [8](#)
- Sørensen, K., Auken, E. (2004): SkyTEM - a new high-resolution helicopter transient electromagnetic system, *Exploration Geophysics*, 35, 194–202. [2](#)
- Stadler, A., Rudolph, S., Kupisch, M., Langensiepen, M., van der Kruk, J., Ewert, F. (2015): Quantifying the effects of soil variability on crop growth using apparent soil electrical conductivity measurements, *European Journal of Agronomy*, 64, 8–20. [3](#)
- Sudduth, K. A., Drummond, S. T., Kitchen, N. R. (2001): Accuracy issues in electromagnetic induction sensing of soil electrical conductivity for precision agriculture,

- Computers and Electronics in Agriculture, 31, 239–264. [4](#)
- Sudduth, K. A., Kitchen, N. R., Bollero, G. A., Bullock, D. G., Wiebold, W. J. (2003): Comparison of Electromagnetic Induction and Direct Sensing of Soil Electrical Conductivity, *Agron. J.*, 95, 472–482. [23](#)
- Sudduth, K. A., Kitchen, N. R., Wiebold, W. J., Batchelor, W. D., Bollero, G. A., Bullock, D. G., Clay, D. E., Palm, H. L., Pierce, F. J., Schuler, R. T., Thelen, K. D. (2005): Relating apparent electrical conductivity to soil properties across the north-central USA, *Computers and Electronics in Agriculture*, 46, 263–283. [3](#)
- Szalai, S. (2000): About The Depth Of Investigation Of Different D.C. Dipole-Dipole Arrays, *Acta Geodaetica et Geophysica Hungarica*, 35, 63–73. [29](#)
- Tarantola, A. (2005): Inverse problem theory and methods for model parameter estimation, Society for Industrial Mathematics. [13](#)
- Telford, W. M., P., G. L., E., S. R. (1990): Applied geophysics, Cambridge University Press, Cambridge [England]; New York. [3](#)
- Triantafyllis, J., Wong, V., Santos, F. A. M., Page, D., Wege, R. (2012): Modeling the electrical conductivity of hydrogeological strata using joint-inversion of loop-loop electromagnetic data, *Geophysics*, 77, WB99–WB107. [5](#)
- van der Kruk, J., Gueting, N., Klotzsche, A., He, G., Rudolph, S., von Hebel, C., Yang, X., Weihermüller, L., Mester, A., Vereecken, H. (2015): Quantitative multi-layer electromagnetic induction inversion and full-waveform inversion of crosshole ground penetrating radar data, *Journal of Earth Science*, 26, 844–850. [27](#)
- Van Genuchten, M. T. (1980): A closed-form equation for predicting the hydraulic conductivity of unsaturated soils, *Soil science society of America journal*, 44, 892–898. [89](#)
- van Nostrand, R. G.; Cook, K. L. (1984): Interpretation of resistivity data, Geological survey professional paper 499, US Geological Survey, Washington. [78](#)
- Vereecken, H., Maes, J., Feyen, J. (1990): Estimating unsaturated hydraulic conductivity from easily measured soil properties, *Soil Science*, 149, 1–12. [89](#)

- Vereecken, H., Huisman, J. A., Bogena, H., Vanderborght, J., Vrugt, J. A., Hopmans, J. W. (2008): On the value of soil moisture measurements in vadose zone hydrology: A review, *Water Resources Research*, 44. [1](#)
- von Hebel, C., Rudolph, S., Mester, A., Huisman, J. A., Kumbhar, P., Vereecken, H., van der Kruk, J. (2014): Three-dimensional imaging of subsurface structural patterns using quantitative large-scale multiconfiguration electromagnetic induction data, *Water Resources Research*, 50, 2732–2748. [27](#), [35](#)
- von Hebel, C., van der Kruk, J., Mester, A., Altdorff, D., Zimmermann, E., Endres, A., Vereecken, H. (submitted to *Geophysics*): Conversion and post-calibration for quantitative inversion of electromagnetic induction data beyond the LIN approximation, *Geophysics*. [15](#)
- Vrugt, J. A., Gupta, H. V., Bouten, W., Sorooshian, S. (2003): A Shuffled Complex Evolution Metropolis algorithm for optimization and uncertainty assessment of hydrologic model parameters, *Water Resources Research*, 39, 1201. [11](#)
- Vrugt, J. A., ter Braak, C. J. F., Diks, C. G. H., Robinson, B. A., Hyman, J. M., Higdon, D. (2009): Accelerating Markov Chain Monte Carlo Simulation by Differential Evolution with Self-Adaptive Randomized Subspace Sampling, *International Journal of Nonlinear Sciences and Numerical Simulation*, 10. [14](#)
- Wait, J. R. (1954): Mutual coupling of loops lying on the ground, *Geophysics*, 19, 290–296. [5](#)
- Wait, J. R. (1955): Mutual electromagnetic coupling of loops over a homogeneous ground, *Geophysics*, 20, 630–637. [8](#)
- Wait, J. R. (1962): A note on the electromagnetic response of a stratified Earth, *Geophysics*, 27, 382–385. [8](#)
- Wait, J. R. (1982): *Geo-Electromagnetism*, Academic Press Inc., New York, London. [8](#)
- Ward, S., Hohmann, G. (1988): *Electromagnetic Theory for Geophysical Applications*, in: *Electromagnetic Methods in Applied Geophysics*, edited by Nabighian, M. N., vol. 1 of *Investigations in Geophysics*, pp. 130–311, Society of Exploration Geophysics.

cists, United States of America. [4](#), [5](#), [8](#)

Weihermüller, L., Huisman, J. A., Lambot, S., Herbst, M., Vereecken, H. (2007): Mapping the spatial variation of soil water content at the field scale with different ground penetrating radar techniques, *Journal of Hydrology*, 340, 205–216. [36](#)



# List of Figures

1.1	Local and cumulative sensitivities of PRP, VCP and HCP coil configurations . . . . .	4
2.1	Multi-coil EMI data of multiple devices computed above layered earth models . . . . .	10
2.2	SCE inversion algorithm flowchart . . . . .	12
3.1	EMI phasor diagram and time representation . . . . .	18
3.2	Quadrature components of LIN-FM and exact EM-FM for different EMI coil configurations and subsurface properties . . . . .	19
3.3	LIN-based method and exact ECa conversion (EEC) . . . . .	20
3.4	Investigation of the EMI field setup influences on the measurements . . . . .	24
3.5	Site specific EMI-ECa calibration using ERT data . . . . .	26
3.6	Universal EMI-ECa calibration deduced using data of various test sites and dates . . . . .	28
3.7	Comparison of EMI and ERT sensitivities in the upper centimeter depth . . . . .	29
3.8	Experimental EMI data inversions using LIN-based conversion and EEC . . . . .	31
3.9	Universal calibrated experimental EMI data inversions . . . . .	32
4.1	Grain size distribution at Selhausen bare-soil field . . . . .	37
4.2	Depth sensitivities of multi-coil CMD-MiniExplorer . . . . .	38
4.3	Measured, predicted, and calibrated multi-coil EMI-ECa along calibration line . . . . .	40
4.4	Three-layer EMI inversion results along calibration line . . . . .	42
4.5	Linear regression plots for EMI-ECa calibration . . . . .	43

LIST OF FIGURES

---

4.6	Quantitative multi-coil ECa maps of bare-soil field . . . . .	46
4.7	Horizontal slices through quasi-3D inversion results . . . . .	47
4.8	Validation of vertical quasi-3D depth slices . . . . .	48
5.1	Topography and aerial image of the paleo-river channel field . . . . .	53
5.2	Custom made EMI sleds used during campaign I and campaign II . . . .	54
5.3	Depth sensitivities of multiple multi-coil EMI devices . . . . .	54
5.4	Quantitative ECa maps of the paleo-river channel field measured in July 2012 showing Auger positions for campaign I and locations of the detailed measurements performed in July/Aug. 2015 within campaign II . . . . .	59
5.5	Quasi-3D three-layer inversion results of campaign I . . . . .	60
5.6	Comparison between quasi-3D inversion results and ERT tomogram above paleo-river channel . . . . .	61
5.7	Campaign I and campaign II large-scale imaging of paleo-river channel attributes . . . . .	63
5.8	Transect T1 n-layer inversion results of multiple multi-coil EMI device data and boreholes drilled in campaign II . . . . .	65
5.9	Comparison of four/five-layer inversion results to the soil cores drilled at transect T1 . . . . .	66
5.10	Transect T2 n-layer inversion results of multiple multi-coil EMI device data and boreholes drilled in campaign II . . . . .	68
5.11	Comparison of four/five-layer inversion results to the soil cores drilled at transect T2 . . . . .	69
6.1	Selhausen focus area for upcoming EMI surveys. . . . .	76
A.1	VES data inversion results . . . . .	80
A.2	Mutltiple multi-coil EMI device calibration based on inverted VES data	81
A.3	Recorded and calibrated mutltiple multi-coil EMI device ECa . . . . .	83
B.1	Topography and aerial image of the bare-soil field . . . . .	86
B.2	Wheather conditions during/before bare soil field survey and paleo-river channel field campaigns . . . . .	87

---

B.3 Synthetic study to obtain optimum field setup for paleo-river channel reconstruction . . . . .	88
B.4 Regression analysis of $\sigma(z_i)$ and soil texture over Auger depth increments	90
B.5 Quasi-3D inversion results and predicted field capacity of the paleo-river channel field . . . . .	91
B.6 Quantitative ECa maps of paleo-river channel field at campaign II . . .	92
B.7 Four-layer inversion results compared to the soil cores drilled at T1 . . .	93
B.8 Five-layer inversion results compared to the soil cores drilled at T1 . . .	94
B.9 Four-layer inversion results compared to the soil cores drilled at T2 . . .	95
B.10 Five-layer inversion results compared to the soil cores drilled at T2 . . .	95
C.1 Determination of maximum layer thicknesses for a three-layer inversion using depth of investigation . . . . .	98
C.2 SCE and DREAM inversions of noise-free and noise-contaminated synthetic data and uncertainty analysis based on DREAM results . . . . .	99
C.3 Maximum layer boundaries set for four-layer inversions and EMI device measurement error estimates required by likelihood function used in DREAM algorithm . . . . .	100
C.4 Comparison of SCE and DREAM inversion results at borehole locations	101



# List of Tables

2.1	Multi-coil EMI device configurations . . . . .	9
3.1	LIN-based and exact ECa conversion (EEC) of homogeneous and layered subsurface models . . . . .	21
3.2	Inversion results of LIN-based and EEC converted models . . . . .	22
3.3	Test sites and their land use . . . . .	27
4.1	Mean absolute deviations between calibrated and uncalibrated EMI data	44
A.1	VES electrode distances of Schlumberger array . . . . .	78
A.2	Linear regression parameters of VES and ERT based post-calibration obtained at the paleo-river channel field for ME, SE, and DUEM . . . . .	82
C.1	Multi-coil EMI device configurations . . . . .	97



# List of movies

1. [Chapter 4](#): East-West directed vertical depth slices running from South to North through the bare-soil field.
2. [Chapter 5](#): Horizontal depth slices from top to bottom at the paleo-river channel field obtained by inverting the CMD-MiniExplorer (ME) data of campaign I.
3. [Chapter 5](#): Horizontal depth slices from top to bottom at the paleo-river channel field obtained by jointly inverting the ME & CMD-SpecialEdition (SE) data of campaign II.



# Danksagung

Die vorliegende Dissertation ist im Forschungszentrum Jülich, Institut für Bio- und Geowissenschaften, Agrosphäre, IBG-3, entstanden und wurde durch TR32 (Transregional Collaborative Research Centre 32), 'Pattern in Soil-Vegetation-Atmosphere Systems: Monitoring, Modelling and Data Assimilation', finanziert durch die DFG (Deutsche Forschungsgemeinschaft), unterstützt. Weiterhin waren TERENO (Terrestrial Environmental Observations), ACROSS (Advanced Remote Sensing - Ground-Truth Demo and Test Facilities) beteiligt und ich danke TerrSys (Centre for High-Performance Scientific Computing in Terrestrial Systems) sowie dem JSC (Jülich supercomputer center).

Zuerst bedanke ich mich bei meinem Doktorvater Prof. Dr. Jan van der Kruk für seine großartige Unterstützung, sein immer offenes Ohr und die immer anregenden Diskussionen in denen er aus seinem unermesslichen Ideenreichtum schöpft. Jan, recht herzlichen Dank und ich freue mich auf die weiteren Projekte. Ebenfalls danke ich den beiden Berichtern, Prof. Dr. Bülent Tezkan und Associate Prof. Dr. Tomáš Fischer für den Aufwand und die Zeit, die sie in die Beurteilung meiner Arbeit investiert haben sowie für die spannende Diskussion in der Verteidigung. Es war sehr gut. Vielen Dank.

Ich möchte diese Stelle auch nutzen, um mich bei Prof. Harry Vereecken zu bedanken, welcher sich als Institutsleiter sehr für das Bestreben und Vorankommen der Doktoranden einsetzt und auch Zeit für einen regen Austausch findet. Ein recht herzliches Dankeschön gilt auch den Kollegen im Institut, die zum Erfolg der vorliegende Dissertation beigetragen haben. Hier sind für anregende Diskussionen Prof. Sander Huisman, Dr. Achim Mester, Dr. Daniel Altdorff, Inge Wiekenkamp, Dr. Anja Klotzsch und Sebastian Rudolph zu nennen. Für die technische Unterstützung danke ich besonders Rainer Harms. Und für die Hilfe bei den Messungen danke ich Philipp Pohlig, Luka Kurnjek und Dr. Lutz Weihermüller.

Mein besonderer Dank gilt Eva, Liebe meines Lebens, Ehefrau und Mutter unserer tollen Kinder Leo und Lenny, für ihre Geduld, Unterstützung und vor allem Liebe. Ein ganz großes Danke an meine Eltern Monika und Kurt, die mir immer mit Rat und Tat zur Seite stehen und mich in meinen Vorhaben immer bestärken. Ein ausdrückliches Dankeschön auch an meine Schwiegereltern, Bärbel und Günter, für ihre stetige Bereitschaft uns zu helfen und natürlich auch an die tolle Familie meiner Schwester Mareike mit Chris und ihren Kindern Luisa, Jule und Emily. Ein Vielen Dank geht an Sieglinde, Maria und Willem, und an alle Familienmitglieder, ich bin froh Euch zu haben und bei Euch zu sein. Ich danke meinem besten Freund Daniel, sowie Philipp, Patrick, Frederic und allen Freunden und Wegbegleitern. Danke das ihr da seid.



# Christian von Hebel

## Curriculum Vitae

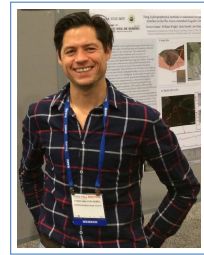
Senefelderstr. 48

D - 50825 Köln

+49 172 8762872

+49 2461 619404

✉ c.von.hebel@fz-juelich.de



### Personal Details

Date of birth March 9<sup>th</sup>, 1981  
Place of birth Köln, Germany  
Nationality German

### Education

- 10/2012–present **Doctoral studies,**  
*Institute of Bio- Geoscience, Agrosphere (IBG3), Forschungszentrum Jülich and Rheinisch-Westfälische Technische Hochschule (RWTH) Aachen, Germany.*
- Doctoral thesis Calibration and large-scale inversion of multi-configuration electromagnetic induction data for vadose zone characterization
- Supervisor Prof. Dr. Jan van der Kruk, IBG3, Forschungszentrum Jülich and RWTH Aachen
- 09/2010–08/2012 **Master in Applied Geophysics,**  
*Joint Master Program of three Universities, TU Delft (Netherlands), ETH Zurich (Switzerland), and RWTH Aachen (Germany).*
- Master thesis Multi-layer conductivity inversion of calibrated multi-configuration electromagnetic induction measurements
- Supervisor Prof. Dr. Jan van der Kruk, IBG3, Forschungszentrum Jülich and RWTH Aachen
- 10/2007–08/2010 **Bachelor in Geotechnology,**  
*Technical University (TU) Berlin, Germany.*
- Bachelor thesis Hydrogeologische und hydrochemische Untersuchungen im Einzugsgebiet des Schlottermühlbachs in Oberfranken
- Supervisor PD Dr. Traugott Scheytt, Applied Geoscience, TU Berlin
- 10/2006–10/2007 **Studies in Geophysics and Meteorology,**  
*University of Cologne, Germany.*
- 09/2002–07/2005 **Abitur,**  
*Abendgymnasium der Stadt Düsseldorf, Germany.*

---

## Work Experience

### Monash University, Melbourne AUS

- 11/2014 Soil Moisture Active Passive Experiments (SMAP-ex)  
Geophysical investigation of the shallow subsurface with the aim to contribute to soil moisture contents derived by remotely sensed microwave radiometry and GNSS-R observations

### SOGLO Project, Arvorezinha and Ilopolis, Brasil

- 08/2014 Electromagnetic induction survey to support the Soil system under Global change (SOGLO) project

### Fugro Consult GmbH

- 07/2011–08/2011 Internship in Geothermal energy  
Design, maintenance, and calculations of borehole heat exchanger and oil pollution disposal planning

### Self-employed

- 07/2004–08/2010 Beside studying; planning, organization, and realization of promotion jobs

### Bayer AG & Bayer Cropscience AG

- 02/2001–07/2004 Chemical laboratory worker  
Research and evaluations of novel formulated plant protectants
- 09/1997–02/2001 Apprenticeship to chemical laboratory worker

---

## Publications

### First Author

- 2014 **von Hebel, C.**, S. Rudolph, A. Mester, J.A. Huisman, P. Kumbhar, H. Vereecken, and J. van der Kruk. Three-dimensional imaging of subsurface structural patterns using quantitative large-scale multiconfiguration electromagnetic induction data. *Water Resources Research*, 50, 2732–2748, doi:10.1002/2013WR014864
- submitted **von Hebel, C.**, J. van der Kruk, A. Mester, D. Altdorff, E. Zimmermann, A. Endres, and H. Vereecken. Conversion and post-calibration for quantitative inversion of electromagnetic induction data beyond the LIN approximation. *Geophysics*
- in prep. **von Hebel, C.**, J. van der Kruk, H. Vereecken. Imaging of paleo-river channels by joint data inversion of multiple electromagnetic induction devices

### Co-Author Publications

- 2015 **Rudolph, S.**, J. van der Kruk, C. von Hebel, M. Ali, M. Herbst, C. Montzka, S. Patzold, D.A. Robinson, H. Vereecken, L. Weihermüller. Linking satellite derived LAI patterns with subsoil heterogeneity using large-scale ground-based electromagnetic induction measurements. *Geoderma*, 241, 262–271, 10.1016/j.geoderma.2014.11.015

### Co-Author Publications (continue)

- 2015 **van der Kruk, J.**, N. Gueting, A. Klotzsche, G. He, S. Rudolph, C. von Hebel, X. Yang, L. Weihermüller, A. Mester, H. Vereecken. Quantitative multi-layer electromagnetic induction inversion and full-waveform inversion of crosshole ground penetrating radar data. *Journal of Earth Science*, 26 (6), 844–850, 10.1007/s12583-015-0610-3
- 2015 **Borchard, N.**, M. Schirrmann, C. von Hebel, M. Schmidt, R. Baatz, L. Firbank, H. Vereecken, M. Herbst. Spatio-temporal drivers of soil and ecosystem carbon fluxes at field scale in an upland grassland in Germany. *Agriculture, Ecosystems and Environment*, 211, 84–93, 10.1016/j.agee.2015.05.008
- accepted **Aldorff, D.**, C. von Hebel, N. Borchard, J. van der Kruk, H. Bogena, H. Vereecken, J.A. Huisman. Potential of catchment-wide soil water content mapping using electromagnetic induction in a forest ecosystem. *Environmental Earth Science*
- in prep. **Mester, A.**, E. Zimmermann, C. von Hebel, J. van der Kruk, H. Vereecken and S. van Waasen, Field-optimization and validation of a novel multi channel electromagnetic induction system

---

### Conferences and Workshops

- 10/2015 TERENO Workshop, Remote sensing and soil  
Improved catchment characterization by nesting ground and satellite based sensors, Invited Poster
- 06/2015 SEG 6th International Geosciences Student Conference  
3D subsurface imaging using calibrated large-scale electromagnetic induction data, Invited Talk (Presenter Jan van der Kruk)
- 04/2015 European Geoscience Union (EGU), General Assembly 2015  
Large-scale multi-configuration electromagnetic induction: a promising tool to improve hydrological models, Invited Talk
- 12/2014 American Geophysical Union (AGU), Fall Meeting 2014  
Toward catchment vadose zone characterization by linking geophysical electromagnetic induction and remote sensing data, Poster presentation
- 09/2014 TERENO International Conference 2014  
Combined satellite and proximal soil sensing approach for improved catchment characterization, Oral presentation
- 03/2014 Deutsche Geophysikalische Gesellschaft (DGG), 74. Jahrestagung  
Large-scale 3D multi-layer electromagnetic induction data inversion, Oral presentation
- 04/2013 European Geoscience Union (EGU), General Assembly 2013  
From 1D-multi-layer-conductivity-inversion to pseudo-3D-imaging of quantified electromagnetic induction data acquired at a heterogeneous Test Site, Oral presentation

### Conferences and Workshops (continue)

- 03/2013 TR32-HOBE International Symposium  
Semi-3D Multi-layer Inversion of Calibrated Electromagnetic Induction Data acquired at the Selhausen test site, Oral presentation
- 03/2014 Deutsche Geophysikalische Gesellschaft (DGG), 74. Jahrestagung  
Towards large scale multi-layer-conductivity inversion of quantitative electromagnetic induction data , Oral presentation
- 02/2013 HydroGeophysics Workshop - Advancing Hydrogeophysics  
Multi-layer-conductivity inversion of quantitative electromagnetic induction data, Poster presentation

---

## Collaborations, Co-supervisions, and, Teaching

### Collaborations

- SOGLO Soil system under Global change
- Bonares Boden als nachhaltige Resource
- Earthshape Earth Surface Shaping by Biota

### Co-supervisions (CoS) and Support (Su)

- M.Sc. Combined GPR and EMI Characterization of Rollesbroich, CoS, J. Becker
- Ph.D Investigation of the impact of land use changes on soil processes using EMI, Su, J. Robinet
- Diploma Oberflächennahes Mehrspulenverfahren in der Anwendung auf geotechnische, geologische, und archäologische Fragestellungen, Su, G. Avci

### Teaching

- 2015 Masters course HydroGeophysics, RWTH Aachen
- 2014 Bachelor course Angewandte Geophysik II, RWTH Aachen

---

## Trainings and School

- 2012-recent Integrated Research Training Graduate School
- 12/2015 How to write and publish a scientific paper and scientific ethics, by Markus Flury
- 04/2014 English academic writing, workshop
- 02/2014 Statistics course, by Mort Canty
- 03/2013 Einführung in ParaView zur Visualisierung von wissenschaftlichen Daten
- 11/2012 Introduction to the programming and usage of the supercomputing resources at Jülich
- 11/2012 English academic presentation, workshop

---

## Computer Skills

Prog. languages C, Python (basic)  
Computer algebra Matlab (advanced)  
Geophysical tools Res2Dinv (advanced), Reflex ,ProMax, Petrell, ModFlow (all basic)

---

## Languages

German Mother tongue  
English Fluent (written and spoken)  
Dutch Basic

---

## Interests

Literature Thriller, Crime, and Drama  
Sports Cycling and hiking  
Traveling Exploring metropol's of the earth



Band / Volume 348

**Bipolarplattenmaterialien für Polymer-Elektrolyt-Membran Elektrolyse**

M. Langemann (2016), I-III, 189, IV-XVIII pp

ISBN: 978-3-95806-192-7

Band / Volume 349

**Modellbasierte Ansteuerung räumlich ausgedehnter Aktuator-  
und Sensornetzwerke in der Strömungsregelung**

M. Dück (2016), XIII, 153 pp

ISBN: 978-3-95806-193-4

Band / Volume 350

**TRENDS 2015 – Transition to Renewable Energy Devices and Systems**

ed. by D. Stolten and R. Peters (2016), 200 pp

ISBN: 978-3-95806-195-8

Band / Volume 351

**Dual Phase Oxygen Transport Membrane  
for Efficient Oxyfuel Combustion**

M. Ramasamy (2016), VIII, 136 pp

ISBN: 978-3-95806-196-5

Band / Volume 352

**Transport, co-transport, and retention of functionalized  
multi-walled carbon nanotubes in porous media**

M. Zhang (2016), VII, 112 pp

ISBN: 978-3-95806-198-9

Band / Volume 353

**Untersuchungen zur Luftqualität in Bad Homburg**

C. Ehlers, D. Klemp, C. Kofahl, H. Fröhlich, M. Möllmann-Coers  
und A. Wahner (2016), IV, 93 pp

ISBN: 978-3-95806-199-6

Band / Volume 354

**Herstellung thermisch gespritzter Schichten  
mit optimierten Spannungseigenschaften**

M. Mutter (2016), VI, 142, VII-XXII, xxvi pp

ISBN: 978-3-95806-200-9

Band / Volume 355

**Entwicklung selbstheilender Wärmedämmschichten**

D. Koch (2016), X, 120 pp

ISBN: 978-3-95806-201-6

Band / Volume 356

**Betriebsstrategien für Brenngaserzeugungssysteme zur Anwendung in HT-PEFC-Hilfsstromaggregaten**

D. Krekel (2017), IX, 265 pp

ISBN: 978-3-95806-203-0

Band / Volume 357

**Korrosion metallischer Bipolarplatten in Hochtemperatur-Polymerelektrolyt-Brennstoffzellen**

V. Weißbecker (2017), viii, 194 pp

ISBN: 978-3-95806-205-4

Band / Volume 358

**Realistic Bandwidth Estimation in the Theoretically Predicted Radionuclide Inventory of PWR-UO<sub>2</sub> Spent Fuel Derived from Reactor Design and Operating Data**

I. Fast (2017), XI, 129 pp

ISBN: 978-3-95806-206-1

Band / Volume 359

**Light Trapping by Light Treatment**

Direct Laser Interference Patterning for the Texturing of Front Contacts in Thin-Film Silicon Solar Cells

T. Dyck (2017), vi, 172, XI pp

ISBN: 978-3-95806-208-5

Band / Volume 360

**Interface and Topography Optimization for Thin-Film Silicon Solar Cells with Doped Microcrystalline Silicon Oxide Layers**

C. Zhang (2017), VII, 156 pp

ISBN: 978-3-95806-209-2

Band / Volume 361

**Calibration and large-scale inversion of multi-configuration electromagnetic induction data for vadose zone characterization**

C. von Hebel (2017), ix, 123 pp

ISBN: 978-3-95806-210-8

Weitere *Schriften des Verlags im Forschungszentrum Jülich* unter  
<http://www.zb1.fz-juelich.de/verlagextern1/index.asp>



**Energie & Umwelt /  
Energy & Environment  
Band / Volume 361  
ISBN 978-3-95806-210-8**

